Optogenetic investigation of local adrenaline signaling effects on cardiac arrhythmia mechanisms

Dissertation

zur

Erlangung des Doktorgrades (Dr. rer. nat.)

der

Mathematisch-Naturwissenschaftlichen Fakultät

der

Rheinischen Friedrich-Wilhelms-Universität Bonn

vorgelegt von

Vanessa Stefanie Martha Dusend

aus

Nürnberg, Deutschland

Bonn, 2023

Angefertigt mit Genehmigung der Mathematisch-Naturwissenschaftlichen Fakultät
der Rheinischen Friedrich-Wilhelms-Universität Bonn

1. Gutachter: Prof. Dr. Philipp Saße
2. Gutachterin: Prof. Dr. Evi Kostenis

Tag der Promotion: 02.11.2023
Erscheinungsjahr: 2024

Contents

Abbreviations

Abbreviation	Definition
AC	Adenylate cyclase
AKAP	PKA-anchoring protein
APD	Action potential duration
APD60	Action potential duration at 60% repolarization
Approx.	Approximately
AR	Adrenergic receptor
ATP	Adenosine-5'-triphosphate
AV node	Atrio-ventricular node
bpm	Beats per minute
CaMKII	Ca^{2+}/calmodulin kinase II
cAMP	3’,5’-cyclic adenosine monophosphate
Casq2	Calsequestrin 2
Cat. no.	Catalog number
$Ca_v1.2$, CACNA1C, I_{CaL}	Voltage-gated L-type calcium channels / current
Cch	Carbachol
cGMP	3’,5’-cyclic guanosine monophosphate
ChR1 /2	Channelrhodopsin 1 / 2
CICR	Calcium- induced calcium release
cMyBP-C	Cardiac myosin-binding protein C
Contactin-2	Cntn2
CPVT	Catecholaminergic polymorphic ventricular tachycardia
cTn C	Cardiac troponin C
cTn I	Cardiac troponin I
Cx	Connexin
DAD	Delayed afterdepolarization
DMSO	Dimethyl sulfoxide
DTT	DL-Dithiothreit
EAD	Early afterdepolarization
ECG	Electrocardiogram
Eli50	Half-maximal effective light intensity
Epac	Exchange protein directly activated by cAMP

Abbreviation	Definition
FFT	Fast Fourier Transformation
FKBP12.6	FK506 binding protein
GDP	Guanosine-5'-diphosphate
GFP	Green fluorescent protein
GPCR	G-protein- coupled receptor
G-protein	guanine nucleotide-binding protein
GRK	G-coupled-coupled receptor kinase
GTP	Guanosine-5'-triphosphate
HCN4	Hyperpolarization-activated cyclic -nucleotide-gated cation channel 4
HEPES	4-(2-hydroxyethyl)-1-piperazineethanesulfonic acid
HRP	Horseradish peroxidase
Hsp20	Heat shock protein 20
IBMX	3-Isobutyl-1-methylxanthin
ICD	Implantable cardioverter-defibrillator
$I_{K,slow,}$ $K_v1.5$	slowly inactivating voltage-gated potassium channel / current
I_{K1}, $K_{ir}2.1$, KCNJ2	Inward rectifier potassium channel
K_{ATP}, I_{KATP}	ATP-sensitive potassium channel / current
$I_{Kr,}$ hERG, KCNH2	rapidly activating delayed rectifier potassium channel / current
$I_{Ks,}$ K_vLQT1, KCNQ1 and KCNE1	slowly activating delayed rectifier potassium channel / current
Iso	Isoprenaline
$I_{to,f}$, $I_{to,s}$	transient outward potassium channels / currents (fast and slow)
JellyOp	Jellyfish opsin
JellyOp pos.	JellyOp positive (JellyOp wt/tg)
jSR	Junctional sarcoplasmic reticulum
KH buffer	Krebs-Henseleit buffer
LED	Light emitting diode
LQT	Long QT
LTCC	L-type calcium channel
LV	Left ventricle
MW	Molecular weight
$Na_v1.5$, SCN5A, I_{Na}	voltage-gated sodium channel / current
NCX	Na+ / Ca2+ exchanger / Sodium calcium exchanger
Neg.	Negative
Norm.	Normalized

Abbreviation	Definition
PBS	Phosphate buffered saline
PCR	Polymerase chain reaction
PDE	Phosphodiesterase
PGH-1	Pittsburgh-1
PKA	Phosphokinase A
PLN	Phospholamban
Pos.	Positive
PP1	Phosphatase 1
PP2A	Phosphatase 2a
PVC	Premature ventricular contraction
RA	Right atrium
Rel.	Relative
RT	Room temperature
RV	Right ventricle
RyR2	Ryanodine receptor type 2
SA node	Sino-atrial node
SDS	Sodium dodecyl sulfate
Serca2a	Sarco/endoplasmic reticulum Ca^{2+}-ATPase 2a
SNS	Sympathetic nervous system
SOICR	Store overload-induced calcium release
SR	Sarcoplasmic reticulum
TAE	Tris-acetat-EDTA
TBST	Tris-buffered saline with tween20
Tris	Tris-(hydroxymethyl)-aminomethan
T-tubule	Transverse tubule
VF	Ventricular fibrillation
VT	Ventricular tachycardia

1 Introduction

1.1 Physiological and pathophysiological excitation in the heart

1.1.1 Physiological heart function

The heart's function is to enable a steady supply of oxygen and nutrients to all organs and tissues by generating blood flow with sufficient pressure, which can be rapidly adapted to changing needs. This adaptation is accomplished by the heart's intrinsic morphological and functional characteristics, as well as higher regulation via the autonomous nervous system.

The mammalian heart is comprised of two atria and two ventricles. The right atrium receives blood enriched in CO_2 and depleted of oxygen from the venous part of the systemic circulation and provides it to the right ventricle. The right ventricle pumps the blood through the pulmonary artery into the lungs, where the gas exchange happens to remove CO_2 and oxygenate the blood. Oxygenated blood then flows into the left atrium and from there into the left ventricle, which pumps the blood through the aorta into the arterial part of the systemic circulation, thus supplying the body with oxygen.

A heartbeat consists of two phases: diastole and systole. The myocardium is relaxed in diastole and the pressures in the ventricles are low. When the pressure in the ventricles falls below that of the atria, the atrio-ventricular valves open and the ventricles fill with blood passively due to a shift of the cardiac valvular plane and the pressure difference to the atria. Atrial contraction completes the filling of the ventricles. Atrial contraction is followed by the ventricular contraction, which marks the systole. Pressure rises in the ventricles until it exceeds the pressure in the aorta (in the left ventricle) or the pressure in the pulmonary artery (in the right ventricle). At this point blood is ejected from the ventricles. Typically, in humans at rest, systole lasts approx. 300 ms, while diastole lasts 600-700 ms. Both are dependent on the heart rate, and can shorten at higher frequencies, with the diastolic interval shortening more drastically than the systolic interval.[1]

1.1.2 Electrical activation of the heart

In order to ensure a coordinated heartbeat, the heart has to follow a specific pattern of electrical activation (Fig. 1A). The sino-atrial node (SA node), located in the dorsal right atrium, is the heart's pacemaker. Its cells spontaneously depolarize during diastole due to the opening of the non-selective hyperpolarization-activated cyclic nucleotide-gated cation channel 4 (HCN4) until the threshold membrane potential for the opening of voltage-gated calcium channels ($Ca_v1.2$, CACNA1C, I_{CaL}) is

reached, which induces an action potential[2]. Because cardiac cells are electrically coupled via gap junctions, the electrical activation of the SA node spreads through the atrial tissue, represented on an electrocardiogram (ECG, Fig. 1B) by the P-wave. The excitation then reaches the atrio-ventricular node (AV node), located at the junction of the right atrium and the ventricular septum. In the structurally normal heart the AV node is the only electrical passage from the atria to the ventricles, as a fibrous cardiac skeleton otherwise insulates them by spanning around the atrio-ventricular valves as well as the pulmonary and aortic valve. The AV node's slow conduction (~0.05 m/s) delays the electrical signal transmission until the filling of the ventricles is complete. This delay is visualized in the ECG as the PQ interval[1].

The excitation is conducted from the AV node into the ventricles via the ventricular conduction system. The conduction system consists of the bundle of His and the bundle branches, which are surrounded by a fibrous layer and located in the ventricular septum. From there, the excitation is transmitted to the Purkinje fibers, which span along the subendocardium at the lumen of the ventricles. The conduction system cells are characterized by a high density of voltage-gated sodium channels ($Na_v1.5$, SCN5A, I_{Na}) and gap junction proteins, which leads to a fast conduction velocity (2-4 m/s)[3]. The excitation further spreads through the myocardium of the ventricular wall and to the epicardial surface with a lower conduction velocity (~0.5 m/s). The propagation of the electrical excitation through the ventricular wall is represented on the ECG as the QRS complex[4].

An important characteristic of ventricular cardiomyocytes is their long-lasting refractory period. This refractory period is essential to ensure that each sinus beat only triggers one distinct beat of the heart and the heart then goes back to its resting state during diastole, which is necessary for complete blood ejection and refilling of the heart. The repolarization of the action potential through the ventricular wall, seen in the ECG as the T-wave, happens from the endocardium to the epicardium due to a prolonged action potential duration (APD) in the endocardial cardiomyocytes. The QT duration presents an essential marker for the cardiac refractory period, which is determined by the APD of the ventricular cardiomyocytes. In long QT (LQT) syndrome a prolongation of the APD in ventricular cardiomyocytes and, thus, prolonged QT interval leads to an increased arrhythmogenic potential. The underlying mechanisms of which are further discussed in Chapter 1.1.5.

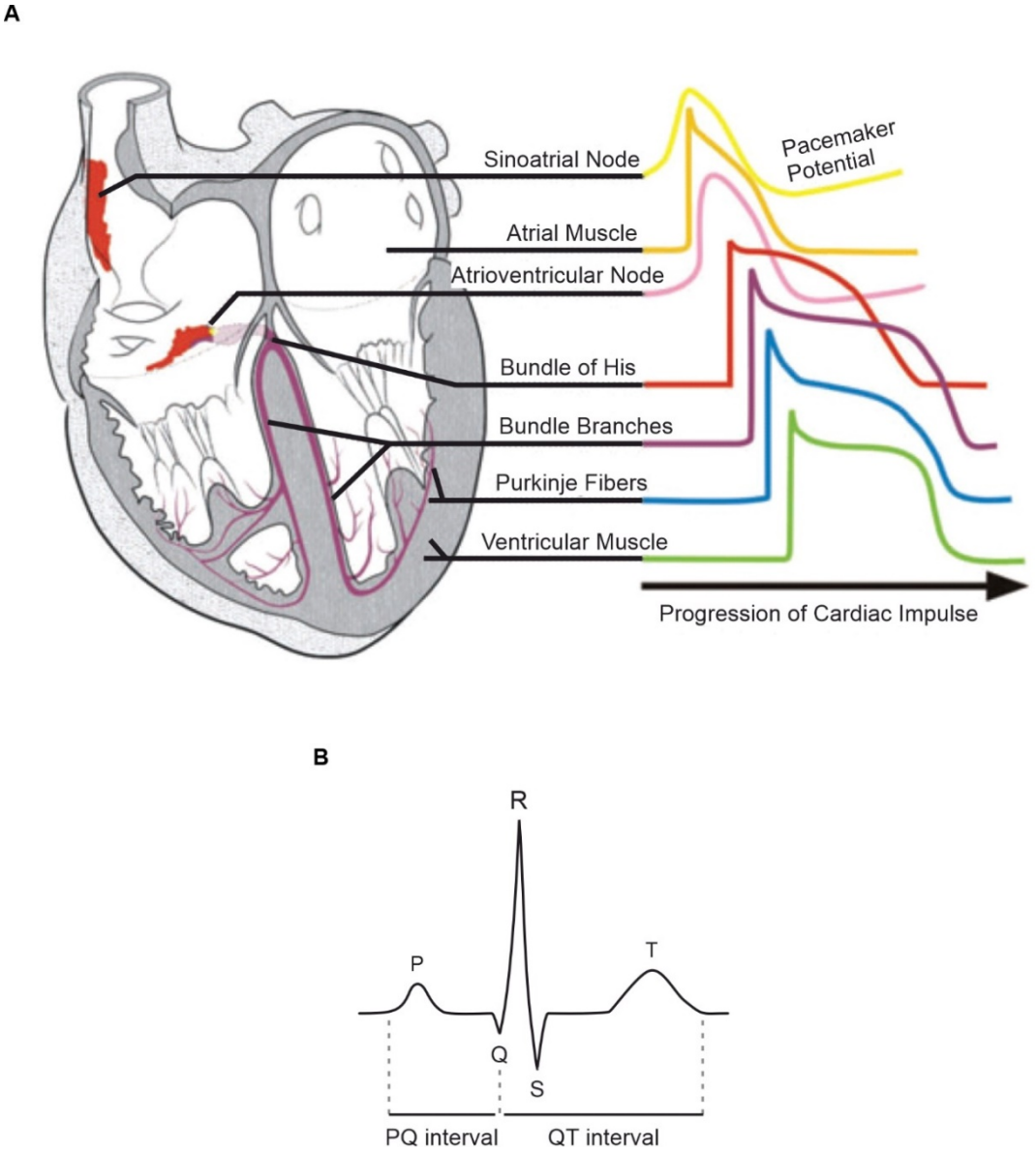

Figure 1: Electrical activation of the heart (adapted from Monfredi et al., 2010[5]).
A) Schematic of the heart (left) with typical action potentials in the different anatomic regions (right); B) Schematic of a human surface ECG with connotations of the main phases of the electrical conduction: P-wave: atrial activation, QRS complex: ventricular activation, T-wave: ventricular repolarization.

1.1.3 The action potential of ventricular cardiomyocytes

A ventricular cardiomyocyte has a resting membrane potential of -85 mV[6] maintained by the potassium current I_{K1} through the inward rectifier potassium channel (K_{ir}2.1, KCNJ2)[7]. In a regular beat, the cardiomyocyte is excited from a neighboring cell – either by another ventricular cardiomyocyte or by a Purkinje cell – via gap junctions. Gap junctions are pores located at the intercalated disks between two cardiomyocytes permeable for ions and molecules <1kDa. Gap junctions are comprised of connexins, of which six together form a hexagonal hemichannel – the connexon – in the cell

membrane. Two hemichannels of two adjacent cells then form a gap junction. The most abundant connexin isoform in ventricular myocytes is connexin 43 (Cx43), while the conduction system has higher expression levels of connexin 40 (Cx40) and connexin 45 (Cx45)[8]. The higher conductance and transcellular voltage sensitivity of Cx40 compared to Cx43 contributes, in addition to the higher expression of $Na_v1.5$ and gap junction proteins, to the faster conduction in the specialized conduction system compared to the working myocardium[8].

The initial small depolarization through gap junctions leads to the opening of $Na_v1.5$ channels [9,10], resulting in an action potential with a very fast upstroke of approx. 150 mV/ms to approx. +20 mV (phase 0, Fig. 2)[11]. This fast upstroke of the action potential is made possible by the block of $K_{ir}2.1$ by the biogenic amine spermine at membrane potentials above -50 mV[12]. Additionally, at -40 mV $Ca_v1.2$ channels – also referred to as L-type calcium channels (LTCC) – open, which further depolarize the cell and due to their long-lasting current are also responsible for the plateau phase of the action potential (phase 2)[13]. Sodium channels, on the other hand, are rapidly inactivated and stay in an inactivated state for the plateau and early repolarization phase, during which they cannot reopen and therefore create an absolute refractory period, where the cell cannot generate another action potential[14]. The absolute refractory period can be measured experimentally as the effective refractory period, which is reported to be 220-260 ms in humans, while only 30-80 ms in mice[15].

In addition, voltage-gated potassium channels open during an action potential, leading to the efflux of potassium and, thus, repolarization of the cell. Early repolarization from the action potential peak (phase 1) is caused by rapid opening of transient outward potassium channels ($I_{to,f}$, $I_{to,s}$)[16]. Opening of delayed outwardly rectifying potassium channels combined with the closing of $Ca_v1.2$ leads to the cell's repolarization (phase 3) and its eventual return to the resting membrane potential (phase 4). In humans, the main delayed outwardly rectifying potassium channels responsible for repolarization are I_{Kr} (hERG, KCNH2) and I_{Ks} (K_vLQT1, KCNQ1 and KCNE1)[17,18]. The primary repolarizing currents in mice are created by $K_v1.5$ ($I_{K,slow}$)[19,20] and I_{to}[21]. During the repolarization phase, the $Na_v1.5$ channels return from an inactivated to a closed state, which marks the time point of the transition from the absolute to the relative refractory period. During the relative refractory period a strong stimulus can potentially trigger another action potential, which, however, will be smaller in amplitude, have a slower upstroke velocity and a shorter APD[22,23].

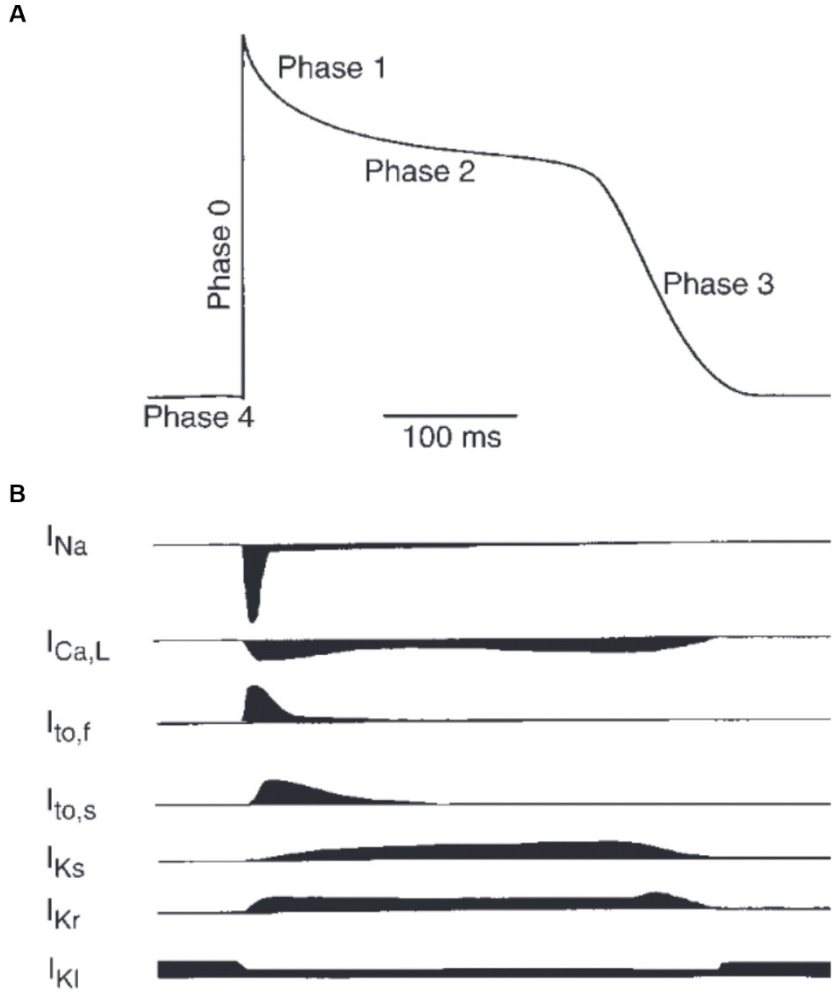

Figure 2: Ionic currents during the action potential of a human ventricular cardiomyocyte (adapted from Nerbonne and Kass, 2005[24]).
A) Schematic of the phases of a typical human ventricular action potential. B) Main ionic currents (down: inward, up: outward) with corresponding ion channels for sodium, calcium and potassium fluxes.

1.1.4 Excitation contraction coupling and calcium-induced calcium release

The basis for the contraction of a cardiomyocyte is a substantial increase in the cytoplasmic calcium concentration. As described in the previous chapter, an action potential is accompanied by the opening of $Ca_v1.2$ / LTCC (Fig. 3-1). Although the influx of calcium into the cell from the LTCC is only a smaller fraction of the total cytoplasmic calcium increase, this triggers the opening of ryanodine receptors type 2 (RyR2), which are calcium channels located in the sarcoplasmic reticulum (SR) membrane (Fig. 3-2,3). By this calcium-induced calcium release (CICR)[25] via RyR2 from the SR into the cytoplasm, the cytoplasmic calcium concentration increases from approx. 100 nM to 1-2 µM. Calcium in the cytoplasm binds to cardiac troponin c (cTn C), which is bound to tropomyosin along the thin actin filaments (Fig. 3-4), leading to a conformational change, thereby making actin binding domains accessible to myosin

heads on the thick myosin filaments. The cross-bridge cycle of actin-myosin binding then leads to the contraction of the cell.

CICR is optimized by the localization of the LTCC and the RyR2 within couplons in close proximity (~15 nm) of each other[26–28]. For this, the plasma membrane of a ventricular cardiomyocyte creates tubular invaginations called transverse tubules (t-tubules). T-tubules span along the short axis of the cell at the z-disc of each sarcomere and build functional units, called dyads, with the junctional SR (jSR), rich in RyR2.

At the end of the contraction, calcium is transported back into the SR by the sarco/endoplasmic reticulum Ca^{2+}-ATPase 2a (Serca2a; Fig. 3-5a) and out of the cell by the sodium calcium exchanger (NCX) in exchange for three sodium ions (Fig. 3-5b). In humans approx. 70 % of calcium ions are transported into the SR, while in mice up to 90 % are transported into the SR[25]. Calcium within the SR lumen binds to calsequestrin 2 (Casq2), which acts as a calcium buffer[29].

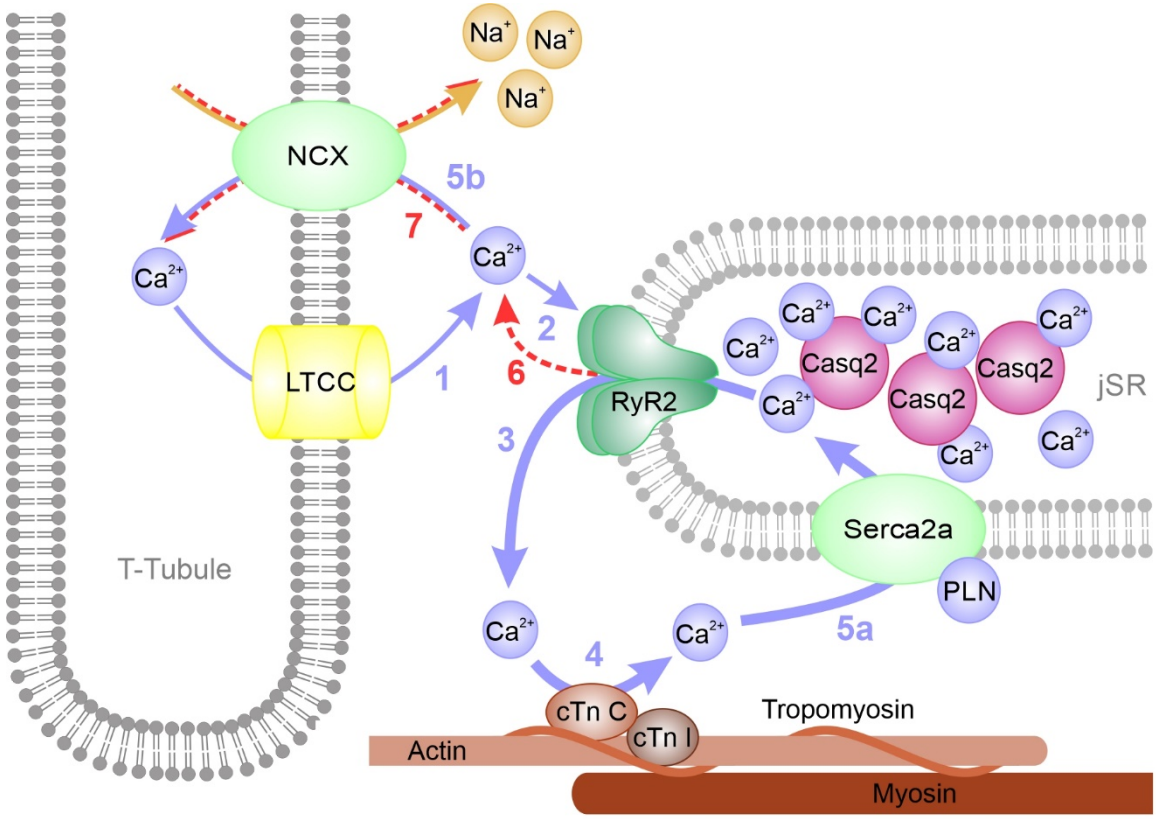

Figure 3: Calcium-induced calcium release.
Schematic of a calcium release unit of a ventricular cardiomyocyte. When LTCC opens, calcium enters the cell (1) and binds to RyR2 at the jSR (2). This leads to opening of the RyR2 and calcium efflux from the SR (3). Calcium binds to cTn C, which induces contraction (4). Calcium is transported back into the SR by Serca2a (5a) or out of the cell by NCX (5b). During diastolic calcium leak, calcium is released into the cytosol by RyR2 (6) and is subsequently exchanged for 3 sodium by NCX (7), causing a diastolic depolarization of the cell.

1.1.5 Mechanisms of ventricular arrhythmias

Arrhythmias are deviations of the heart from its regular beating rhythm. Arrhythmias can result from abnormal automaticity of cells inside or outside of the SA node or can be caused by aberrant conduction in the cardiac tissue.

One common way to categorize arrhythmias is by their place of origin. SA nodal dysfunctions can result in decreased (<60 beats per minute (bpm); bradycardia) or increased (>100 bpm; tachycardia) heart rate with otherwise normal conduction. When the SA nodal frequency is too low, the AV node can overtake the ventricular excitation as a secondary pacemaker with a lower intrinsic, spontaneous frequency (40-50 bpm). In extreme cases the conduction system or ventricular cardiomyocytes can also spontaneously depolarize, but with an even slower frequency (20-40 bpm)[1].

When an abnormal, fast pacemaker or conduction is situated in the atria, it is defined as an atrial arrhythmia. Atrial flutter is an abnormally fast contraction of the atria caused by reentry mechanisms, while atrial fibrillation is an irregular, fast reentry excitation of the atria hindering a coordinated contraction. Junctional arrhythmias originate in the AV node or the conduction system. They are characterized by an increased frequency of the QRS complex without a preceding P-wave, but with otherwise normal QRS morphology and duration[30].

In the case of ventricular arrhythmias, the arrhythmia's origin lies in the ventricles. Ventricular tachycardia (VT) is the autonomous beating of the ventricles at an increased frequency compared to the regular sinus rhythm and typically shows a deformed QRS complex with increased duration. VTs can either be triggered, whereby automaticity of an ectopic pacemaker in the ventricle triggers fast pacing of the ventricular myocardium, or reentrant, whereby an excitation wave is continuously propagated through the ventricular tissue[31].

Triggered VTs are periods of fast-paced spontaneous extrabeats generated by cells with an increased spontaneous rhythm, which can be caused by different forms of ionic imbalances leading to cell depolarization. This depolarization in ventricular cardiomyocytes can be divided by the time of occurrence into early afterdepolarizations (EADs) and delayed afterdepolarizations (DADs). EADs occur during the repolarization phase of the action potential. They are usually the result of a prolonged APD, for example, due to decreased repolarizing potassium currents as seen in LQT syndrome 1 and 2, which are caused by loss-of-function mutations in KCNQ1 and KCNH2 respectively, or increased late calcium or sodium currents in LQT syndrome 3, caused by gain-of-function mutations in $Ca_v1.2$ and $Na_v1.5$[32,33]. DADs are spontaneous depolarizations during the diastolic interval due to calcium leak from the SR via RyR2[34] (Fig. 3-6). The diastolic increase in calcium in the cytosol activates NCX, which transports one calcium ion out of the cell in exchange for three sodium ions, generating a depolarizing current into the cell[35] (Fig. 3-7). The activation of a single cluster of RyR2 and a subsequent local, subcellular release of calcium is referred to as a calcium spark[36]. However, a more synchronous fast calcium release throughout the cell is needed for a DAD to depolarize the cell up to its threshold potential and thereby trigger an action potential[35,37]. Moreover, on a whole organ level, it is not sufficient for one cell to generate an action potential, because the surrounding cells, coupled by gap junctions, form an electrical sink, silencing the active cell. For a premature ventricular contraction (PVC) to be generated either by EAD or DAD, multiple cells have to be depolarized synchronously. A mathematical model by Xie et al. estimated 700,000-800,000 cells are required to synchronize in a healthy 3D tissue to generate a PVC[38].

The onset of a reentry VT is usually an ectopic activity in the ventricle causing a PVC. This PVC can be generated like in triggered VTs by EADs or DADs. The excitation wave then continuously propagates

and repeatedly re-excites the tissue. For a spiral wave to be created and sustained, the propagating tissue needs specific electrical characteristics. In an anatomical reentry arrhythmia, the excitation wave is sustained by propagation around an anatomical obstacle, such as fibrotic or necrotic tissue as it occurs in heart failure or after myocardial infarction. A simple representation of this would be a ring-like structure of excitable tissue (Fig. 4A). In this ring-structure, a reentry can occur when the wave front is separated by its refractory tail by a gap of excitable tissue. In other words, the wavelength, which is the spatial extension of tissue currently displaying an action potential, must be shorter than the ring's circumference. The wavelength can be defined as the product of the refractory period and the conduction velocity. The refractory period can be directly correlated to the APD, while the conduction velocity is dependent on several different factors, such as excitability of the tissue, action potential upstroke velocity and connectivity via gap junctions[39,40]. A shortening of the wavelength is proarrhythmic as it becomes more likely to be able to induce reentry. Therefore, slower conduction velocity and shorter APD are both generally considered proarrhythmic due to a shortening of the wavelength. Seemingly contrary to this, conditions that prolong APD, such as LQT syndrome, are also proarrhythmic. This is explained by an increased likelihood of EADs and PVCs during the prolonged refractory period. In the ECG, the QRS complex resulting from a PVC during repolarization occurs during the previous T-wave. Therefore, it is also referred to as an R-on-T phenomenon. During the refractory period the cell is still partially depolarized and not all sodium channels are available in a closed state. The reduced sodium current reduces the upstroke velocity and thus slows conduction of the R-on-T PVC. A reduced calcium current by voltage and calcium dependent inactivation of $Ca_v1.2$[41] leads to a shorter APD. Therefore, the wavelength of an R-on-T PVC will be shortened. Moreover, tissue during this time window often displays increased heterogeneity as different parts of the ventricles are in different stages of refractoriness. Thus, PVCs in this time window lead to a higher dispersion of APD and conduction velocity. The combination of the shortening of the wavelength and the increased heterogeneity of the tissue make R-on-T PVCs especially likely to induce functional reentry VTs.

As opposed to anatomical reentry, a functional reentry VT occurs without an anatomical obstacle. Different models have been suggested to explain the sustained propagation in a functional reentry. One early model was the leading circle hypothesis, in which a circular excitation wave rotates around a tissue core that is continuously refractory by a centripetal excitation wave front from the circular excitation around it (Fig. 4B)[42].

Today the most common explanation for functional reentry, however, is the generation of rotors[43,44]. In a rotor the excitation wave is curved, so that the APD decreases towards the center and the wave front and wave tail meet in the center of the rotor, thus creating a singularity around which the wave rotates (Fig. 4C, D). In 2D, this rotor is typically referred to as a spiral wave. In 3D tissue like the

ventricular walls, the core around which the wave rotates builds a so-called filament and the spiral wave is referred to as a scroll wave (Fig. 4E)[45].

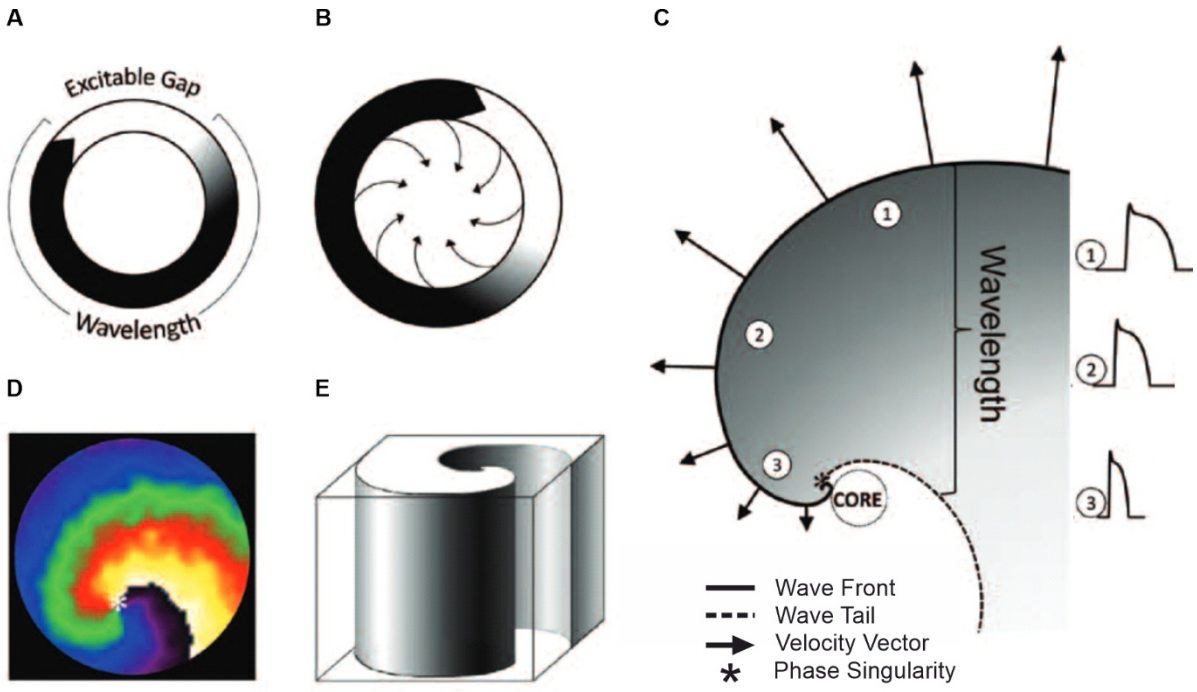

Figure 4: Mechanisms of reentry VT (adapted from Pandit and Jalife, 2013[43]).
A) Schematic of a continuous excitation wave in a ring structure. Black indicates excited cells, white resting cells, which form an excitable gap between the wave front (black arrow) and the wave tail. B) Schematic of the excitation in the leading circle hypothesis for reentry VT with centripetal excitation (arrows) building a refractory core. C) Schematic of a spiral wave with exemplary depictions of the conduction velocity (arrows) and action potentials at different positions in the spiral wave (1-3); * indicates the rotor core. D) 2D representation of a spiral wave; * indicates the rotor core. E) 3D representation of a scroll wave.

The morphology of the propagation throughout the ventricle determines the complexity of a VT. Triggered arrhythmias are typically monomorphic if generated by one focal activity (Fig. 5A) or bidirectional if two alternating focal points cause alternating activity[46]. Reentry VTs can have highly variable complexity. The simplest form of reentry VT is a monomorphic arrhythmia, in which the excitation circles around one stable, anchored rotor or filament (Fig. 5B). Polymorphic reentry VT occurs if the rotor is unstable, meandering in the ventricular tissue, or if multiple rotors exist simultaneously (Fig. 5C). Ventricular fibrillation (VF) is the most complex form of arrhythmia and also the cause of most sudden cardiac deaths. In VF, there are no clearly identifiable rotors as the excitation propagation appears as small, seemingly random wavelets throughout the ventricles (Fig. 5D). It is still

under discussion in how far the wavelet formation in VF results from random propagation and wave break, or if there could be an underlying stable high-frequency mother rotor that drives the VF[47,48].

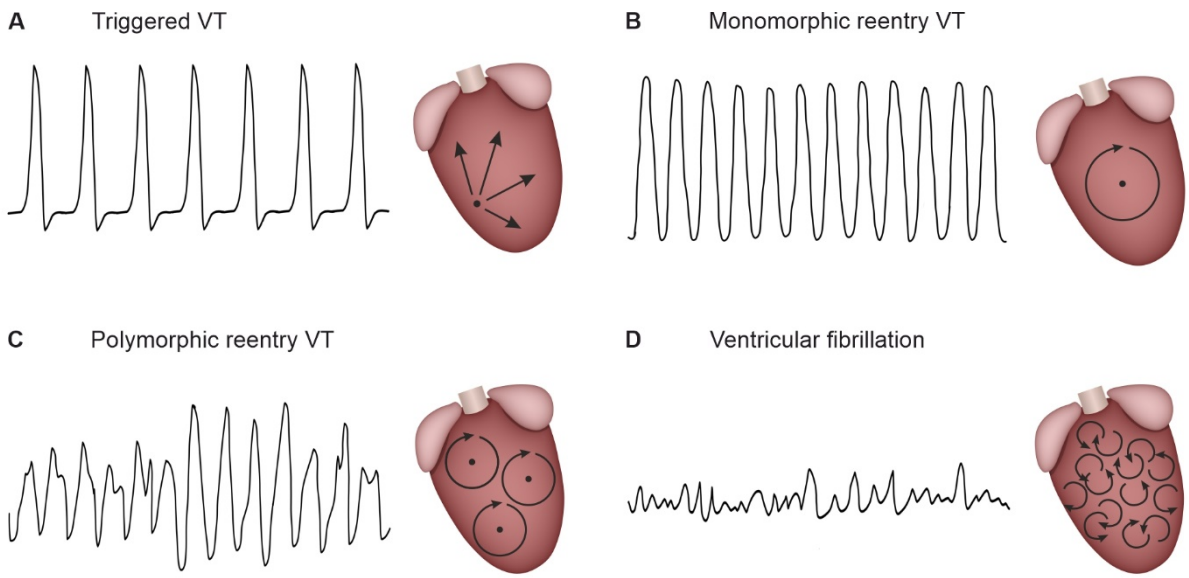

Figure 5: Morphology of ventricular arrhythmias.
Schematic examples of ECG traces with corresponding depiction of excitation propagation in the ventricles during triggered VT (A), monomorphic reentry VT (B), polymorphic reentry VT (C) and VF (D). Arrows depict simplified excitation propagation. Black dots represent the point of origin for triggered VT (A) or rotor cores for reentry VT (B, C).

1.1.6 Antiarrhythmic therapies

Several antiarrhythmic drugs are available for the treatment and prevention of cardiac arrhythmias. Antiarrhythmic drugs in standard use can be classified by their mode of action according to the Vaughan-Williams classification[49,50]. Class I antiarrhythmic drugs are sodium channel blockers, which are again subdivided into Class Ia – 1c, with different modes of action, effects on QT interval duration and indicated application in different arrhythmias. Examples include quinidine (Ia), lidocaine (Ib) and flecainide (Ic). They are primarily used in specific ventricular arrhythmia syndromes, such as Brugada syndrome, and atrial fibrillation, but are contraindicated in post-myocardial infarction arrhythmia prevention[51]. Class II antiarrhythmic drugs are β-adrenergic receptor (AR) blockers. β-blockers play an essential role in sudden cardiac death prevention in heart failure[52,53] and myocardial infarction[54,55] patients as well as hereditary catecholamine induced VTs by modulating multiple targets involved in cardiac excitation as discussed in more detail in the following chapters. Class III antiarrhythmic drugs are potassium channel blockers, e.g. amiodarone, which increase APD and the wavelength and, thus, reduce the risk of reentry VTs by decreasing the excitable gap. Calcium channel blockers, such as

verapamil, are class IV antiarrhythmic drugs mainly used for the treatment of supraventricular arrhythmias. Inhibition of I_{CaL} mainly affects the depolarization rate in SA nodal and AV nodal cells and, thus, reduces the heart rate and the AV node's conduction velocity. In ventricular myocytes it moreover prolongs the effective refractory period.

Antiarrhythmic drug therapy is often insufficient and catheter ablation or an implantable cardioverter-defibrillator (ICD) are necessary to prevent or quickly terminate ventricular arrhythmias. In addition, ICDs have been shown in multiple studies to reduce risk of sudden cardiac death more effectively than antiarrhythmic drugs[56,57].

There are also a number of other antiarrhythmic mechanisms, which have been targeted by antiarrhythmic drugs experimentally, but are not in clinical use, yet. Among these are for example gap junction modulators as well as ryanodine receptor blockers[58]. However, treating and preventing cardiac arrhythmias remains a major challenge in current clinical practice. While a broad range of antiarrhythmic therapies are available, their effectiveness varies widely in the different underlying arrhythmic conditions. Depending on the underlying arrhythmic mechanism these therapies can even enhance proarrhythmic effects. Therefore, research into the underlying mechanisms of arrhythmia generation to develop novel drugs with high antiarrhythmic effectiveness and reduced adverse effects is still necessary.

1.2 Physiological role of the sympathetic nervous system in the heart

1.2.1 The autonomous nervous system in the heart

The autonomous nervous system regulates homeostasis and rapid adaptation to changing demands within the body. It consists of two players: the parasympathetic and the sympathetic nervous system. The parasympathetic nervous system is activated during rest and is primarily responsible for homeostasis. It affects the heart by decreasing heart rate and slowing conduction of the AV node via M2 muscarinic acetylcholine receptors and subsequent G_i signaling[59].

Its antagonist is the sympathetic nervous system (SNS), which is activated during exercise or stress and is commonly associated with the 'fight-or-flight' response[60]. In the heart, activation of the SNS accelerates heart rate (positive chronotropy) and the conduction of the AV node (positive dromotropy). Furthermore, it increases contractile force (positive inotropy) and accelerates relaxation (positive lusitropy).

Post-ganglionic sympathetic neurons penetrate the myocardium from the subepicardium and have been found to typically run alongside the heart's vasculature, spreading through the myocardium into the endocardium[61]. Higher sympathetic innervation has been reported in the epicardium than the endocardium[62,63]. Sympathetic neurons display varicosities organized in a pearl-necklace structure containing vesicles that release the neurotransmitter noradrenaline[64]. While it has been commonly described that the neurotransmitter released from sympathetic neurons diffusely spreads between nerve processes and receptor-expressing cardiomyocytes, new research suggests a prominent role of direct, synapse-like interaction occurring between nerves and cardiomyocytes[65,66].

Noradrenaline binds to and activates ARs in the effector organ cells. Most of it is then re-taken up into the nerve by the transporter uptake 1, while it is estimated that 10-20% of the released noradrenaline spills over into the bloodstream[67]. Besides spill-over from the heart, a substantial amount of plasma-noradrenaline also comes from other organs, most notably the kidneys and skeletal muscle[67]. Moreover, adrenaline, as well as to a much lesser extent noradrenaline, is secreted from the adrenal glands into the blood stream, through which it is distributed to its effector organs, including the heart and the vasculature throughout the body.

Multiple ARs are differentially expressed throughout the body: α1A, α1B, α1D, α2A, α2B, β1, β2 and β3[68]. All ARs are 7-transmembrane G-protein-coupled receptors (GPCRs), belonging to the class A, rhodopsin-like GPCRs[69]. While α1-ARs, for example found in vascular smooth muscle cells, are $G_{q/11}$-coupled, α2-ARs are $G_{i/o}$-coupled. However, the most prominent subtypes in the heart are the G_s-coupled β1- and β2-ARs.

1.2.2 G_s-signaling in ventricular cardiomyocytes

The G_s-protein is a heterotrimeric guanine nucleotide-binding protein (G-protein), consisting of an α-subunit ($G_s\alpha$) and a βγ-subunit (Gβγ) (Fig. 6). In its inactive form, $G_s\alpha$ has bound guanosine-5'-diphosphate (GDP). When the G-protein-coupled receptor gets activated, it promotes GDP exchange for guanosine-5'-triphosphate (GTP), which leads to the dissociation of $G_s\alpha$ from Gβγ. As a result, free $G_s\alpha$ activates adenylate cyclases (ACs), of which AC5 and AC6 are predominant in cardiomyocytes[70]. Activated AC catalyzes the conversion of adenosine-5'-triphosphate (ATP) to 3',5'-cyclic adenosine monophosphate (cAMP). The second messenger cAMP, in turn, binds to the regulatory subunits of phosphokinase A (PKA), which releases its two catalytic subunits. PKA phosphorylates several effector proteins in the ventricular myocardium. Phosphorylation of LTCC enhances I_{Ca} by increasing open probability[71]. RyR2 phosphorylation at S2809 increases its open probability and its sensitivity towards calcium[72,73]. Unphosphorylated phospholamban (PLN) binds to and inhibits SERCA2a. Upon phosphorylation by PKA, PLN detaches from SERCA2a, which enhances and accelerates calcium re-transport to the SR[74,75]. Moreover, PKA also influences contraction and relaxation by phosphorylation of cardiac troponin I (cTn I), cardiac myosin-binding protein C (cMyBP-C) and titin[76].

Another important downstream pathway of G_s-signaling is the activation of Ca^{2+}/calmodulin kinase II (CaMKII) via PKA-mediated calcium increase as well as independently of PKA-activation via guanine nucleotide exchange protein directly activated by cAMP (Epac)[77]. CaMKII also phosphorylates among other targets the LTCC, the RyR2 and PLN[77,78]. There is, of yet, debate whether an increased open probability of the RyR2 is mainly mediated by PKA phosphorylation at S2808 (S2807 in mice) or PKA-dependent CaMKII phosphorylation at S2814 (S2813 in mice)[78].

The negative regulation and turn-off of G_s-signaling involve the hydrolyzation of cAMP catalyzed by phosphodiesterases (PDEs) and the dephosphorylation of effector proteins by phosphatases.

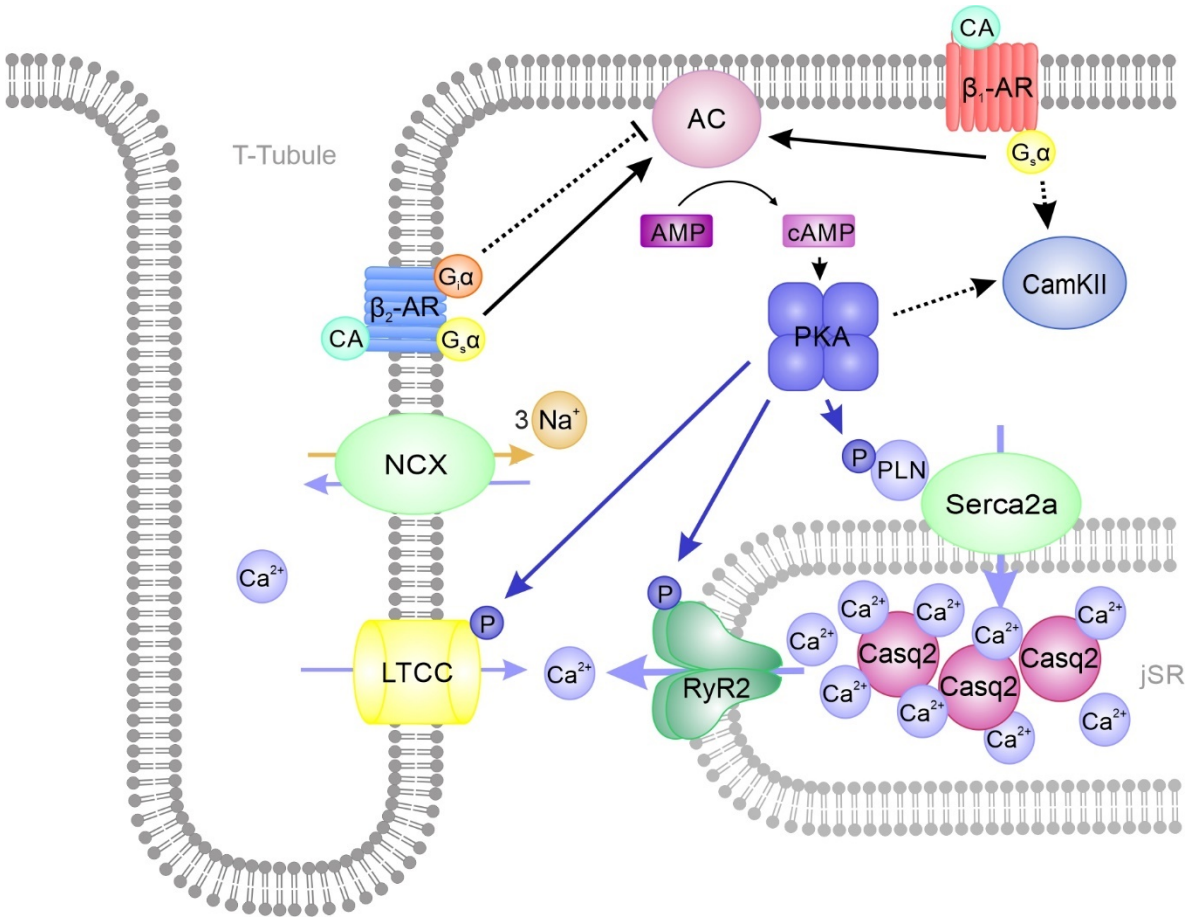

Figure 6: β-AR signaling in ventricular cardiomyocytes.
β-AR activation leads to AC activation via $G_s\alpha$ and subsequent cAMP production. cAMP activates PKA, which phosphorylates a number of proteins involved in CICR and cell contraction, such as LTCC, RyR2 and PLN. β2-AR, while predominantly activating the G_s-signaling pathway, can also switch to G_i-signaling, which inhibits AC activity.

1.2.3 β-ARs in ventricular cardiomyocytes

In ventricular cardiomyocytes, all three β-AR subtypes are expressed. However, the most abundant subtype is the β1-AR, distributed in the cytoplasmic membrane and the t-tubular system[79,80]. β1-AR exclusively couples to G_s-proteins and, in healthy hearts, was found to be the major mediator of the adrenergic response by increasing heart rate and contractile force.

β2-AR is found predominantly in the t-tubular membrane, where it is especially associated with Caveolin-3-rich caveolae and lipid rafts[80–83]. β2-AR is also mainly G_s-coupled, however, only a modest increase in heart rate and very little to no effect on contraction can be associated to β2-AR in the healthy heart[84]. The main role of the β2-AR seems to be activation of the LTCC, which has also been found to be enriched in caveolae[85,86].

This differential role of β1- and β2-AR might be explained by a number of different factors. One of these is the aforementioned differential localization of the two receptors in the plasma membrane. Another essential factor on the function of ARs is their modulation by phosphorylation. Both receptors can be phosphorylated by G-protein-coupled receptor kinases (GRKs). This mediates the binding of β-arrestin and the desensitization and internalization of the receptor[87]. The most notable difference in the phosphorylation of the receptors, however, is that β2-AR, but not β1-AR, upon phosphorylation by PKA, can switch from G_s-signaling to G_i-signaling[88], which inhibits AC.

Another factor is the interaction of the receptors with distinct scaffolding and downstream proteins, such as PKA, PKA-anchoring proteins (AKAPs) and PDEs. For example, β1-AR has been reported to bind to PDE4D8 in an inactivated state and release PDE4D8 upon activation[89]. This mechanism might reduce basal activity of the receptor, while promoting local cAMP increase upon agonist binding. Meanwhile, β2-AR was found to bind β-arrestin upon activation leading to desensitization of the receptor and β-arrestin dependent recruitment of PDE4D5 to the receptor, which limits local cAMP concentration[90].

1.2.4 Subcellular regulation of G_s-signaling

The intracellular response to the G_s-stimulating signal is highly controlled in space and time by many regulating mechanisms along the signaling cascade. As mentioned in the previous section, the first level of signal regulation is the localization and modulation of activation of β-ARs. Nevertheless, multiple other factors shape the response. In this regard, an important field of research is the compartmentation and subsequent creation of subcellular microdomains of cAMP, the central second-messenger in G_s-signaling.

PDEs are the main negative regulators of cAMP levels and are thereby thought to limit diffusion and create cAMP microdomains[91]. In cardiomyocytes there are six different PDE families expressed (PDE1, PDE2, PDE3, PDE4, PDE5 and PDE8), which additionally consist of multiple isoforms. PDE1, PDE2, PDE3, PDE4 and PDE8 are capable of hydrolyzing cAMP, while PDE5 is 3',5'-cyclic guanosine monophosphate (cGMP) specific. Each PDE displays specific expression patterns, activity regulators and localizations in the cardiomyocytes, which depend on the PDE's differential interplay with its binding partners[92,93].

PDE1 is activated by Ca^{2+}/calmodulin and is suggested to mostly regulate cGMP levels. The role of PDE1 in cardiomyocytes is still under discussion, but loss-of-function, as well as inhibitor studies, suggest a protective role against adrenergic induced hypertrophy[94]. PDE2 is stimulated by cGMP, thereby lowering cAMP levels through nitric oxide induced cGMP production[95,96]. It is situated at the plasma membrane and is thus an important regulator of LTCC phosphorylation[97]. PDE3 is a main down-regulator of the G_s-induced inotropic effect by modulating PLN phosphorylation and thus SERCA2a

activity and SR calcium uptake[98]. While PDE3 inhibitors are used to treat acute HF, long-term use is associated with increased mortality[99]. In relation to this, chronic downregulation of PDE3 was shown to increase cardiomyocyte apoptosis in a pressure-overload mouse model[100]. PDE4 has multiple isoforms expressed in cardiomyocytes with distinct localizations due to interaction with anchoring proteins such as AKAPs and myomegalin[101,102]. PDE4D for example associates together in a macromolecular complex with mAKAP and RyR2 in the space between the T-tubule and the jSR[103,104]. PDE4 regulates RyR2 phosphorylation, I_{Ks} phosphorylation[105] and is directly associated with β1-AR, which regulates local cAMP production at the receptor[89]. In heart failure and hypertrophic hearts, PDE4 is downregulated, which leads to RyR2 hyperphosphorylation associated with increased diastolic SR calcium leak and VT incidence[103]. PDE8 is a cAMP-specific PDE also expressed in cardiomyocytes. PDE8 knock-out led to higher increase of calcium-transients after β-adrenergic activation, as well as increased incidence of calcium sparks[106]. PDE8 has also been found to be insensitive to the unselective PDE inhibitor 3-Isobutyl-1-methylxanthin (IBMX)[92].

Another essential mechanism of regulation of G_s-responses is the control of phosphorylation levels of target proteins, which phosphatases can achieve. Phosphatase 1 (PP1) as well as phosphatase 2A (PP2A) are mainly involved in dephosphorylation kinetics in cardiomyocytes[107,108].

1.3 Pathological role of the sympathetic nervous system

1.3.1 The sympathetic nervous system in heart failure

Heart failure occurs when the heart is unable to pump blood effectively enough through the body, e.g. due to weakening or stiffening of the muscle. Heart failure is one of the most common diseases in the elderly, often coinciding with hypertension, diabetes and coronary artery disease. The prevalence in the overall European and US American population is estimated at 1-2%, with the prevalence increasing in persons older than 65 years of age[109]. The severity of heart failure can be determined according to structural remodeling in the heart, severity of symptoms and limitations of activity according to the American Heart Association stages A-D or the New York Heart Association Classes I-IV. It can be further divided into heart failure with reduced ejection fraction and heart failure with preserved ejection fraction[110].

As the SNS is an important regulator to increase cardiac output, early studies investigated whether activation of the β-adrenergic system might benefit heart failure patients' outcomes. However, it has been shown that long term pharmacological activation of β-AR signaling was detrimental for survival of heart failure patients[111,112]. On the contrary, inhibition of β-adrenergic signaling, either by β1-AR specific inhibitors or unspecific β-AR inhibitors, was beneficial for survival, making β-blockers the primary pharmacological therapies for heart failure[53,113].

In order to maintain or increase output in failing hearts, the SNS is activated and neuronal growth factor expression is increased, leading to hyperinnervation[114]. These changes can be indirectly measured by plasma-noradrenaline levels, which in heart failure patients can be increased at rest up to maximal exercise levels in healthy humans[115,116]. Even though this can initially and acutely conserve cardiac function and output, long-term hyperactivation of the SNS seems detrimental to disease outcome because higher plasma-noradrenaline levels directly correlate to worse heart failure prognosis[117]. On a cardiomyocyte level chronic β-adrenergic G_s-activation leads to hypertrophy and apoptosis[118–121].

A possible protective mechanism towards chronic activation of β-AR is a desensitization of the receptors due to the phosphorylation by GRKs and subsequent binding of β-arrestins to phosphorylated β-ARs, which desensitizes the receptors by impairing G-protein-coupling and promotes internalization[122,123]. Regarding this, overall β-AR expression is reduced by approx. 40% in human failing hearts, but β2-AR expression levels remain mostly unchanged[122]. This might be a protective mechanism, because β2-AR activation has the potential to promote survival of cardiomyocytes via coupling to G_i instead of G_s[121]. While these findings in mouse cardiomyocytes indicate a cardioprotective role of β2-ARs, this mechanism has not been clinically explored. Moreover,

there are also studies in mice indicating a detrimental effect of β2-AR in heart failure. Although expression levels of β2-AR do not change compared to healthy hearts, their localization does: instead of being mostly confined to the t-tubules, β2-AR in failing cardiomyocytes are also found on the plasma membrane[79]. A change in function accompanies this change in localization. While in healthy cardiomyocytes, β2-AR stimulation had only a minor effect on calcium transients or contractile force, in heart failure cardiomyocytes β2-AR stimulation induced an increase in calcium transients as well as increased calcium load in the SR and PLN phosphorylation[124,125]. Interestingly, these changes in β2-AR signaling were arrhythmogenic: β-AR stimulation induced arrhythmias in a rabbit heart failure model as well as in cardiomyocytes obtained from human heart failure patients and were blocked by the β2-AR blocker ICI 118,551[124].

In the further progression of heart failure, sympathetic denervation occurs, in which multiple mechanisms seem to be involved: anatomical denervation due to a decrease in nerve growth factor expression, trans-differentiation of adrenergic into cholinergic neurons as well as a functional denervation by expression of fetal genes driven by leukemia inhibitory factor[114].

Of particular research interest is the relationship of these changes in sympathetic activity on the generation of arrhythmias. 30-50% of heart failure deaths are due to sudden death from lethal ventricular arrhythmias[126,127], making arrhythmia prevention one of the most important factors for the survival of heart failure patients. Both regional hyperinnervation and regional denervation, which also occur after myocardial infarction, are proarrhythmic[128,129]. A possible reason for this is that both overall lead to increased heterogenous activation and promote dispersion of APD and conduction velocity throughout the tissue. This is supported by experiments on left ventricular wedge preparations from heart failure patients, where β2-stimulation specifically exacerbated a transmural dispersion of calcium transient duration and APD[125]. The same study also showed that β1- as well as β2-stimulation increased Purkinje fiber automaticity in failing hearts. Overall, the role of local, heterogenous activation of G_s-signaling in the generation of VTs remains a point of great interest in current research.

1.3.2 Catecholaminergic ventricular tachycardia

The SNS is not only implicated in the arrhythmia formation in structural remodeling, such as in heart failure or after myocardial infarction, but also in several hereditary diseases, in which activation of the SNS is directly responsible for generating ventricular arrhythmias.

One such hereditary disease, which will be part of the focus of this thesis, is catecholaminergic ventricular tachycardia (CPVT). CPVT is a rare but highly lethal hereditary disease with an incidence of approx. 1:10000 in the European population and a mortality rate of 30-50% by the age of 40 years if

untreated[130,131]. Manifestations of CPVT are syncope or (aborted) sudden cardiac death caused by ventricular arrhythmias upon emotional stress or exercise. The first symptoms usually occur in the first or second life decade. The heart of CPVT patients is structurally normal and the resting ECG is inconspicuous with a narrow QRS complex and a normal QT interval. The only manifestation that regularly occurs during rest is a slight sinus bradycardia[132,133]. Upon exercise-stress test or adrenaline infusion a high number of PVCs occur, which later typically devolve into bidirectional or polymorphic ventricular arrhythmia[132]. An investigation of electrocardiographic characteristics by Sumitomo et al. in 2003 reported 72% of VT episodes to be non-sustained, 21% to be sustained and 7% devolved from polymorphic or bidirectional VT into VF[134].

The first case of CPVT was reported in 1975[135], however, the first mutation linked to CPVT was only identified in 1999 in the RyR2[136,137]. Shortly after, a second locus for CPVT was found to belong to the Casq2 gene[138,139]. CPVT with RyR2 mutation or Casq2 mutation were termed CPVT1 and CPVT2, respectively. CPVT1 makes up about 50% of CPVT patients, while CPVT2 makes up only 2-3% of cases but shows higher mortality rates[130]. To date, there have been two other proteins identified as causes for CPVT: triadin[140] and calmodulin[141,142] (with three genes CALM1, CALM2 and CALM3 all encoding an identical protein), both of which make up less than 1% of cases[143]. Almost 50% of clinically classified CPVT patients could not yet be genetically linked to a gene. However, likely gene candidates are other proteins associated with the RyR2, such as junctin, which like triadin associates with RyR2 and Casq2 in the SR membrane, or the FK506 binding protein (FKBP12.6), which binds to the cytoplasmic side of RyR2 and inhibits it[144].

The general mechanism of VT induction in CPVT is an increased leakiness of the RyR2, which leads to a release of calcium from the SR during diastole and thus the generation of a DAD as described in Chapter 1.1.5.

CPVT1 has been linked to >50 different mutations in RyR2, that are mostly autosomal dominant. There are three major concepts by which RyR2 receptor mutations increase the open probability of the receptor (Fig. 7A-C). The first concept is that mutations impair the ability of FKBP12.6 to either bind to the RyR2 or to inhibit the receptor during diastole, thus increasing the open probability of RyR2 during diastole[145,146]. The second concept is that mutations alter the receptor's sensitivity to luminal SR calcium and decrease the threshold of luminal SR calcium needed to open RyR2[147]. The third concept is that mutations cause a conformational change in the pore of the receptor leading to a so-called 'unzipping' and, thus, opening of the receptor[148,149].

All of these effects are highly exacerbated by β-AR stimulation due to a further increase of the open probability of the RyR2 receptor by PKA and CamKII phosphorylation and an increase in SR calcium

load due to phosphorylation of PLN and subsequent activation of Serca2a, which can lead to a store overload-induced calcium release (SOICR)[143].

CPVT-causing Casq2 mutations, of which >20 have been found so far, are most commonly autosomal recessive, although autosomal dominant missense mutations have been identified as well[150,151].Casq2 is located in the SR lumen, binding calcium with high capacity and low affinity. Calcium binding to Casq2 induces dimerization and subsequent formation of double-helical Casq2 filaments, further increasing calcium binding capacity. Some, but not all, mutations have been found to have impaired calcium binding capacity, which leads to an increase in free calcium in the SR (Fig. 7D)[150]. In at least two autosomal dominant CPVT2 mutations, the filament formation has been found to be impaired (Fig. 7E)[152]. Another important function of Casq2, which is highly implicated in the proarrhythmic mechanism of Casq2 mutations, is its complex formation with RyR2, junctin and triadin. It has been shown that sensing of luminal calcium was impaired in the absence of Casq2 and the open probability of RyR2 at low luminal calcium concentrations was increased (Fig. 7F)[153]. Thus, an impaired interaction of Casq2 with its binding partners presents another mode of increased RyR2 calcium leak.

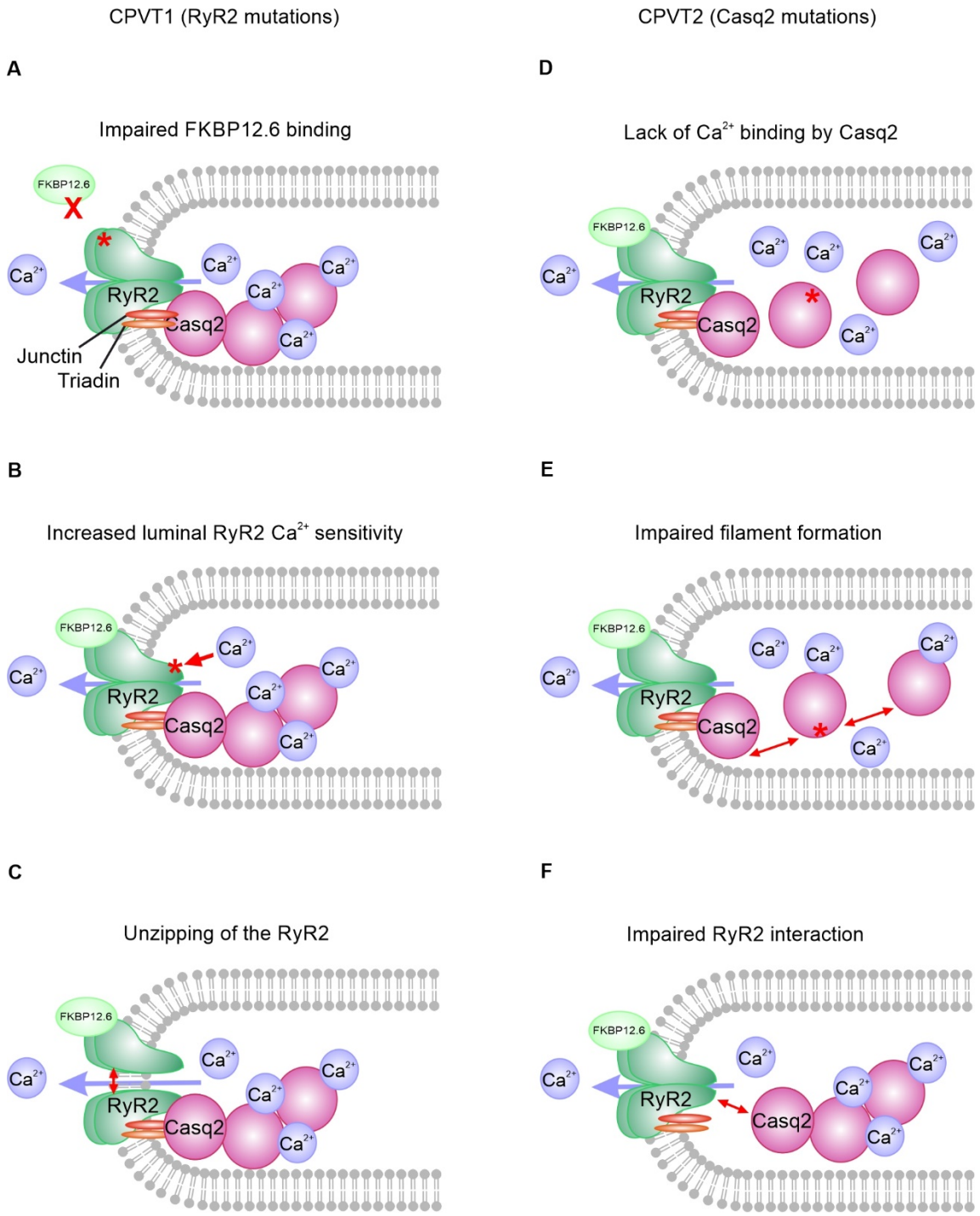

Figure 7: Molecular mechanisms of diastolic calcium leak in CPVT.
A-C) Schematic of the mechanisms of diastolic calcium leak caused by different RyR2 mutations in CPVT1. D-F) Schematic of the mechanisms of diastolic calcium leak caused by different Casq2 mutations in CPVT2. Red stars and arrows indicate side of mutation and influence on interacting molecules.

1.4 Optogenetic activation of G_s-signaling in the heart

1.4.1 Control of excitable tissue by optogenetics

The principle of optogenetics is to transgenically introduce light-sensitive proteins into cells and organisms to regulate a specific response via illumination, which provides unmatched spatial and temporal resolution compared with pharmacological substances. Although the first light-sensitive ion channels have been described as early as the 1970s[154], it was only in the early 2000s that optogenetics gained traction as an emerging field of research. In 2002 and 2003, Nagel et al. described the light-gated proton channel channelrhodopsin-1 (ChR1) and the light-gated cation channel channelrhodopsin-2 (ChR2) found in algae[155,156]. ChR2 was then successfully used to control mammalian neuron activity after lentiviral transduction[157]. From then on, optogenetics has been an integral method in the field of neuroscience.

Since cardiomyocytes can produce action potentials upon depolarization similarly to neurons, cardiology was the next field of research to adopt optogenetics. In 2010 Bruegmann et al. generated a transgenic mouse line expressing ChR2 under the CAG promotor and successfully used ChR2 to pace mouse hearts from locally distinct areas[158]. It was further shown that ChR2 can be used to defibrillate ventricular arrhythmias in mouse hearts[159].

This paper also showed the potential and limitations of optogenetics for therapeutic use. One of the major limitations in the translation of optogenetics from small organisms to larger mammals and eventual therapeutic use in humans is the penetration depth of light in tissue. Because light with a longer wavelength has deeper penetration depth than shorter wavelength light, there is a strong requirement for red-shifted optogenetics for potential future therapeutic applications.

Recently, optogenetics has expanded from light-gated ion channels to many other light-gated receptors, of which light-gated GPCRs are sought-after targets, as G-protein-signaling is one of the most abundant and diverse signaling pathways in the human body. In cardiomyocytes and the heart, optogenetic modulation of G_s-[160], G_i-[161] as well as G_q-[162,163]signaling has been successfully applied.

1.4.2 Optogenetic control of the adrenergic response in the heart

Two approaches have been explored for the optogenetic investigation of sympathetic signaling in the heart thus far: optogenetic activation of sympathetic neurons and direct optogenetic activation of β-adrenergic signaling in the cardiomyocytes. Sympathetic neurons have been targeted to express ChR2 using the tyrosine hydroxylase promoter, thereby enabling light stimulation of neuronal noradrenaline release in cardiac tissues to study the effects of sympathetic stimulation on heart function and

arrhythmias[65,164]. While optogenetically targeting the sympathetic neurons allows the investigation of the interplay between neurons and cardiomyocytes, it also limits the β-AR activation to the sides of endogenous innervation. Direct optogenetic activation of G_s-receptors in cardiomyocytes allows more precise spatial and temporal activation control. The first attempts to generate a light-sensitive G_s-coupled receptor have been performed by using the vertebrate rhodopsin – which naturally couples to $G_{i/o}$ in mammalian retina cells[165,166] – and replacing the intracellular part with the intracellular domain of the β2-AR[167,168]. These so-called OptoXR chimeric receptors successfully activated intracellular signaling cascades similar to the endogenous receptors regarding cAMP production and other downstream pathways[169]. There was, however, a significant drawback to the genetically engineered receptor in a strong bleaching effect, which can be associated with the conversion of cis-retinal to trans-retinal and subsequent decrease in available cis-retinal that is needed for rhodopsin photosensitivity[170].

In 2008 an opsin from the eye of the box jellyfish was identified, which exclusively couples to G_s and mediates light-induced cAMP production[171,172]. This jellyfish opsin (JellyOp) was first used as an optogenetic tool for light-induced G_s-signaling in mammalian cells by Bailes et al.[170]. It was found that the receptor is highly light sensitive compared to other optogenetic tools, but could produce higher amounts of cAMP than OptoXR and could be repeatedly activated in short intervals without any bleaching effect. This is likely due to a bi-stable nature, in which it can use cis- as well as trans-retinal to achieve photosensitivity.

Makowka et al. created a transgenic mouse line expressing JellyOp in cardiomyocytes under the CAG promotor. They found that it also coupled to G_s in cardiomyocytes and could modify heart function similarly to β-AR signaling in the heart[160]. The study showed the specificity of JellyOp to the G_s-signaling pathway in stem cell-derived cardiomyocytes and atrial tissue by measuring cAMP levels and frequency response. The characteristics of the JellyOp receptor and its confirmed function in transgenic mouse hearts makes JellyOp an ideal tool for the optogenetic investigation of local Gs-signaling effects in the heart.

1.5 Aim of the Thesis

Even though a number of antiarrhythmic drugs are currently on the market, sudden cardiac death due to ventricular arrhythmias still presents as one of the most common causes of death worldwide. On a cellular level, arrhythmias can be caused by an imbalance in the interplay between a range of ion channels creating depolarizing and re- / hyperpolarizing currents. On a whole organ level, a change in the organization and connectivity of different subtypes of cardiomyocytes can modulate the electric conduction to increase the risk of arrhythmia generation. β-blockers are one of the most effective antiarrhythmic drugs. This shows that a change in the cellular response to adrenergic stimulus, as e.g. observed in remodeling in heart failure, can be proarrhythmic, especially when the response is inhomogeneous within the organ. The SNS has distinct effects on different areas of the heart. In the SA node, adrenergic stimulation leads to increased heart rate, in the conduction system and the Purkinje cells it modulates excitability and conduction. In the ventricles it also increases contractile force. However, the effects of local adrenaline effects on the different heart areas have not been extensively studied in the whole organ. Therefore, the exact roles of the changes in heart rate, cell excitability and conduction by adrenergic stimulation on the generation of arrhythmias are not fully understood. Moreover, there might be distinct effects in the different areas of the ventricles, as endocardial and epicardial cardiomyocytes differ e.g. in APD and might have different sensitivities to adrenergic stimulation.

This thesis aims to expand the understanding of the proarrhythmic potential of local β-adrenergic signaling using the striking advantage of optogenetics over conventional pharmacological activation – its highly spatially and temporally defined activation by local illumination. Hereby, the influence of the trigger of the VT in the form of PVCs, but also the substrate of the VT, which defines the VT duration and complexity, were points of interest. For this investigation, transgenic mice expressing JellyOp, a G_s-coupled blue-light activated receptor were crossed with a CPVT mouse model carrying a Casq2 knockout mutation.

In Langendorff-perfused hearts of these mice, the local potential to generate an arrhythmic trigger through premature excitation was investigated for endocardial and epicardial tissue. Furthermore, the underlying differences in these tissues with regard to calcium handling and β-adrenergic signaling were investigated. The role of PDEs in the arrhythmic trigger potential and the expression and phosphorylation of calcium handling proteins were examined.

In order to investigate the role of β-adrenergic signaling on the substrate of arrhythmias, S1S2 electrical stimulation served as a premature trigger to elucidate the potential to induce reentry VT and their duration. Moreover, long-running VTs were induced by shortening the action potential duration

to investigate the complexity of a reentry VT upon G_s-stimulation. These analyses used ventricle-specific ECG recordings and voltage mapping of the epicardial surface to determine VT complexity. Sharp electrode measurements were performed to detect changes in action potential morphology.

2 Material and Methods

2.1 Laboratory equipment

Equipment	Specification	Supplier
Agarose gel chamber	Mini-Sub Cell GT	Bio-Rad
Autoclave		HSP steriltechnik AG
Automatic chlorider	ACL-01	Npi electronic
Balances	XS205 DualRange KB 1200-2N	Mettler Toledo Kern
Blotting system	Trans-Blot® Turbo™	Bio-Rad
Centrifuges	Micro Star 17R Mini Star	VWR VWR
Cryostat	CM3050 S	Leica
ECG recorder	Powerlab 8/35 Animal Bio Amp	AD Instruments
Electrical stimulator	Isolated pulse stimulator model 2100	A-M Systems
Electrophoresis chamber	Mini-PROTEAN® Tetra System with PowerPac™ Basic	Bio-Rad
Heated magnetic stirrer	MR Hei-Standard	heidolph
Ice machine	AF 80	Scotsman
Immunofluorescence imaging camera	Prime BSI	Photometrics
Immunofluorescence light emitting diodes (LEDs)	LedHUB	Thorlabs
Immunofluorescence microscope	Eclipse Ti2	Nikon
Integrating sphere	IS236A-4-SP1	Thorlabs
Laser	LuxX® 488-200	Omicron-Laserage
Laser in-line fiber filter mount	FOFMS/M-UV (250nm-450nm)	Thorlabs
LED control unit	DC2200	Thorlabs
Light catheter	CD-253-10-0	LifePhotonic GmbH
Liquid light guide, 3 mm, 340-800 nm	LLG3-6H	Thorlabs

Equipment	Specification	Supplier
Macroscope	MVX10 MV PLAPO 1x objective filter slider DSI-3PS-OL-UA	Olympus Olympus Mightex
Microliter syringe for Lugol ablation	50 µL SYR 705 RN	Hamilton
Micropipette Puller	P-1000	Sutter Instrument
Monochromator	Optoscan Monochromator with Optosource High Intensity ARC Lamp	Cairn Research
Optogenetic LEDs	LedHUB (460 nm) GCS-0470-50-A510 LED and BLS-13000-1 driver 470 nm M470F1	ThorlabsOmicron-Laserage Mightex Thorlabs
Peristaltic pump	Minipuls 3	Gilson
pH meter	765 Calimatic	Knick
Photodiode power sensor	S130c S170c	Thorlabs
Pipette controller	Pipetboy	Integra
Pipettes	Pipetman (P2, P20, P200, P1000)	Gilson
Powermeter	PM 100 A	Thorlabs
Red light lamp	KL 2500 LCD with red light filter	Schott
Sharp electrode setup		
Pipette holder	BNC type 1.0 mm OD	Heka
Bridge Amplifier	BA-01x	Npi
Micromanipulator	uMp-3	Sensapex
Touch screen control unit	uM-TSC	Sensapex
Rotary Wheel remote unit	uM-RW3/RW4	Sensapex
Stereo microscope	SMZ800N	Nikon
Stereo microscope light source	KL 1600 LED	Schott
Surgical instruments		
Narrow Pattern Forceps	11003-12	Fine Science Tools
Dumont #5 - Fine Forceps	11254-20	

Equipment	Specification	Supplier
Extra Fine Bone Scissors	14084-08	
Spring scissors	15003-08	
Temperature controlled perfusion cannula	TC02 (controller) PH01 (cannula)	Multichannel systems
Thermo shaker	MKR 23	Hettich Lab Technology
Tube roller mixer	SRT6D	stuart
Ultrasound bath	USC100T	VWR
Vacuum pump	vacusafe	Integra
Voltage mapping cameras		
PGH-1	acA720-520um	Basler
Di-4-ANEQ(F)PTEA	MiCam03-N256	Brainvision
Voltage mapping LED	SOLIS-660C	Thorlabs
Voltage mapping macroscope	THT macroscope MV PLAPO 1x objective	Brainvision Olympus
Vortexer	Vortex Genie 2	Scientific Industries
Water preparation system	Omnia-Pure-T UV-TOC	Stakpure
Western blot and DNA gel imager	ChemiDoc™ MP Imaging System	Bio-Rad
Wheaton™ micro tissue grinder 0.1 mL	357844	DWK Life Sciences

Table 1: Laboratory equipment

2.2 Imaging and optogenetic filters

Filter Type (Specification)	Use	Supplier (cat. no.)
Beam splitter T 515 LP	Voltage mapping with optogenetic illumination	AHF Analysentechnik (F48-515))
Cy3 ET Filter set Exc. 545/25 ET Band pass Beam splitter T 565 LPXR Em. 605/70 ET Band pass	Immunofluorescence imaging	AHF Analysentechnik (F46-004)

Filter Type (Specification)	Use	Supplier (cat. no.)
Cy5 ET Filter set Exc. 640/30 ET Band pass Beam splitter T 660 LPXR Em. 690/50 ET Band pass	Immunofluorescence imaging	AHF Analysentechnik (F46-009)
DAPI HC BP Filter set Exc. 377/50 BrightLine HC Beam splitter HC 409 Em. 447/60 BrightLine HC	Immunofluorescence imaging	AHF Analysentechnik (F36-500)
Neutral density filter (OD 1.0)	Optogenetic light reduction	Thorlabs (NDW10B)
PGH-1 filter Exc. 664/24 Band pass Beam splitter HC BS 685 Em. 795/188 Band pass	Voltage mapping	AHF Analysentechnik (F49-824) AHF Analysentechnik (F38-685) AHF Analysentechnik (F37-796)
Sputtered Enhanced Silver Mirror	Optogenetic light reflection	AHF Analysentechnik (F46-015)
YFP ET Filter Set Exc. 500/20 ET Band pass Beam splitter T 515 LP Em. 535/30 ET Band pass	Immunofluorescence imaging	AHF Analysentechnik (F46-003)

Table 2: Imaging and optogenetic filters

2.3 Consumables

Consumable	Supplier (cat. no.)
15 mL, 50 mL tubes	Greiner bio-one (188271, 227261)
4–20% Mini-PROTEAN® TGX Stain-Free™ Protein Gels, 10 well, 30 µl	Bio-Rad (#4568093)
4–20% Mini-PROTEAN® TGX Stain-Free™ Protein Gels, 15 well, 15 µl	Bio-Rad (#4568096)
Borosilicate glass capillaries	World Precision Instruments, Inc (1B100F-4)
Disposable needle 20G	Braun (4657519)
Exadrop® flow control	Braun (4061284)

Consumable	Supplier (cat. no.)
Histobond® microscope slides	Marienfeld (0810000)
ImmEdge® Hydrophobic Barrier PAP Pen	Vector (H-4000)
Immersion oil type N	Nikon
Microloader pipette tips	Eppendorf (5242956.003)
Microscope cover glasses 24x50mm	VWR (631-0146)
Multidirectional stopcock	Braun (4095111)
Original Perfusor® line	Braun (8255253)
Pipette tips	Diamond® Tower Pack™ (DL10, DL200, DL1000)
Seraflex® silk suture	Serag Wiessner (IC108000)
Silver wire	Science Products GmbH (AG-10T)
Trans-Blot Turbo Mini 0.2 µm PVDF Transfer Packs	Bio-Rad (#1704156)
Tygon tubes for roller pump (3.17 mm ID)	Ismatec (070534-251-ND)
VitraPOR™ micro filter candle with tube	Robu® (18103)

Table 3: Consumables

2.4 Chemicals and Reagents

Reagent	Supplier (cat. no.)
10x Tris/Glycine/SDS buffer	Bio-Rad (1610732)
10x Tris/Glycine/SDS Electrophoresis Buffer	Bio-Rad (#1610732)
2-Methylbutane	Sigma (M32631)
3M KCl	Knick (ZK0960)
4% formaldehyde	AppliChem (252931.1214)
4-(2-hydroxyethyl)-1-piperazineethanesulfonic acid (HEPES)	Sigma (H4034)
50x Tris-acetat-EDTA (TAE) buffer	Thermo Scientific (B49)
Agarose Standard	Roth (3810.3)
Aqua-Poly/Mount	Polysciences (18606-20)
Blebbistatin	Enzo (BML-EI315-0005)

Reagent	Supplier (cat. no.)
Calcium chloride ($CaCl_2$)	Merck (1.02378)
Carbamoylcholine chloride / carbachol (Cch)	Sigma (C4382)
Di-4-ANEQ(F)PTEA	Potentiometric Probes (33040)
Dimethyl sulfoxide (DMSO)	Sigma (D8418)
DirectPCR Lysis Reagent (Mouse Tail)	Viagen (102-T)
DL-Dithiothreit (DTT)	Roche (DTT-RO)
dNTP-Mix (2 mM)	Thermo Scientific (R0242)
Donkey Serum	Jackson ImmunoResearch (017-000-121)
GeneRuler Mix DNA ladder	Thermo Scientific (SM0333)
Glucose	Sigma (G7021)
Glycerol	Sigma (49757)
HDGreen™	Intas
Hoechst 33342	Sigma (B2261)
IBMX	Sigma (I7018)
Iodine (I_2)	Sigma-Aldrich (207772)
Isoprenaline (Iso) hydrochloride	Sigma (I5627)
L-Ascorbic acid	Sigma (A92902)
Magnesium chloride ($MgCl_2$)	Sigma (M8266)
Magnesium sulfate ($MgSO_4$)	Sigma (M7506)
PhosSTOP™ EASYpack	Sigma (4906845001) / Roche
Pierce™ ECL Western Blotting Substrate	Thermofisher (32106)
Pinacidil (hydrate)	Biomol (Cay15416)
Pittsburgh-1 (PGH-1)	Supplied by Guy Salama, Vascular Medicine Institute, University of Pittsburgh
Pluronic®-L64	Sigma (43449)
Potassium chloride (KCl)	Sigma (P9333)
Potassium iodide (KI)	Sigma-Aldrich (221945)
Potassium phosphate monobasic (KH_2PO_4)	Sigma (P5655)

Reagent	Supplier (cat. no.)
Precision Plus Protein™ All Blue Pre-Stained Protein Standard	Bio-Rad (#1610373)
Proteinase K 20 mg/mL	AppliChem (A4392)
Roti®fair phosphate buffered saline (PBS) 7.4	Roth (1112.2)
Serva Blue R	Serva (35051.02)
Skim milk powder	VWR (84615.0500)
Sodium azide (NaN_3)	Sigma (S2002)
Sodium bicarbonate ($NaHCO_3$)	Sigma (S5761)
Sodium chloride (NaCl)	Sigma (71376)
Sodium dodecyl sulfate (SDS) pellets	Roth (CN30.2)
Sodium hydroxide (NaOH)	Sigma (S8045)
Sucrose	Sigma (S0389)
Taq DNA-polymerase (5 E/µL), with 10x PCR buffer, $MgCl_2$ (50 mM)	Invitrogen (10342-020)
Thiourea (NH_2CSNH_2)	Sigma (T7875)
Tissue-Tek® O.C.T. compound	Sakura (4583)
Tris-(hydroxymethyl)-aminomethan (Tris)	Roth (4855.2)
Tris-hydrochloride (Tris-HCl)	Roth (9090.3)
Triton-X 100	Sigma (X100)
Tritrack 6x DNA loading dye	Thermo Scientific (R1161)
Tween® 20	Sigma (P9416)
Urea (NH_2CONH_2)	Sigma (U5128)

Table 4: Chemicals and Reagents

2.5 Solutions and buffers

HEPES perfusion buffer

	MW (g/mol)	Concentration (mM)
$CaCl_2$	110.99	1.8
Glucose	180.16	10
Hepes	238.3	10
KCl	74.56	5.4
$MgCl_2$	95.22	1
NaCl	58.4	140
Adjust to pH 7.4 with NaOH		

Table 5: HEPES perfusion buffer

Krebs-Henseleit (KH) buffer

	MW (g/mol)	Concentration (mM)
$CaCl_2$	110.98	1.8
Glucose	180.16	11
KCl	74.55	4.7
KH_2PO_4	136.07	12
$MgSO_4$	120.37	1.2
NaCl	58.44	118
$NaHCO_3$	84.01	18

Table 6: KH buffer

10x Tris-buffered saline with tween20 (TBST) (pH 7.5)

	MW (g/mol)	Concentration
Tris	121.14	0.5 M
NaCl	58.44	1.5 M
Tween® 20	1227.54	0.5 %
Adjust to pH 7.5 before adding Tween 20		

Table 7: 10x TBST (pH 7.5)

Protein isolation buffer

	MW (g/mol)	Concentration
Urea	60.06	8 M
Thiourea	76.12	2 M
SDS	288.38	3 %
Glycerol	92.09	10 %
Tris-HCl pH 6.8	121.14	0.05 M
DTT	154.25	75 mM (add fresh)
Add a few grains of serva blue		

Table 8: Protein isolation buffer

Lugol solution

	MW (g/mol)	Concentration
KI	166.00	10%
I_2	253.81	5%
Dissolved in KH buffer		

Table 9: Lugol solution

2.6 Antibodies

Primary antibodies

Antigen	Host and AB type	Supplier (cat. no.)	Use (dilution)
α-actinin	Mouse monoclonal IgG1	Sigma (A7811)	IF (1:400)
α-actinin	Rabbit polyclonal IgG	Abcam (ab137346)	IF (1:400)
PLN	Mouse monoclonal IgG1	Badrilla (A010-14)	WB (1:5000)
P-PLN (pser16)	Rabbit polyclonal IgG	Badrilla (A010-12AP)	WB (1:5000)
Rhodopsin (1d4)	Mouse monoclonal IgG1	StressMarq Bioscience (SMC-177C)	IF (1:100)

Antigen	Host and AB type	Supplier (cat. no.)	Use (dilution)
RRXS*/T*	Rabbit monoclonal IgG	Cell Signaling TECHNOLOGY (9624L)	WB (1:1000)
RyR2	Mouse monoclonal IgG1	ThermoFisher (MA3-916)	WB (1:1000)
Serca2a	Mouse monoclonal IgG2a	ThermoFisher (MA3-919)	WB (1:1000)

Table 10: Primary antibodies
(IF - Immunofluorescence; WB - Western Blot)

Secondary antibodies

Antigen	Conjugate	Supplier (cat no.)	Use (dilution)
Mouse IgG	Alexa Fluor™ 555	ThermoFisher (A31570)	IF (1:400)
Mouse IgG	Alexa Fluor™ 647	ThermoFisher (A31571)	IF (1:400)
Rabbit IgG	Alexa Fluor™ 555	ThermoFisher (A31572)	IF (1:400)
Rabbit IgG	Alexa Fluor™ 647	ThermoFisher (A31573)	IF (1:400)
Mouse IgG	Horseradish peroxidase (HRP)	Jackson ImmunoResearch Laboratories, INC. (115-035-146)	WB (1:10.000)
Rabbit IgG	HRP	Jackson ImmunoResearch Laboratories, INC. (111-035-144)	WB (1:10.000)

Table 11: Secondary antibodies
(IF - Immunofluorescence; WB - Western Blot)

2.7 Software

Software	Supplier	Use
BV workbench 2	SciMedia (Brainvision)	Voltage mapping analysis
CorelDRAW® 2019 Graphics Suite	Corel Corporation	Figure and schematic design
Fiji / imageJ	ImageJ	Image processing

Software	Supplier	Use
Graphpad Prism 8	GraphPad Software, Inc	Data analysis and statistical analysis
Image Lab 6.1	Bio-Rad Laboratories	Western blot analysis
LabChart 8 with ECG analysis module and peak analysis module	ADInstruments	ECG and sharp electrode recordings, ECG and action potential analyses, control of optogenetic and electrical stimulation
NIS-Elements AR 5 with General Analysis 3	Nikon	Fluorescence imaging and image analysis
Omicron control center v3	Omicron-Laserage	LED and laser control
Pylon Viewer 64-bit	Basler	Voltage mapping recording
OriginPro 8G	OriginLab Corporation	Data analysis

Table 12: Software

2.8 Experiments in explanted mouse hearts

2.8.1 Mouse lines

The animals used in this study were housed and bred in the animal facility "Haus für experimentelle Therapie" of the university clinic Bonn under specific pathogen-free conditions according to FELASA guidelines. Adult male and female mice were used in the experiments.

The JellyOp transgenic mouse line and the ChR2 mouse line were previously generated and established by our working group[158,160]. The Casq2 -/- mouse line was generated and published by Knollmann et al.[173]. The Casq2 -/- and JellyOp transgenic mouse lines were crossbred to generate JellyOp wt/tg (JellyOp pos.) x Casq2 +/- and further crossbred to generate JellyOp wt/tg x Casq2 -/- mice.

2.8.2 Genotyping of mouse lines

For Casq2 genotyping, tissue from ear punches was lysed and DNA was extracted. 100 µL of DirectPCR Lysis Reagent (Viagen) and 3 µL of proteinase K were added to the tissue. The tissue was lysed overnight at 55°C, 400 rpm, followed by inactivation at 85°C for 45 min. Lysate was then used for polymerase chain reaction (PCR). The PCR components for the sample preparation are detailed in Table 13 and the primers are shown in Table 14. The PCR protocol is specified in Table 15.

Substance	Amount (µL)
H_20	12.75
10x PCR buffer	2.5
dNTP-Mix (2 mM)	2.5
$MgCl_2$ (50 mM)	0.75
Primer 14550F	1
Primer 15777R	1
Primer 15605F	1
Taq DNA-polymerase	0.5
Sample DNA	2

Table 13: PCR components for Casq2 genotyping

Primer	Nucleotide sequence
156_CASQ Forward1 (14550F)	caccggcttccctgcctcccacagc
155_CASQ Reverse(15777R)	ccaccttaagagtttgcccacag
157_CASQ Forward2(15605F)	ggcagcagcctcctgtatgatag

Table 14: Primers for Casq2 genotyping

Step #	Temperature (°C)	Duration (s)
1	94	300
2	94	40
3	56	40
4	72	40 (go to 2 for 40x)
5	72	480
6	4	∞

Table 15: PCR protocol for Casq2 genotyping

Following PCR, agarose gel electrophoresis was performed. 2 % agarose gels were generated by dissolving 1 g agarose in 50 mL TAE buffer and heating until fully dissolved. 2µL HDgreen (Intas) was added. The gel was cast into a gel chamber (Bio-Rad). After polymerization, gels were placed into a running chamber filled with TAE buffer. 20 µL of PCR sample mixed with 4 µL of 6x loading buffer were loaded into a gel chamber. GeneRuler Mix (Thermo Scientific) DNA ladder was used as a DNA size marker. Electrophoresis was performed at 90 V for 60 min. Results were visualized using the ChemiDoc™ MP Imaging System (Bio-Rad).

A band at 280 base pairs represented the Casq2 knockout allele, a band at 172 base pairs represented the Casq2 wildtype allele.

For genotyping of JellyOp mice, ear punches were checked for green fluorescent protein (GFP) expression under the macroscope. ChR2 mice were used and genotyped as described in Bruegmann et al.[158].

2.8.3 *ECG recordings of explanted mouse hearts ex vivo*

Mice were sacrificed by cervical dislocation and hearts were excised. Excised hearts were transferred to chilled PBS and the aorta was cannulated by a 20 gauche, blunted cannula. Hearts were perfused

with HEPES perfusion buffer or KH buffer in Langendorff configuration via a custom constant-flow perfusion system consisting of a water bath to warm the buffer to 42°C, a peristaltic pump, and a heated perfusion cannula (set to 42°C) to reach a buffer temperature of 37°C when entering the aorta. Perfusion flow was set to 2 mL/min. HEPES buffer was oxygenated with 100% O_2 gas, KH buffer was oxygenated and pH adjusted to 7.4 with 95% O_2 / 5% CO_2 gas.

Bipolar ECG signals were detected by placing the apex of the heart onto a metal spoon, which served as the positive electrode, and placing a silver-chloride electrode at the aorta as the negative electrode. ECG was recorded at a sampling frequency of 10–20 kHz using a bio-amplifier recording system (PowerLab 8/35, Animal Bio Amp, LabChart 8 software, AD Instruments). Local ventricular ECG recordings were performed by placing the silver-chloride electrode directly onto the free wall of the respective ventricle as the positive electrode and using the spoon as the indifferent (negative) electrode. Heart rate and PQ interval were determined using the LabChart software with ECG analysis module.

2.8.4 Optogenetic stimulation of explanted mouse hearts

Epicardial illumination of explanted mouse hearts was performed via a macroscope (MVX10, Olympus) equipped with a 1x objective (MVPLAPO1x, Olympus) using a blue light LED attached to the epifluorescence port via a light guide (Thorlabs). For each experiment of the results section the used light source with corresponding illumination areas are summarized in Table 16. Blue light was directed onto the heart using a silver mirror placed in the filter slider (Mightex) of the macroscope. The illumination area was adjusted via the zoom function of the macroscope. Slit (Chapter 3.2) and half (Chapter 3.16) illumination were achieved by coupling the LED into the side port of the macroscope and placing either a focused custom-made inlet with adjustable slit width or a custom-made inlet with a half circular pattern filter into the light path at the field diaphragm plane.

Light intensity was regulated by controlling the voltage from the bio-amplifier and adjusting maximal intensity via the Omicron control center. Additionally, light could be reduced by the insertion of neutral density filters into the optogenetic light path. Light intensity was calibrated using a powermeter (PM100, Thorlabs) with a planar photodiode power sensor (S130A or S170C, Thorlabs). Light intensities are specified for each experiment in the corresponding results section.

Endocardial illumination was performed with a 360° illumination light catheter developed in cooperation with LifePhotonic GmbH (Bonn). The light catheter consisted of a light fiber with a cylindrical tip with a diameter of 500 µm and an illumination zone length of 4 mm, coated with light scattering particles. The light catheter was inserted by cutting a small incision into the respective

atrium and inserting the catheter through the atrio-ventricular valve into the ventricle. The light catheter was attached to a 488 nm laser (Omicron-Laserage). The laser was controlled by the Omicron control center and the Powerlab bio-amplifier system.

The light intensity of the catheter was measured using an integrating sphere (IS236A-4-SP1, Thorlabs). For this, the catheter was placed into the center of the integrating sphere and light intensity was detected using the powermeter.

Results section	**LED**	**Illumination area (zoom)**
Fig. 11	GCS-0470-50-A510 LED and BLS-13000-1 driver, Mightex	130 mm^2 (2x)
Fig. 12	470 nm M470F1, Thorlabs	2 mm slit illumination (1.25x)
Fig. 13, 31–37	460 nm LED Hub, Omicron-Laserage	38 mm^2 (4x)
Fig. 16–22, 24, 25	488 nm laser	360° endocardial illumination
Fig. 20–21, 24, 25	460 nm LED Hub, Omicron-Laserage	15 mm^2 (6.3x)
Fig. 30	GCS-0470-50-A510 LED and BLS-13000-1 driver, Mightex	38 mm^2 (4x)
Fig. 35-37	460 nm LED Hub, Omicron-Laserage	Half illumination (2x)

Table 16: Light sources and their use and specifications

2.8.5 Comparison of pharmacological and illumination-induced heart rate increase

The dorsal part of the right atrium (RA), where the SA node is situated, was illuminated with supramaximal light intensity (2 mW/mm^2, 90 s) to achieve maximal frequency increase during light stimulation (Fig. 11A-E). Subsequently, after the return of the frequency to baseline, the heart was perfused with isoprenaline (iso, 1 µM, 4 min) to measure maximal endogenous β-AR-induced frequency increase.

Frequency traces were smoothed with a triangular filter (Bartlett, 10 s window). The baseline frequency was defined as the maximal frequency of the smoothed data within a 45 s interval immediately before stimulation. The maximal frequency of the smoothed data after stimulation was used to calculate the maximal frequency increase relative to baseline.

Time to peak was determined as time from the start of illumination or Iso perfusion to increase to 80% of maximal frequency after the start of stimulation. Deactivation time was determined as time from end of illumination or Iso perfusion to decrease to 50% of maximal frequency.

Spectral sensitivity of JellyOp (Fig. 11F) was determined by generating 1 s long light pulses (10 µW/mm^2) with wavelengths of 400–700 nm in 50 nm steps and additionally 470 nm using a monochromator (OptoScan, Cairn-Research). The normalized heart rate increases (y) at applied wavelength λ were fitted with OriginPro software using the Govardovskii nomogram equation[174], which can be used as a general fit for the spectral sensitivity of visual pigments.

$$y=1/\{exp[A*(a-x)]+exp[B*(b-x)]+exp[C*(c-x)]+D\}$$

with $x=\lambda max/\lambda$, A=69.7, a=0.88, B=28, b=0.922, C=−14.9, c=1.104, D=0.674

Equation 1: Govardovskii equation for the spectral sensitivity of visual pigments. Equation and values taken from Govardovskii et al.[174]

With this fit the peak wavelength (λ_{max}) was calculated.

2.8.6 Investigation of ventricular arrhythmia generation

Hearts were Langendorff-perfused with either HEPES perfusion buffer or KH buffer to investigate ventricular arrhythmias during regular or pharmacologically reduced sinus rhythm. For pharmacological heart rate reduction, 1 µM Cch was added to the buffers and continuously perfused during the following application of either Iso or light.

Iso was applied in concentrations of 0.1–1 µM either by addition to the perfusion buffer or as a bolus injection with a 5 mL syringe into the aortic perfusion.

Light was applied onto the ventricle as described in Chapter 2.8.4. The corresponding results section specifies the duration and light intensities for each experiment.

For the investigation of arrhythmias at defined ventricular beating frequencies, atria were removed during Langendorff-perfusion using spring scissors. Ventricles were then paced with a bipolar silver electrode connected to an isolated pulse stimulator. Hearts were paced with electrical pulses of 1 ms duration and 1–3 V intensity, at either 200 bpm or 400 bpm.

To investigate the inducibility of VT after a premature trigger, S1S2 electrical stimulation was applied. For this, a bipolar silver electrode was placed on the RV base and 6 S1 pulses with 150 ms cycle length, followed by an S2 pulse with reduced cycle length were applied (1 ms, 1-3 V). S2 pulses were reduced by 5 ms until no QRS complex was induced (no capture) to determine the capture threshold.

2.8.7 Endocardial ablation

Ablation of the endocardium of a Langendorff-perfused mouse heart was performed by bolus injection of 7 µL Lugol solution, consisting of 5% I_2 and 10% KI in perfusion buffer, directly into the left ventricle (LV) using a glass microliter syringe (Hamilton). Langendorff-perfusion was continued during the injection. Experiments on ablated hearts were continued 8 min after ablation. Hearts that were not electrically paceable after ablation were excluded from the experiments.

2.8.8 Ventricular arrhythmia analysis

For hearts in intrinsic sinus rhythm, a PVC was determined as an ectopic beat with a deformed QRS complex without preceding P-wave. For electrically paced hearts, a PVC was determined as an ectopic beat not immediately preceded by an electrical stimulus (seen on the ECG as a large, short artifact correlating with the electrical stimulation). To visualize and count PVCs, a corrected ECG signal was generated in Labchart by blanking the first 50 ms after the start of electrical stimulation to 0 mV to remove the regularly paced QRS complexes. For analysis of PVC incidence by endocardial and epicardial illumination, PVCs occurring in a 30 s interval after and before illumination were counted. PVC count/s was defined as PVC count after illumination subtracted by PVC count before illumination divided by time (30 s).

A junctional arrhythmia was defined as a series of regularly shaped QRS complexes without a preceding P-wave, at a higher frequency than sinus rhythm. Triggered VT was determined as a series of monomorphic, abnormally-shaped QRS complexes in fast succession (faster than intrinsic sinus rhythm) but with a return to the isoelectric line between beats. Reentry VT was characterized by monomorphic or polymorphic ECG signals without return to the isoelectric line between beats, indicating continuous electrical propagation. Frequency characteristics of reentry VT were further analyzed using the spectrum function in LabChart to create Fast Fourier Transformations (FFT). The ECGs were recorded at a sampling frequency of 20 kHz and the following spectrum analysis parameters were selected: FFT size: 16384; Data window: Hann (cosine-bell); overlap: 50%; mode: amplitude. For quantification of the high frequency component, the standard deviation (SD) of the high frequency

including the second harmonic of the dominant frequency was calculated in LabChart (lower frequency limit: 30-40 Hz, upper frequency limit 100 Hz). Mean SD of the high-frequency component in a 30 s interval before illumination was defined as baseline. The mean SD of the high-frequency component in a 30 s interval from the start of illumination was defined as illuminated.

2.8.9 PDE inhibition in Langendorff-perfused mouse hearts

PDE inhibition was performed by continuous perfusion with 1–3 µM IBMX in KH buffer. Atria were removed and ventricles were electrically paced as described in Chapter 2.8.6. Light-dose responses of PVC count were generated by applying a 1 s long light pulse every 30 s with increasing light intensities (endocardial: 0.0035–1.09 mW/mm^2; epicardial: 0.35–11.9 mW/mm^2). Baseline was defined as PVC count/s in a 30 s interval before the first light pulse. For each light pulse, PVC/s was determined in a 30 s interval from the start of illumination. For corrected PVC count/s baseline PVC count was subtracted from the PVC count after illumination. Dose-response curves of corrected PVC count/s were fitted using the Hill1 equation (OriginPro, nonlinear fit, Growth/Sigmoidal).

2.8.10 Pacing threshold in ChR2 hearts

ChR2 hearts were Langendorff-perfused with KH buffer and subsequently with HEPES buffer. Endocardial and epicardial illumination was applied as described in Chapter 2.8.4. 20 consecutive light pulses of 10 ms duration at 400 bpm were applied onto the LV. Pacing threshold was defined as the minimum light intensity needed to trigger a QRS complex with each of the last 10 light pulses. The pacing threshold was determined three times for each condition per heart and averages were calculated.

2.8.11 Sharp electrode measurements

Cardiac action potential recordings were performed using sharp microelectrode. Hearts were perfused in Langendorff configuration and ECG recordings were performed as described in Chapter 2.8.3. To abolish contraction movements 10 µM blebbistatin was added to the perfusion buffer.

Sharp microelectrodes were produced from borosilicate glass capillaries with a micropipette puller (P-1000, Sutter Instrument) with the following program settings: Heat = 519; Pull = 80; Velocity = 125; Time = 250; Pressure = 500; Ramp = 514.

Microelectrodes were filled with 3 M KCl solution and attached to a micromanipulator (Sensapex) with a fast piezo actuator. A bridge amplifier (Npi) was used for signal amplification, which was recorded using the Powerlab system. The microelectrode was inserted into the LV free wall and moved forward until a stable resting membrane potential of < -60 mV was detected. Cardiac action potentials were analyzed using the LabChart peak analysis module with Cardiac Action Potential analysis routine.

For the analysis of the influence of G_s-activation on action potential parameters, ventricles were electrically paced with an interpulse period of 205 to 185 ms and baseline action potential parameters were measured as average over the last 2 s before the start of illumination. An area of 38 mm^2 on the LV free wall, including the insertion side of the microelectrode, was illuminated for 30 s with 0.83 mW/mm^2 as described in Chapter 2.8.4. Illumination action potential parameters were defined as average values in a 2 s interval around the maximal effect after illumination.

2.8.12 Voltage mapping

Mouse hearts were perfused in Langendorff configuration with HEPES buffer at 2 mL/min containing 100 µM blebbistatin to inhibit contraction movement. Voltage mapping of hearts during S1S2 electrical stimulation (Fig. 33) was performed using the red-light voltage-sensitive dye Di-4-ANEQ(F)PTEA to measure conduction velocity. Voltage mapping of long-running VTs (Fig. 34) was performed using the red-light voltage-sensitive dye PGH-1.

100 ng Di-4-ANEQ(F)PTEA dissolved in 50 µL EtOH was placed in an ultrasound bath for 10 min and dissolved in 2.5 mL perfusion buffer. The heart was perfused with dye solution for 2.5 min at 1 mL/min flow rate, then the flow rate was increased again to 2 mL/min, before perfusion was switched from constant flow to constant pressure perfusion to remove movement artifact from the peristaltic pump. Voltage mapping was performed at 1 kHz and 47.8 µm pixel size with 660 nm excitation and the PGH-1 filter set and recorded with a MiCam03-N256 camera (Brainvision) using the BV workbench (Brainvision) software.

20 µL of 2 mM PGH-1 dissolved in 84% DMSO and 16% Pluronic were added to 500 µL HEPES buffer and manually applied as a bolus to the aortic perfusion via a 1 mL syringe. Excitation light using a 660 nm LED was coupled to the epifluorescence port of the macroscope with the PGH-1 filter set (Table 2), while the optogenetic stimulation was applied via the side port (Fig. 8). Images were recorded using a CMOS camera (Basler) and pylon viewer (Basler) software at 500 fps. Images were binned with 8x8 averaging (ImageJ), resulting in a final pixel size of 164 µm.

Recordings were further analyzed using BV workbench (Brainvision) software. Filters were applied (PGH-1 imaging: 5x5 Gaussian Blur; invert polarity, drift removal with 3 degree polynomial fit, finite impulse response filter with fc = 100 Hz; Di-4-ANEQ(F)PTEA imaging: 5x5 Gaussian Blur, invert polarity). Frequency analysis for dominant frequency maps, phase analysis for phase maps and activation time of the peak analysis for generating activation maps were performed. Conduction velocities were measured in BV workbench via line selection along the axis of wave transmission on the anterior ventricular wall.

To generate a long-running, stable VTs, hearts were perfused with HEPES perfusion buffer containing 100 µM pinacidil. VTs were then induced by electrical burst stimulation (1 ms pulses, 20 Hz, 2 s). After a stable running VT was induced, voltage mapping was performed every 10 s for 2 s intervals. After the first 2 s imaging, a light pulse was applied either onto the whole anterior ventricular wall or onto the left or right ventricle using a half circular pattern filter.

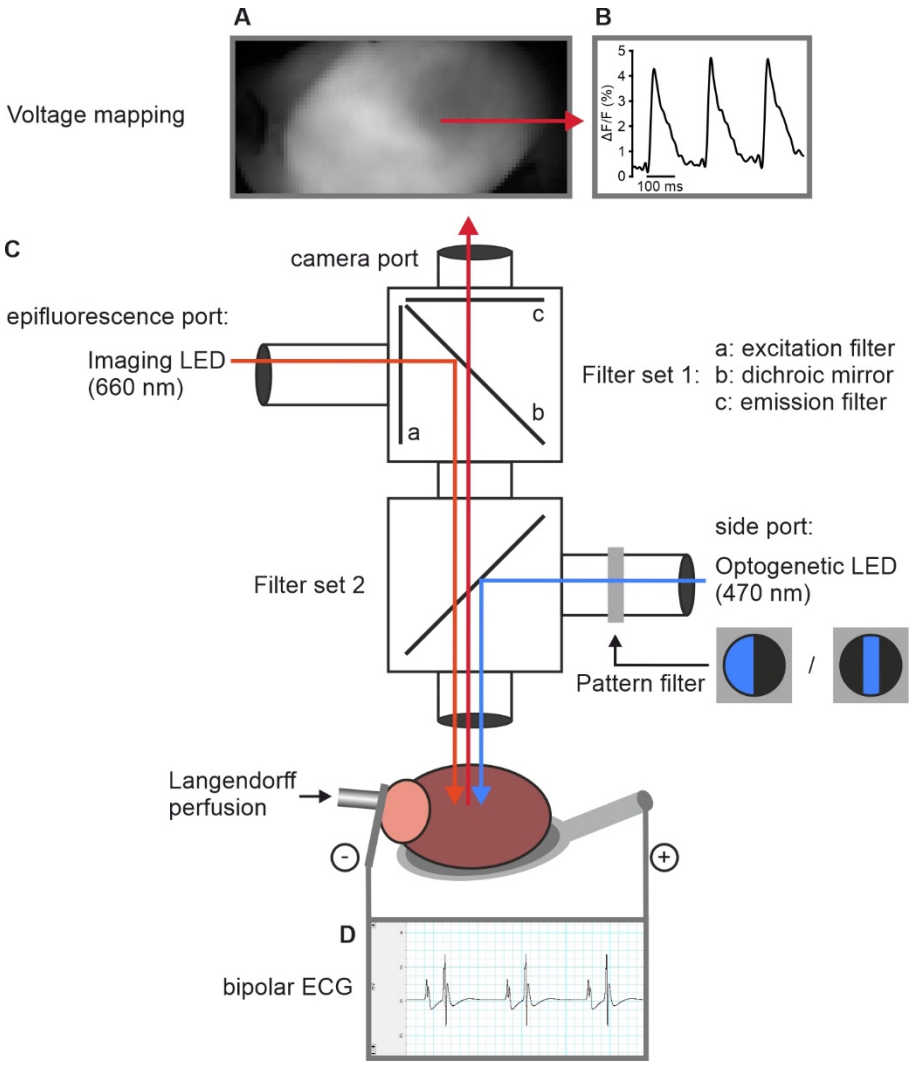

Figure 8: Voltage mapping of explanted mouse hearts.
A) Exemplary voltage mapping image. B) Exemplary raw trace of action potential recordings. B) Schematic drawing of the voltage mapping setup used for simultaneous optogenetic stimulation in explanted, Langendorff-perfused mouse hearts. The voltage mapping LED is coupled to the epifluorescence port of the macroscope. Filter set 1: PGH-1 filter. The optogenetic LED is coupled to the side port with adjustable pattern filter insert. Filter set 2: 515 nm beam splitter. D) Exemplary ECG trace LabChart recording.

2.9 Immunohistochemical analysis

2.9.1 Generation of heart tissue slices for immunostainings

Lugol-ablated hearts (Chapter 3.8) were immunostained after the experiment. Mouse hearts for determination of JellyOp expression (Chapter 3.9) were perfused in Langendorff configuration for 10 min with HEPES buffer before further processing. Hearts were fixed with 5 mL 4% formaldehyde via aortic perfusion and incubated overnight in 5 mL 4% formaldehyde at 4°C in a 15 mL tube. Hearts were transferred to 5 mL 20% sucrose + 0.03% sodium azide in PBS and stored 2 days at 4°C or until the hearts had sunk to the bottom of the 15 mL tube. Subsequently, hearts were frozen on dry ice in 2-methylbutane, precooled at -80°C. Hearts were then stored at -80°C until cryo-sectioning. Heart sections were cut using a cryostat (Leica) with a cryochamber temperature and specimen temperature of -22°C and a section thickness of 8 µm. Slices were stored at -20°C until immunofluorescence staining.

2.9.2 Immunofluorescence staining of heart slices

Slices were thawed for 5 min at room temperature (RT). Slices were then rehydrated with PBS for 5 min, before permeabilization with 0.2% Triton-X in PBS. A blocking solution of PBS containing 5% donkey serum was applied for 30 min. First antibodies were incubated for 2 h at RT diluted as stated in Table 10 in blocking solution. Slices were washed 3 times for 10 min with PBS and secondary antibodies were applied for 1 h at RT in the dark diluted as stated in Table 11 in PBS containing 1 µg/mL Hoechst. Slides were mounted with coverslips using mounting medium Aqua/polymount and dried overnight at 37°C.

2.9.3 Imaging of immunofluorescence stained heart slices

Immunofluorescence stainings were imaged using a fluorescence microscope (Nikon) using NIS elements software (Nikon). Filters and corresponding light sources used for imaging are specified in Table 2. For imaging of the left ventricular free wall, stitched images were generated with a 40x oil objective and using the large image function with optimal path stitching with 2 % overlap.

To determine transmural GFP signal intensity differences (Fig. 23C) a custom GA3 analysis module was generated (Fig. 9A). The analysis module detected the lumen to endocardial border, marked in Fig. 9B+C as the cyan line, using a homogenized α-actinin (Cy5) signal. Furthermore, the α-actinin signal was used to subdivide the LV free wall into random regions (red outlined sections in Fig. 9B+C) and the distance of the center of each region to the lumen border was calculated. Based on this distance,

regions were classified as endocardial (0-299 µm distance to lumen), mid-myocardial (300-599 µm distance to lumen) and epicardial (≥600 µm distance to lumen). The mean GFP intensity of each region was calculated and normalized to mean α-actinin signal intensity.

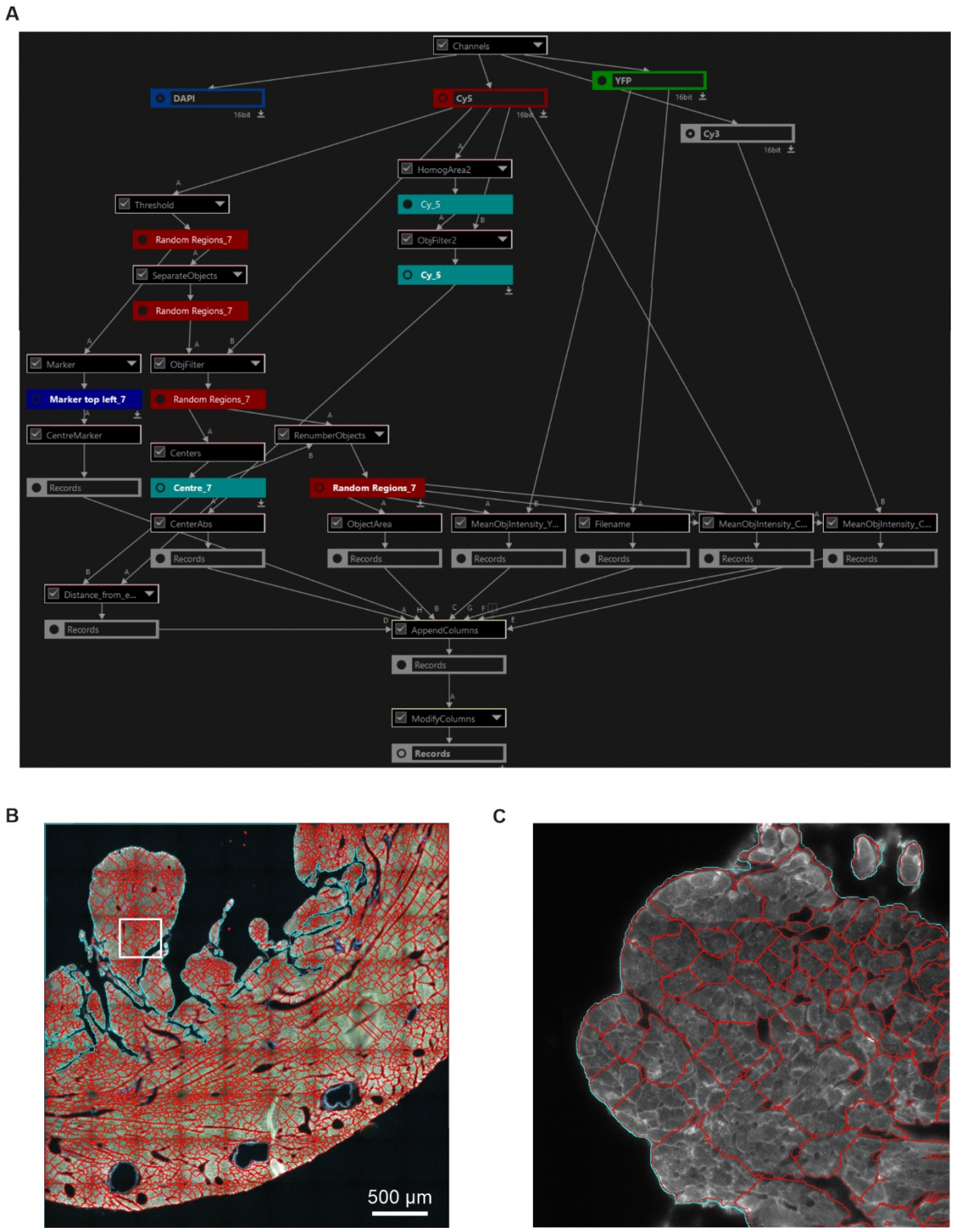

Figure 9: NIS elements GA3 recipe for JellyOp expression analysis.
A) GA3 recipe for the detection of the endocardial border, division of the ventricular wall into regions according to α-actinin signal (Cy5) and calculation of mean signal intensities in each channel and distance of the center of the region from the endocardial border. B) Immunofluorescence image of the LV free wall after GA3 analysis. Cyan line: detected endocardial border, red lines: random regions generated by the analysis. C) Excerpt of the image in B (indicated by white box). Displayed is the 1d4 signal (Cy3, white) and the GA3 analysis overlay.

2.10 Protein analysis

2.10.1 Protein isolation for Western Blot

Hearts were perfused in Langendorff configuration for 5-10 min with Hepes perfusion buffer. For Iso stimulation, hearts were thereafter perfused with Hepes buffer containing 100 nM Iso for 5 min, while unstimulated hearts were perfused with normal Hepes buffer for an additional 5 min. Hearts were then placed in chilled Hepes buffer containing PhosStop (Roche, 1 tablet dissolved in 1 mL ddH_2O, diluted 1:10) to preserve phosphorylation. The ventricular free wall was excised with scissors under a stereomicroscope. The LV free wall was then placed on a specimen disc with the epicardial side down onto a pre-frozen and evenly cut layer of embedding medium (Tissue-Tek, Sakura). The heat extractor of the cryostat was pressed onto the endocardial side of the LV free wall until the tissue was completely frozen (Fig. 10). With the cryostat, slices of 100 µm thickness were cut off. The first 300 µm of endocardial tissue was collected in a pre-chilled micro tissue grinder and 100 µL of protein isolation buffer was added. Tissue was manually homogenized in the tissue grinder and transferred to a 1.5 mL tube chilled on ice. This step was repeated once with an additional 50 µL of protein isolation buffer. The next 500 µm of tissue was cut off and discarded. Another 300 µm was collected as mid-myocardial sample and processed as described for the endocardial sample. The tissue lysates were stored at -80°C until further use.

For protein measurements, 2 µL of each sample were used for gel electrophoresis as described in the following chapter (2.10.2) and stain-free imaging followed by quantification with Image Lab software (Bio-Rad) was performed.

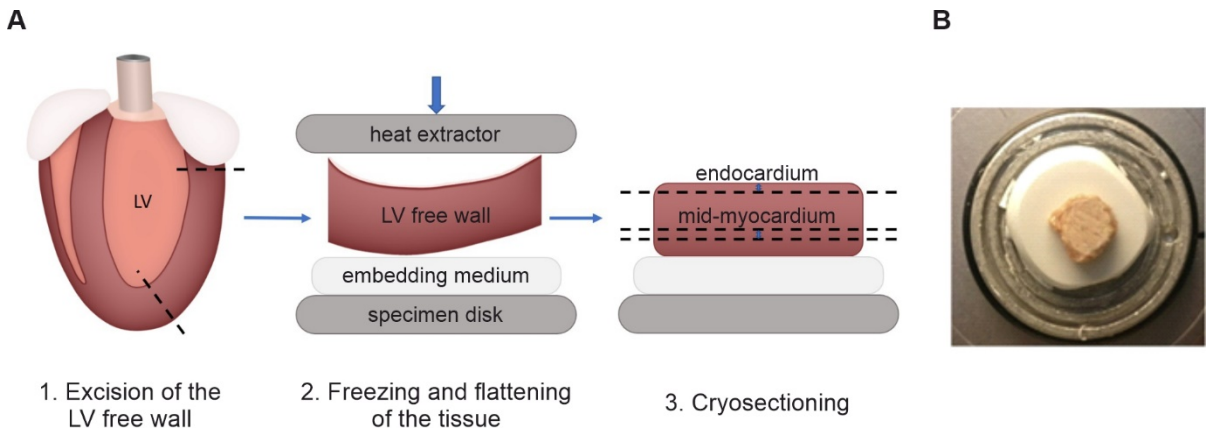

Figure 10: Sample collection of endocardial and midmyocardial tissue.
A) Schematic of the process of tissue collection from the LV free wall. The LV free wall is excised, flattened and frozen epicardial side down, before cryo-sectioned and used for further tissue processing. B) top view of the endocardial surface of the LV free wall attached with embedding medium to the specimen disk after freezing and flattening, before cryo-sectioning.

2.10.2 Gel electrophoresis

Gel electrophoresis was performed using a Mini-PROTEAN® Tetra System (Bio-Rad) electrophoresis chamber. Pre-cast stain-free gradient gels (4-20% SDS) were used for all experiments. 15 µg of the sample were added to a total lysis buffer volume of 10 µL and heated for 5 min at 95°C and briefly centrifuged, before loading onto the gel. 4 µL of protein marker (All blue pre-stained protein ladder, Bio-Rad) was used for determination of molecular weight. Electrophoresis was performed at 60 V for 20 min, then at 120 V until the sample front reached the bottom of the gel.

2.10.3 Western Blot

For protein transfer from the gel onto a western blot membrane, Trans-Blot Turbo Mini 0.2 µm PVDF Transfer Packs (Bio-Rad) were assembled according to manufacturer instructions. The transfer was performed by a Trans-Blot® Turbo™ blotting system (Bio-Rad) using the High MW Bio-Rad program (10 min, 1.3 A). After transfer, the membrane was imaged for stain-free normalization. Then, the membrane was blocked for 1 h at room temperature in 5% skim milk in TBST. Primary antibodies were diluted in 5% skim milk in TBST, as stated in Table 10 and incubated overnight at 4°C on a tube roller mixer. Membranes were washed 3x for 20 min in TBST and HRP-conjugated secondary antibodies, diluted in 5% skim milk in TBST as stated in Table 11 were incubated for 2 h at room temperature. Membranes were washed 3x for 20 min in TBST before adding 1 mL of HRP substrate (Thermofisher) onto the membrane, incubating for 2 min and imaging chemiluminescence signal with the western blot imager (ChemiDoc™ MP, Bio-Rad).

2.11 Statistical analysis

All statistical testing was performed using Graphpad prism 8. For the comparison of two groups with equal variances, unpaired student's t-test was performed. For two groups with different variances (according to F test), Welch corrected unpaired t-tests were performed. For testing between a group at two conditions (e.g. baseline and illumination) paired student's t-test was performed. For multiple group comparison with equal variances ordinary one-way ANOVA with Tukey's post-test was performed. For groups with different variances (according to Brown-Forsythe test), Brown-Forsythe and Welch ANOVA with Dunnett's T3 post-test was used. For multiple group comparison with matched data, repeated measures (RM) ANOVA with Tukey's post-test was performed. For each experiment, the applied test is stated in the corresponding figure legend. P-values of statistical differences between groups are marked with asterisks as follows: *: $p<0.05$; **: $p<0.01$; ***: $p<0.001$; ****: $p<0.0001$.

3 Results

3.1 Comparison of JellyOp activation with activation of endogenous β-adrenergic response in the heart

While some insights on local G_s-effects in the heart have been gained from optical mapping or single-cell studies, regional-specific activation of G_s-signaling within the intact ventricle is challenging to achieve with high precision using pharmacological agents[175,176]. Furthermore, computational modeling revealed distinct effects of G_s-activation kinetics on the induction and morphology of arrhythmias[177], which have thus far not been experimentally studied as the speed of pharmacological application in the whole heart is low. Thus, optogenetic G_s-activation was used in the current study to investigate highly locally and temporally defined β-adrenergic effects on cardiac arrhythmia mechanisms.

The mouse line used in this thesis for optogenetic activation of the G_s-signaling pathway was previously generated by Makowka et al. from a transgenic G4 mouse stem cell line[160]. This mouse line expresses JellyOp-IRES-GFP under the CAG promotor, whereby GFP is located diffusely in the cells and JellyOp is expressed at the cell membrane, acting as a light-sensitive G_s-coupled GPCR. The study by Makowka et al. showed the specificity of JellyOp to the G_s-signaling pathway in stem cell-derived cardiomyocytes and atrial tissue by measuring cAMP levels and frequency response. A dose-response curve in Langendorff-perfused JellyOp pos. hearts displayed a half-maximal effective light intensity (ELi50) of approx. 390 µW/mm^2 and a maximal heart rate increase at light intensities > 2 mW/mm^2 with a pulse duration of 100 ms.

As part of this previous publication and as the first line of experiments for this thesis, the light-induced G_s-activation by JellyOp was quantified and compared to the endogenous β-adrenergic G_s-receptor activation. For this, JellyOp pos. excised mouse hearts were Langendorff-perfused and ECG signals were recorded. Illumination of the dorsal RA, where the SA nodal region is located, with supramaximal blue light (2 mW/mm^2, 90 s) induced a peak heart rate increase by 44.0 ± 4.1% (Fig. 11A). Subsequently, hearts were perfused with a supramaximal dose of the β-AR agonist Iso (1 µM, 4 min). Iso perfusion led to a comparable heart rate increase of 58.1 ± 4.4% (Fig. 11B) with a slightly higher maximal effect than illumination (Fig. 11C). The long illumination time also allowed a comparison of Iso perfusion and illumination regarding activation time and decay after end of illumination or Iso wash-out. The kinetics of the heart rate response were significantly faster after illumination compared to Iso perfusion with an average time to 80% of peak of 15.6 ± 3.3 s during illumination compared to 83.2 ± 11.2 s during Iso perfusion (Fig. 11D). The average deactivation time to 50% of maximal effect after termination of

illumination was 19.6 ± 9.7 s, much faster than the significantly delayed turn-off after Iso wash-out of 1283 ± 178.5 s (Fig. 11E). Of note is also the higher occurrence of arrhythmic events in the original traces after Iso perfusion compared to illumination (grey traces in Fig. 11A,B), especially in the early phase of perfusion with iso. This indicates an activation of other areas of the heart with Iso that are transiently promoting ectopic beats. Such a remote effect was prevented by regional-specific JellyOp activation solely in the SA nodal region of the RA.

The light response of the JellyOp mouse line was further characterized by investigating the spectral sensitivity of the heart rate response. For this, the dorsal RA was illuminated with light with increasing wavelengths from 400 to 700 nm at submaximal light intensities to avoid saturation at the most sensitive wavelengths (50 nm steps, 10 µW/mm^2, 1 s). The maximal heart rate increase was determined (Fig. 11F) and the response spectrum was fitted with the Govardovskii equation previously described for visual pigment absorbance spectra[174]. With this fit, a peak effect at a wavelength of 493 nm was calculated. Above 600 nm, no light response was detected, which makes JellyOp compatible with far-red imaging dyes, as used in later chapters for voltage mapping.

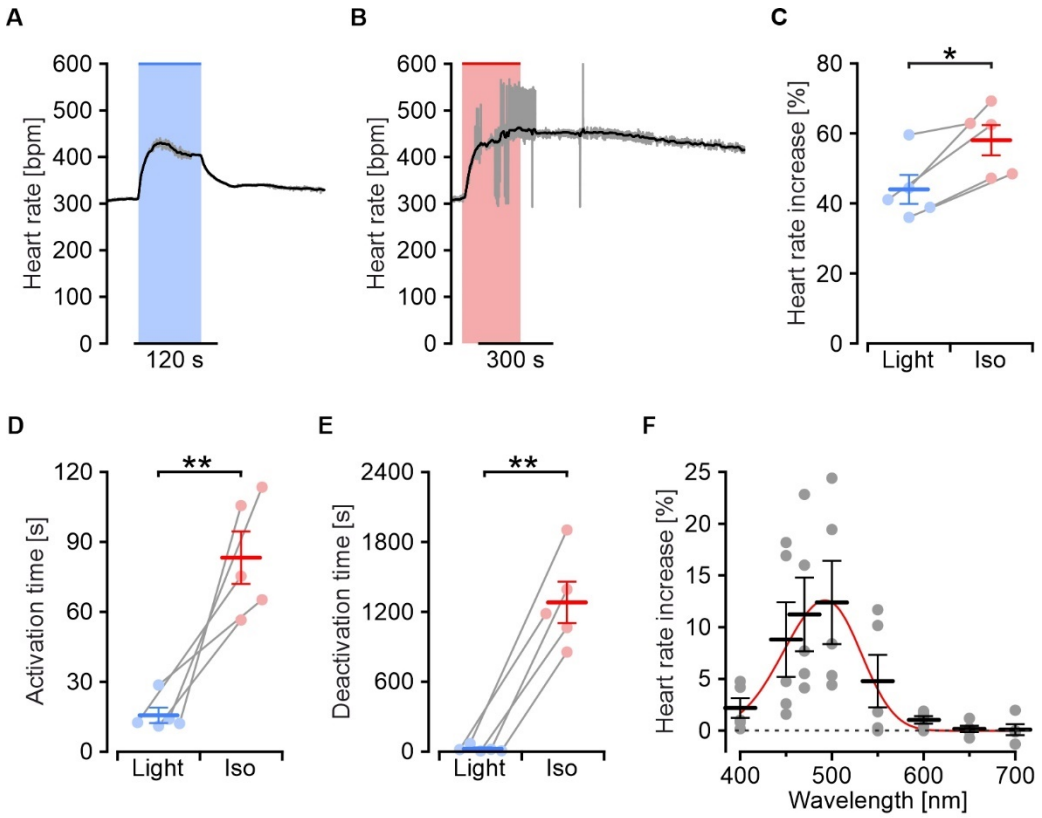

Figure 11: Comparison of JellyOp activation with activation of endogenous β-AR in the Langendorff-perfused mouse heart.
A) Heart rate response upon illumination of the dorsal right atrium of a JellyOp pos. Langendorff-perfused mouse heart (blue bar; 470 nm, 90 s, 2 mW/mm^2); grey line = original traces; black line = averaged traces. B) Heart rate response in the same heart as A upon perfusion with Iso (red bar; 4 min, 1 µM). C-E) Maximal heart rate increase (C), time to maximal response (D) and deactivation time (E) upon supramaximal activation of JellyOp compared to Iso (N=5; grey lines correspond to same heart; paired student's t-test). F) Maximal heart rate increase in relation to the light spectrum, with wavelengths applied from 400 – 700 nm (50 nm steps, 10 µW/mm^2, 1 s). Spectral sensitivity was fitted with the Govardovskii equation (red line, R^2 = 0.98; N=5)

3.2 Regional G_s-effect on ectopic pacemaking activity

In order to investigate regional effects of G_s-activation on arrhythmias, a CPVT mouse model generated by Knollmann et al.[173], was crossed with the JellyOp mouse line. This CPVT mouse line carries a Casq2 null allele, which has a deletion of the promotor and exon 1, thus expressing no functional Casq2 from this allele. Previous characterization of the mouse showed the occurrence of PVCs and VTs upon stimulation with Iso in anesthetized mice *in vivo*.

The effect of local G_s-activation was first investigated in Casq2 +/- JellyOp pos. mice. The anterior side of a Langendorff-perfused heart of a Casq2 +/- JellyOp pos. mouse was illuminated with a slit illumination of 2 mm width to selectively illuminate three specific areas: 1) the atria, including the SA node, 2) the AV septal area, including the AV nodal region and 3) the ventricles (Fig. 12A). Atrial

illumination resulted in an increase in heart rate and the occurrence of supraventricular arrhythmias, indicating the activity of ectopic pacemakers in the atria (Fig. 12B). Ectopic beats had a notably shorter PQ interval duration and a distinct P-wave morphology (Fig. 12B,E). Illumination of the AV septal area resulted in a heart rate increase, with progressive shortening of the PQ duration, until the QRS complex occurrence was faster than the atrial activity (Fig. 12C). QRS complex shape remained unchanged, indicating pacing by the AV node or upper ventricular conduction system, known as junctional arrhythmias (Fig. 12F). Ventricular illumination prompted only a slight increase in heart rate and reduction in PQ interval, which shows a minimal illumination of the SA node and AV node by scattered light (Fig. 12D). The heart remained in sinus rhythm throughout (Fig. 12G).

Together these experiments using local illumination show that specific regional activation has distinct influences on heart rate and pacemaking activity measurable by ECG recordings in Langendorff-perfused mouse hearts, with only slight off-target effects through scattered light on other regions. However, there was no induction of VTs by illumination of the Casq2 +/- JellyOp pos. mice (N=8), while junctional arrhythmias occurred equally in Casq2 +/+ (5 out of 12) and Casq2 +/- (4 out of 8) JellyOp pos. mice.

As Casq2 -/- mice have been reported to have a stronger phenotype than Casq2 +/- mice[178], Casq2 -/- mice were generated and used in the continuation of the thesis.

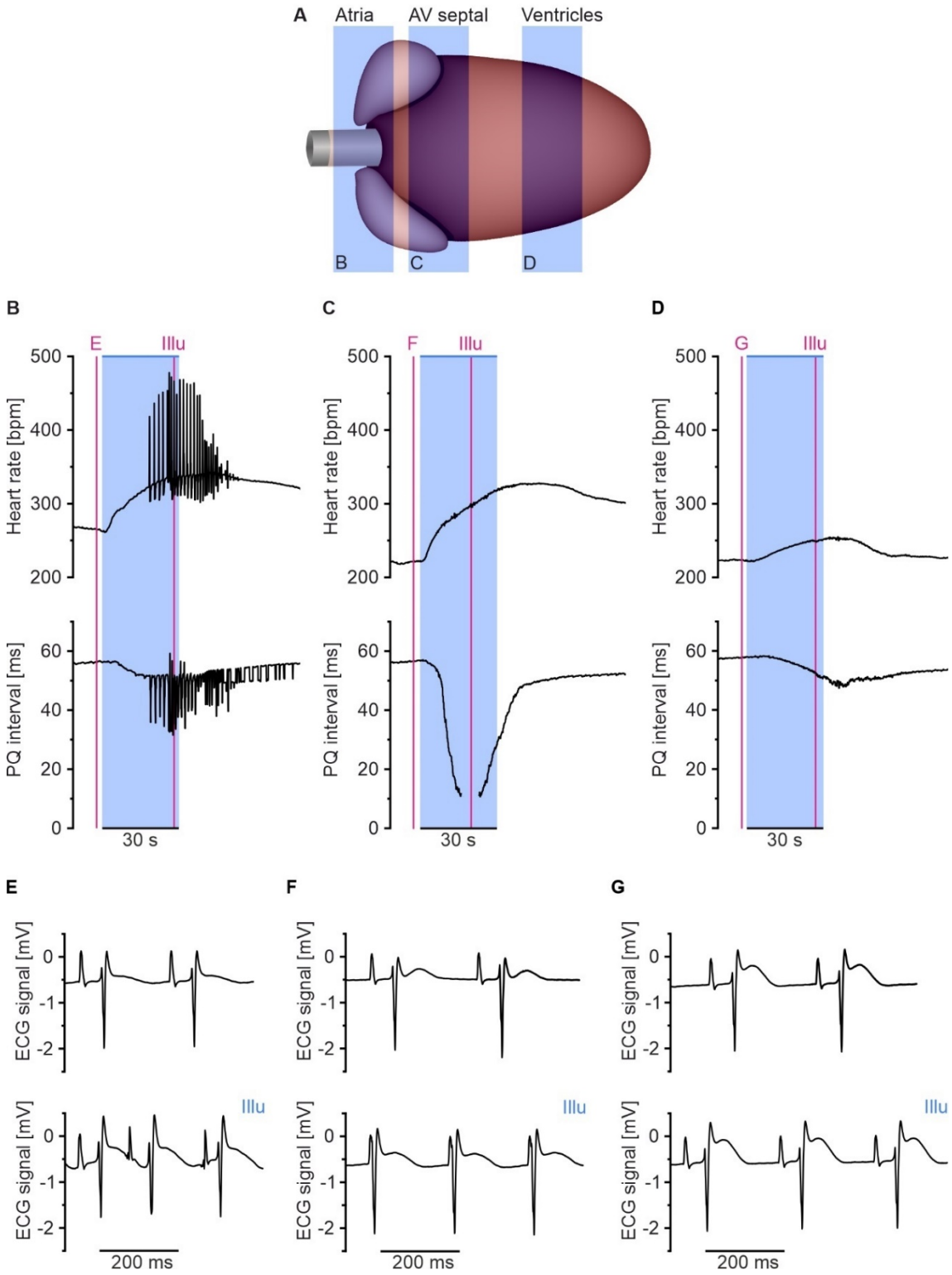

Figure 12: Effect on ectopic pacemaking activity by regional JellyOp activation.
A) Schematic of a Langendorff-perfused Casq2+/- JellyOp pos. heart illuminated by slit illumination (2 mm) on three distinct regions. B-D) Heart rate (upper panel) and PQ interval (lower panel) traces upon illumination (blue bar, 30 s, 0.7 mW/mm^2) of three distinct heart regions as shown in A. B) Illumination of the atria. C) Illumination of the AV-septal area. D) Illumination of the ventricles. E-G) ECG traces before and during illumination corresponding to the time points indicated in B-D by pink lines.

3.3 Generation of G_s-induced ventricular arrhythmias in Casq2 -/- hearts after pharmacological heart rate reduction

Despite the reportedly stronger phenotype, VTs could not be induced in Casq2 -/- JellyOp pos. Langendorff-perfused hearts by illumination of the ventricles (Fig. 13A-C). Therefore, it was tested whether activation of endogenous β-AR was able to induce arrhythmias. However, Iso perfusion did not induce VTs (Fig. 13D-F) but strongly increased heart rate by SA nodal stimulation.

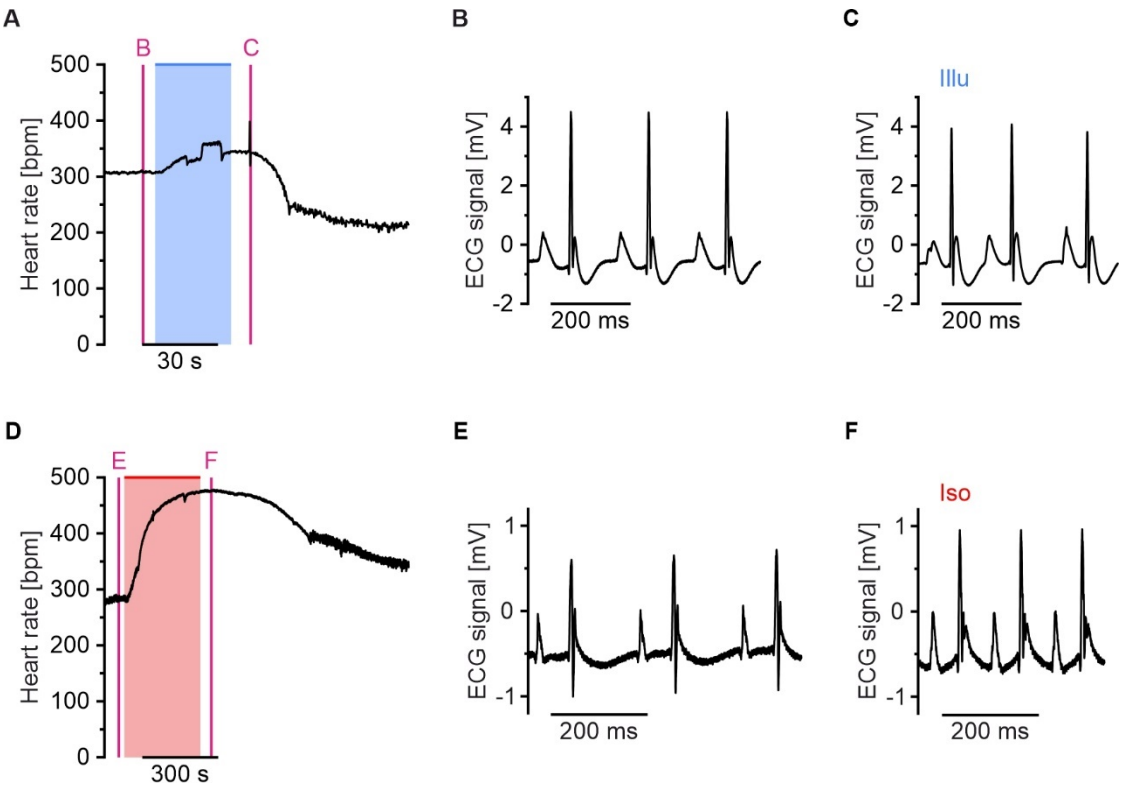

Figure 13: Effect of ventricular G_s-activation in JellyOp pos. Casq2 -/- hearts.
A) Heart rate response upon ventricular illumination (blue bar, 4 mW/mm^2, 30 s). B,C) ECG recordings before (B) and after (C) JellyOp activation at the time points indicated in A by pink lines. D) Heart rate response after Iso perfusion (red bar, 100 nM, 5 min). E,F) ECG recordings before (E) and after (F) Iso perfusion at the time points indicated in D by pink lines.

To test whether the high heart rate prevented VTs, hearts were perfused with the parasympathetic agonist Cch (1 µM) to activate M2 muscarinic receptors and lower the heart rate via G_i signaling in the SA node. This led to a heart rate reduction from an average of 328.0 ± 8.7 to 121.1 ± 11.5 bpm (Fig. 14A). However, still no VTs occurred after illumination (0 out of 3 mice) and only in 1 out of 7 mice after Iso application (Fig. 14B,D,E). For Iso application, constant perfusion as well as bolus injection through the aorta was tested (0.1–1 µM), which both did not induce VTs.

The buffer used for Langendorff-perfusion has been previously used in a number of optogenetic studies and is on the basis of a HEPES buffered tyrode solution. This is optimal to ensure long-lasting, stable heart rate in *ex vivo* whole heart experiments. However, in the induction of arrhythmias, the high buffering capacity of HEPES might be unphysiologically protective. Previous studies on the VT generation in the Casq2 -/- mice were performed in anesthetized mice *in vivo*[30,173]. Physiologically the most important buffer system in the blood is the bicarbonate buffer. To simulate *in vivo* conditions, the buffer for Langendorff-perfusion was subsequently switched to KH buffer, which functions based on bicarbonate buffering and pH equilibration with 5% CO_2. With the perfusion of KH buffer, VTs occurred more frequently after Iso perfusion in 5 out of 7 mice (Fig. 14C,F-H). PVCs as well as triggered VTs occurred, while reentry VTs could not be observed. Subsequent investigations of PVCs and triggered VTs were therefore performed in KH buffer.

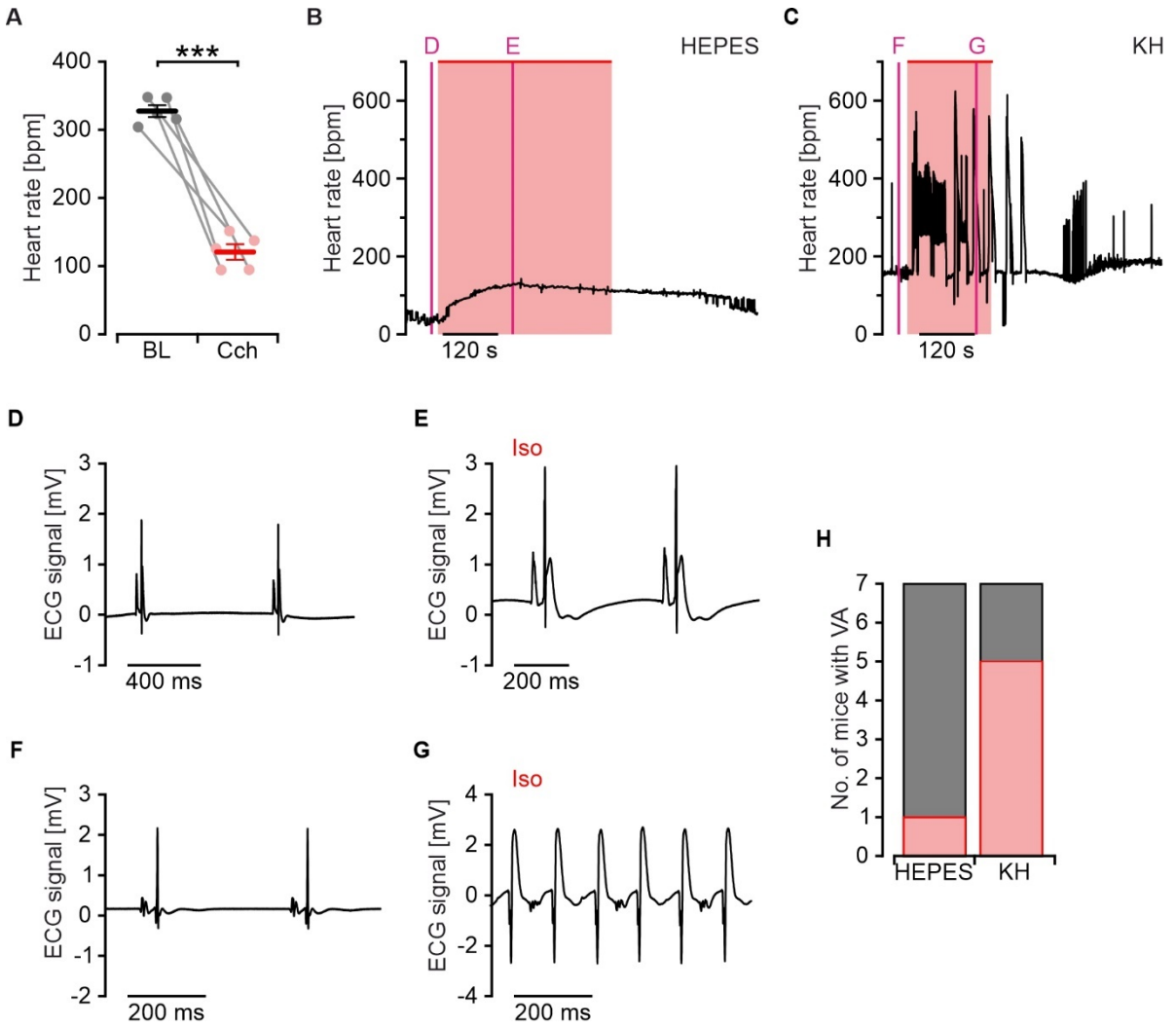

Figure 14: VT induction by β-AR activation in Casq2 -/- hearts after heart rate reduction.
A) Heart rate of Langendorff-perfused mouse hearts at baseline (black) and during Cch (1 µM, red) perfusion (N=5, paired student's t-test). B,C) Heart rate response upon perfusion with 100 nM Iso (red bar) during Cch-reduced heart rate in Casq2 -/- hearts perfused with HEPES buffer (B) or bicarbonate buffered KH buffer (C). Pink lines indicate time points depicted in D-G. D,E) ECG recordings before (D) and during (E) Iso prefusion in a heart perfused with HEPES buffer. F,G) ECG recordings before (F) and during (G) Iso perfusion in a heart perfused with KH buffer. H) Number of mice displaying at least one episode of VT upon Iso perfusion (red bars, N=7) during Langendorff-perfusion with either HEPES or KH buffer.

3.4 Induction of VT by optogenetic G_s-stimulation after pharmacological heart rate decrease

After establishing a buffer perfusion protocol to investigate G_s-induced VTs, the source region of these VTs could be investigated by local optogenetic activation. In order to selectively activate the endocardium, a 360° light-emitting catheter was developed by LifePhotonic GmbH (Bonn), consisting of a light fiber with a cylindrical tip (diameter: 500 µm, length of illumination zone: 4 mm) coated with

light scattering particles, which could be inserted into the ventricles (Fig. 15A). The light catheter was coupled to a 488 nm laser (Omicron-Laserage). An integrating sphere (Thorlabs) was used to accurately measure the intensity of the light dispersed by the catheter in all directions (Fig. 15B). To calculate the intensity of illumination per area, the endocardial ventricular area of the mouse heart was estimated from published echocardiographic data. For this, the endocardial lumen area of the short axis (A2=12.6 mm^2 [179]) of CD1 mouse hearts during diastole was taken to calculate the endocardial surface area ($SA_{Endo}=4*\pi*r^2$, with $r=\sqrt{A2}/\pi$) with the LV lumen approximated as a sphere (Fig. 15C). This led to an approximation of the endocardial surface area being ~15 mm^2.

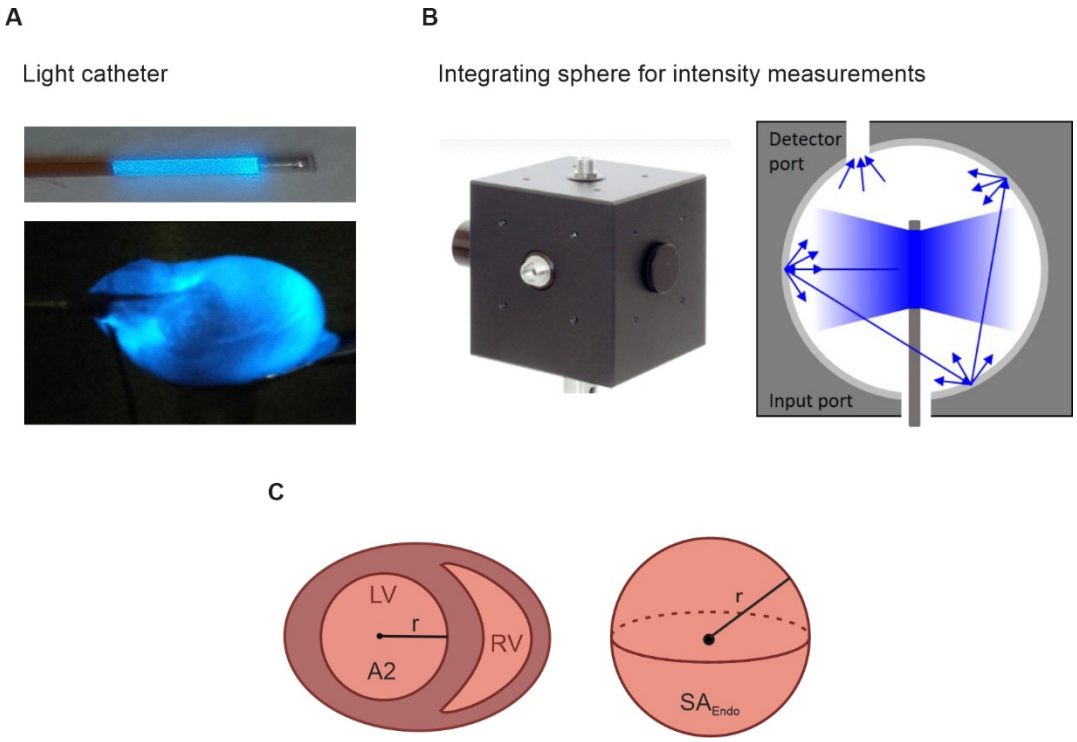

Figure 15: Endocardial illumination in Langendorff-perfused hearts using a light catheter.
A) A 360° light catheter coupled to a blue light (488 nm) laser (upper panel) was developed to be inserted into the ventricle of a Langendorff-perfused mouse heart and to illuminate the endocardium (lower panel: epicardial view after insertion into the LV). B) Integrating sphere (Thorlabs) used for accurate measurement of total light intensity emitted by the light catheter. C) Left: Schematic of the cross-section of the heart along the short axis to depict LV endocardial lumen area (A2) from which the radius (r) of the LV lumen was calculated. Right: spherical approximation of the LV lumen from which the endocardial surface area (SA_{Endo}) was calculated using r.

Endocardial illumination after Cch-induced decrease of heart rate induced individual PVCs, followed by triggered VT, which self-terminated shortly after termination of illumination (Fig. 16). PVCs or triggered VTs could be induced in 4 out of 4 Casq2 -/- JellyOp pos. hearts.

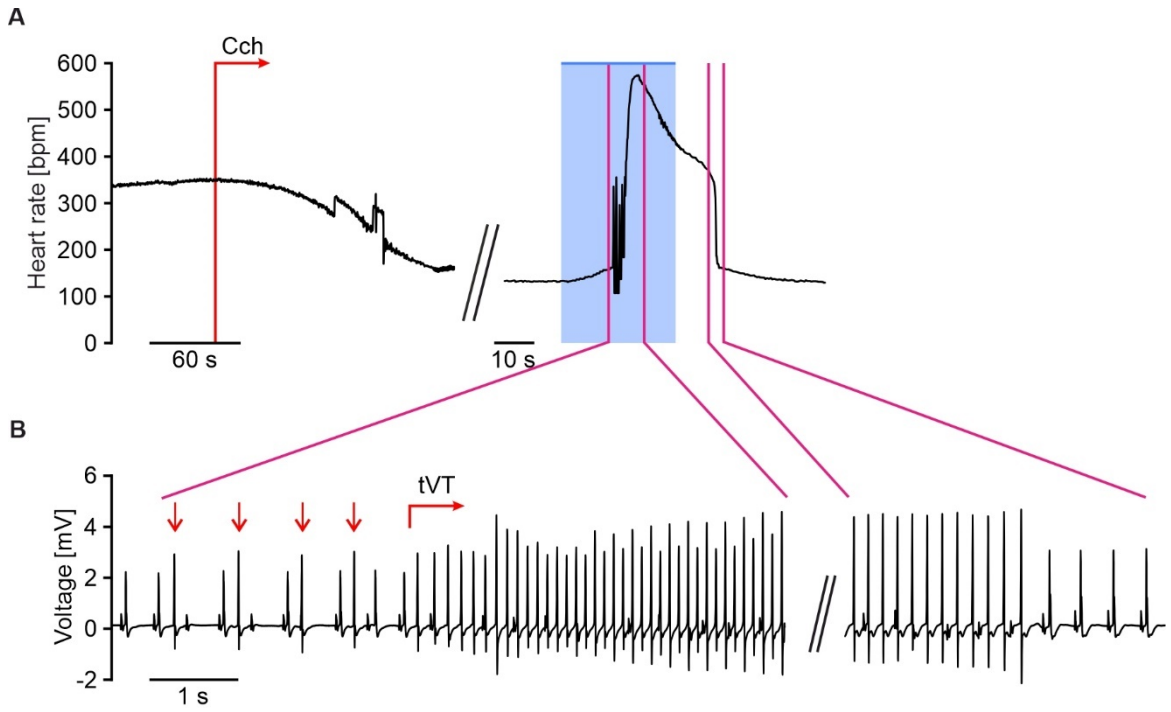

Figure 16: Optogenetic VT induction in Casq2 -/- JellyOp pos. mice.
A) Original frequency trace of a Langendorff-perfused heart of a Casq2 -/- JellyOp pos. mouse. Continuous perfusion with 1 µM Cch (indicated by red arrow) and subsequent endocardial illumination (30 s, 1 mW/mm^2, blue bar) leads to VT. B) ECG trace depicting individual PVCs (red arrows) and start as well as termination of triggered VT (tVT). Traces correspond to time windows in A (pink boxes).

3.5 Characterization of VT inducibility of the left and right ventricle

The light catheter was used for illumination of the LV and the right ventricle (RV) with similar light stimulation (total applied light stimulation 3–6.5 s*mW/mm^2). Upon illumination of Cch-perfused (1µM) hearts, PVCs and triggered VTs were observed. Triggered VTs consisted of fast-paced individual extrabeats. Therefore, each QRS complex in a triggered VT was counted as an individual PVC for the quantification of PVCs. Both LV and RV illumination lead to a significant increase of PVC count in the Casq2 -/- JellyOp pos. mice (Fig. 17A). The PVC count between the LV and the RV was not significantly different.

The triggered VTs occurring in Casq2 -/- JellyOp pos. mice were further characterized by the delay from illumination start to the start of the triggered VT and the duration of the triggered VT. Time to start of VT was significantly shorter by illumination of the LV than the RV (Fig. 17B). There was no significant difference in VT duration between the illumination of the LV and RV (Fig. 17C).

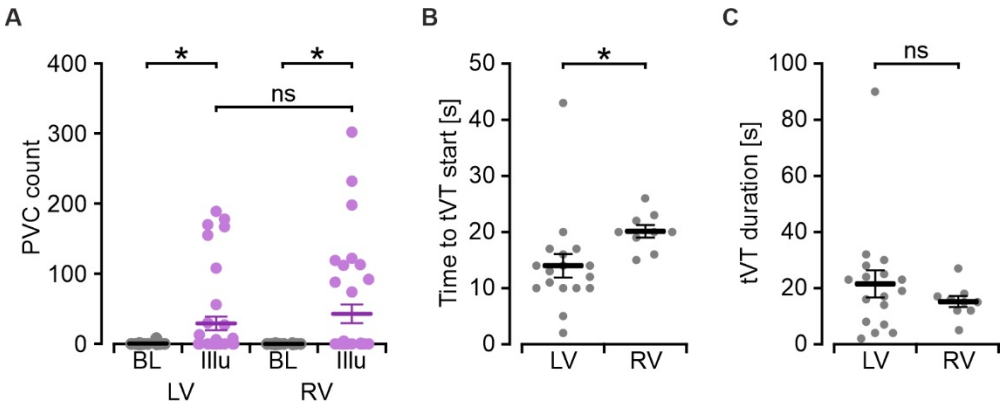

Figure 17: VT generation in Casq2 -/- mice by endocardial illumination of the LV and RV.
A) PVC count in Casq2 -/- JellyOp pos. mice after endocardial catheter illumination of the LV or RV (illu: 3–6.5 s*mW/mm^2, BL: 30 s interval before illu; during continuous perfusion with 1 µM Cch); Brown-Forsythe and Welch ANOVA with Dunnett's T3 post-test (N=4; n=34-38). B,C) Time to start of triggered VT (tVT) (B) and duration of tVT (C) after illumination of the RV or LV in Casq2 -/- JellyOp pos. hearts (unpaired Welch's corrected t-test; N=4; n=9-17).

3.6 Influence of heart rate on VT induction

The G_s-induced PVC and VT occurrence after pharmacological heart rate reduction by Cch indicated that higher heart rate might act protective towards VT generation. The role of heart rate on the inducibility of VTs was further investigated by pacing the ventricles electrically at a high and a low beating rate. For this, the atria were removed prior to pacing to abolish the sinus rhythm and thus reduce intrinsic beating frequency. Then, the ventricles were paced at 400 bpm and 200 bpm and endocardial illumination in the LV was applied to induce VTs. Interestingly, PVCs did not occur at high beating frequency (Fig. 18A,B). In contrast, PVCs occurred frequently at low beating frequency after endocardial illumination (Fig. 18C-E). Thus, a low heart rate presents a risk factor for VTs, while a faster heart rate seems protective against VTs.

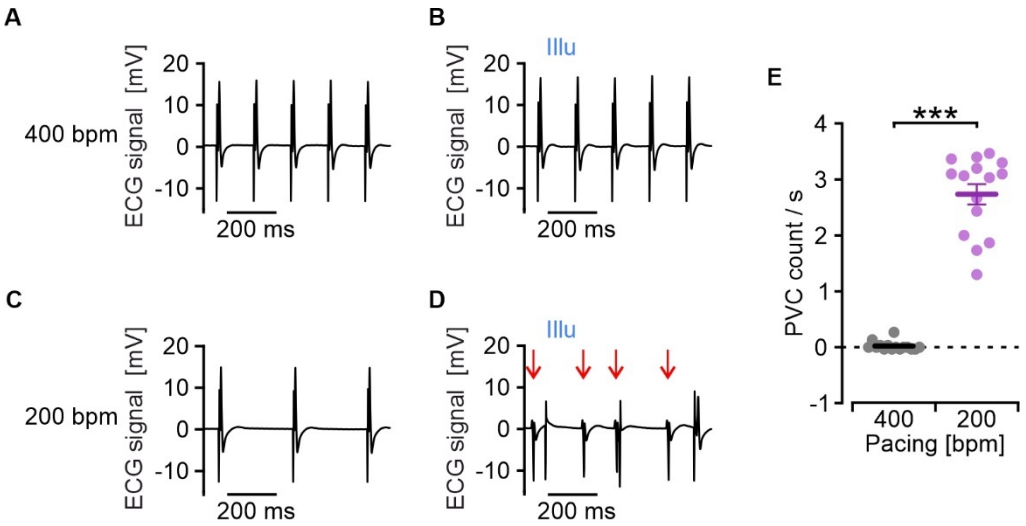

Figure 18: Influence of heart rate on PVC induction.
A-D) Representative ECG traces of a Langendorff-perfused heart during ventricular pacing at high (400 bpm) and low (200 bpm) before (A,C) and after (B,D) endocardial illumination (1 s, 500 µW/mm^2). Note the occurrence of PVCs (red arrows) in D. E) Number of PVCs per second occurring after endocardial illumination during low and high frequency pacing (N=5, n=15, unpaired Welch's corrected t-test).

3.7 Comparison of VT inducibility by endocardial and epicardial G_s-stimulation

After showing that endocardial G_s-activation induced PVCs at low beating frequencies, the next step was to compare the sensitivity towards PVC generation in the endocardium with the sensitivity in the epicardium. Because there was no difference between RV and LV illumination in PVC generation (Fig. 17), the LV was used for these experiments because the LV has a greater wall thickness than the RV. At an LV wall thickness of 0.7–1 mm, approx. 10% of blue light is expected to penetrate the tissue. The wall thickness can reduce activation overlap from light penetration through the tissue and thereby minimize JellyOp activation in the endocardium by illumination of the epicardium and vice versa. In order to generate comparable results by endocardial and epicardial illumination, identical illumination parameters had to be developed. As described in Chapter 3.4, the endocardial surface area had been estimated to be 15 mm^2. In order to match the epicardial illumination to the endocardial illumination, a circular light beam was focused onto the epicardium via the fluorescence macroscope with the same size and intensity as the endocardial illumination (Fig. 19).

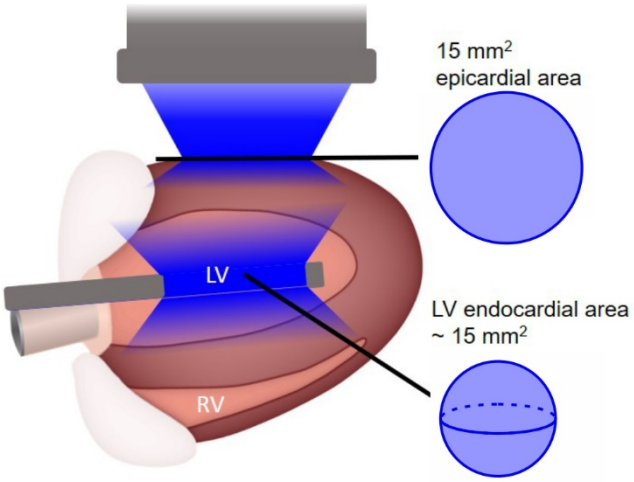

Figure 19: **Light-intensity matched endocardial and epicardial illumination.**
Schematic for comparison of endocardial illumination using the light catheter and epicardial illumination using a fluorescence macroscope. Epicardial illumination area was matched to an estimated spherical left ventricular endocardial area as described in Chapter 3.4.

After atria removal, hearts were electrically paced at 200 bpm and alternately illuminated epicardially and endocardially. Fig. 20A-E shows corrected ECG signals in which electrically paced beats were removed offline to only depict PVCs. Endocardial illumination in Casq2 -/- JellyOp pos. hearts (Fig. 20A) induced a high number of PVCs with a definitive starting point, duration and end point. Epicardial illumination (Fig. 20B) in the same heart induced a much lower number of PVCs, even when the light intensity was increased ten-fold on the epicardium (Fig. 20C). Statistically, endocardial illumination produced significantly more PVCs than epicardial illumination with identical intensity (Fig. 20F, purple dots). To nevertheless exclude a possible discrepancy in the light application method, the epicardial illumination was also performed with ten-fold increased intensity, which still generated significantly less PVCs than endocardial illumination (Fig. 20F, Epi 10x int).

Endocardial illumination in hearts from Casq2 +/+ JellyOp pos. mice only generated PVCs in some hearts with significantly lower PVC count/s after endocardial illumination (Fig. 20D,F, blue dots), showing that the generated PVCs are enhanced by the CPVT phenotype. Endocardial illumination of Casq2 -/- JellyOp neg. mice did not affect PVC generation (Fig. 20E,F, grey dots), excluding unspecific light effects, such as heat development.

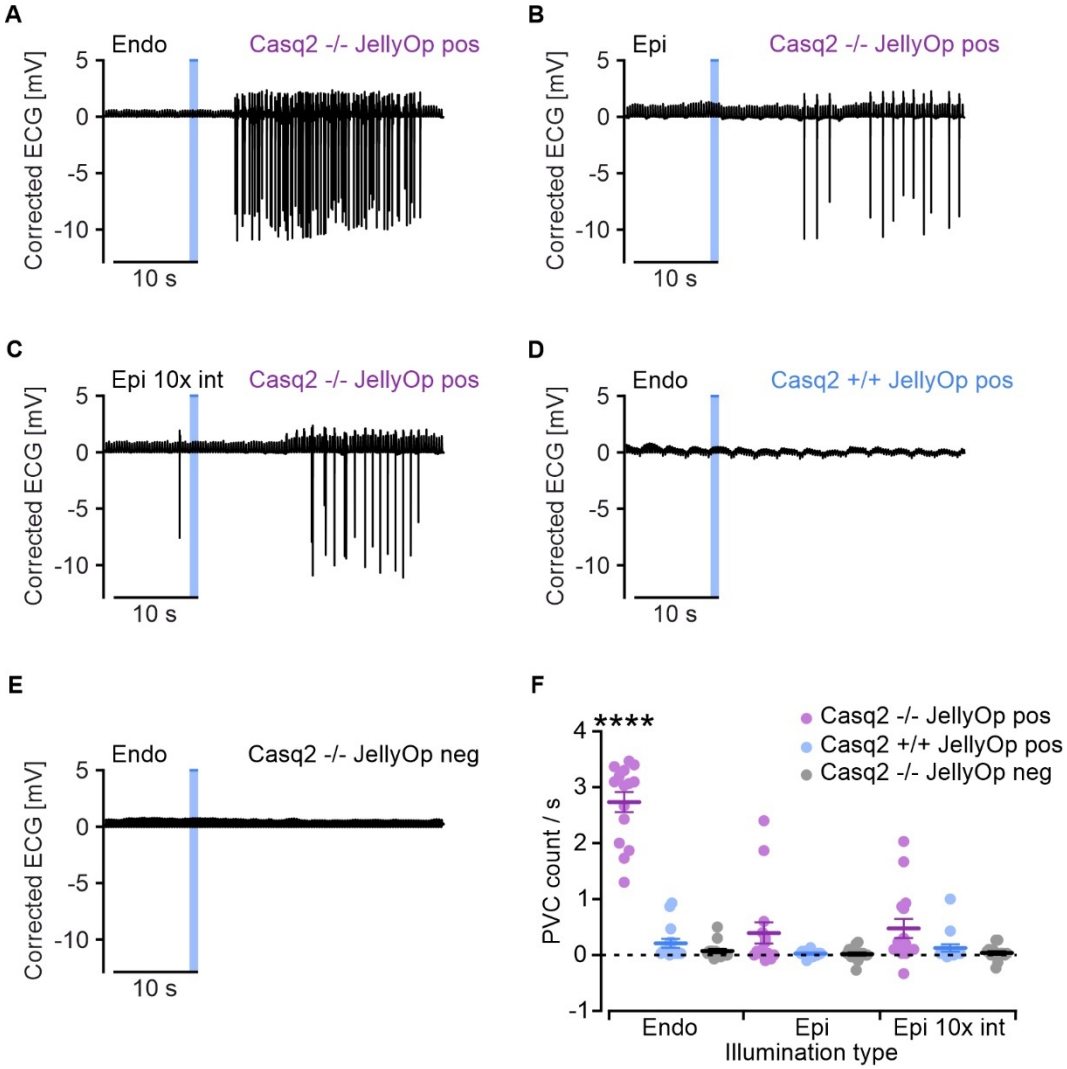

Figure 20: Induction of VT by endo- and epicardial illumination.
A-C) Representative corrected ECG traces (pacing signals removed to only depict PVCs) of endocardial (Endo, A) and epicardial (Epi, B) illumination with identical intensities (blue bar, 1 s, 500 µW/mm^2) and epicardial illumination with 10-fold higher intensity illumination (Epi 10x int, blue bar, 5 mW/mm^2) in a Casq2 -/- JellyOp pos. heart. D) Representative corrected ECG trace of endocardial illumination (blue bar, 1 s, 500 µW/mm^2) in a Casq2 +/+ JellyOp pos. heart. E) Representative corrected ECG trace of endocardial illumination (blue bar, 1 s, 500 µW/mm^2) in a Casq2 -/- JellyOp neg. heart. F) Number of PVCs per second occurring after illumination of either the endocardium (Endo) or the epicardium (Epi) with identical intensities (1 s, 500 µW/mm^2) or the epicardium with 10x higher intensity (Epi 10x int, 5 mW/mm^2) in Casq2 -/- JellyOp pos. (purple), Casq2 +/+ JellyOp pos. (blue) and Casq2 -/- JellyOp neg. (grey) hearts (N=5, n=15, Brown-Forsythe and Welch ANOVA with Dunnett's T3 post-test - ****: group Endo Casq2 -/- JellyOp pos. to all other groups.).

To further analyze the temporal kinetics of the occurring PVC bursts with clearly identifiable start and end points in the Casq2 -/- JellyOp pos. mice, time from illumination to start of PVC burst, PVC burst duration and PVC burst period were calculated. PVC burst period is the average interval between 2 ventricular beats (including paced beats) during the PVC burst. Time to PVC burst start was significantly shorter after endocardial than epicardial illumination (Fig. 21A). PVC burst duration was significantly

longer after endocardial illumination (Fig. 21B) and the period of the intervals between PVCs was significantly shorter after endocardial illumination (Fig. 21C).

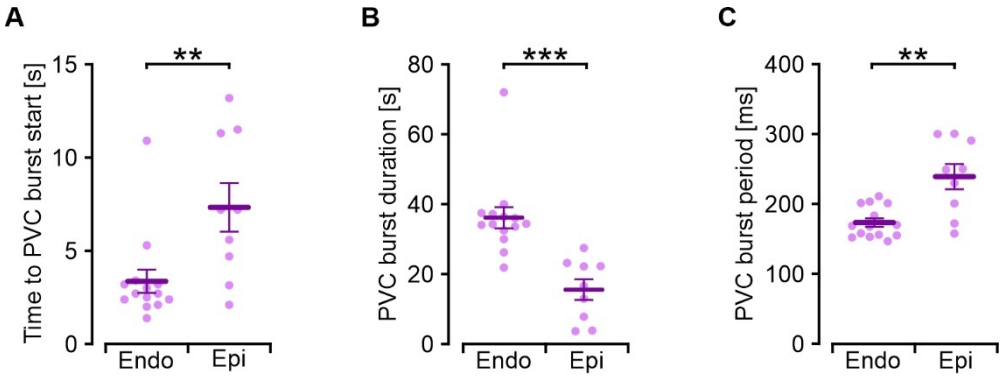

Figure 21: Qualitative analysis of PVC bursts induced by endo- and epicardial illumination in Casq2 -/- JellyOp pos. hearts.
The PVC bursts occurring in Casq2 -/- JellyOp pos. hearts during slow electrical pacing after illumination of the endocardium (N=5; n=14) or the epicardium (N=5; n=9, including 10x Int) as depicted in Fig. 20A-C were analyzed regarding time to start of PVC burst (A) duration of PVC burst (B) and PVC burst period (C). A+B: unpaired student's t-test; C: unpaired Welch's corrected t-test.

3.8 Effect of endocardial ablation on PVC incidence

The increased PVC incidence after endocardial illumination compared to the PVC incidence after epicardial illumination indicates that subendocardial cardiomyocytes might be the origin of PVCs and VTs. To confirm that the origin of the PVCs observed upon endocardial illumination was located in the first subendocardial cell layers within the LV, which among endocardial cardiomyocytes also contain Purkinje cells, these cell layers were chemically ablated by Lugol solution, an iodine solution containing 5% I_2 and 10% KI. Exposure to Lugol solution leads to cardiomyocyte death, whereby conduction system cells are especially sensitive to Lugol solution, but bolus injection into the ventricle also ablates the innermost subendocardial cardiomyocytes[175,181–183]. Ablation of the subendocardial cardiomyocyte layer was confirmed after the experimental procedure by fixation and staining for α-actinin. After Lugol ablation, α-actinin signal, and thus functional cardiomyocytes, was lost in the subendocardial cell layer of the LV (Fig. 22A). The endocardium of the non-ablated RV is shown as a control for intact endocardium with α-actinin positive cardiomyocytes. Hearts were endocardially illuminated before and after bolus injection of Lugol solution. Before Lugol ablation, PVCs occurred frequently after illumination. After Lugol ablation of the LV endocardium, PVC count after endocardial illumination was significantly reduced compared to before ablation and in 2 hearts, even completely abolished (Fig. 22B-F).

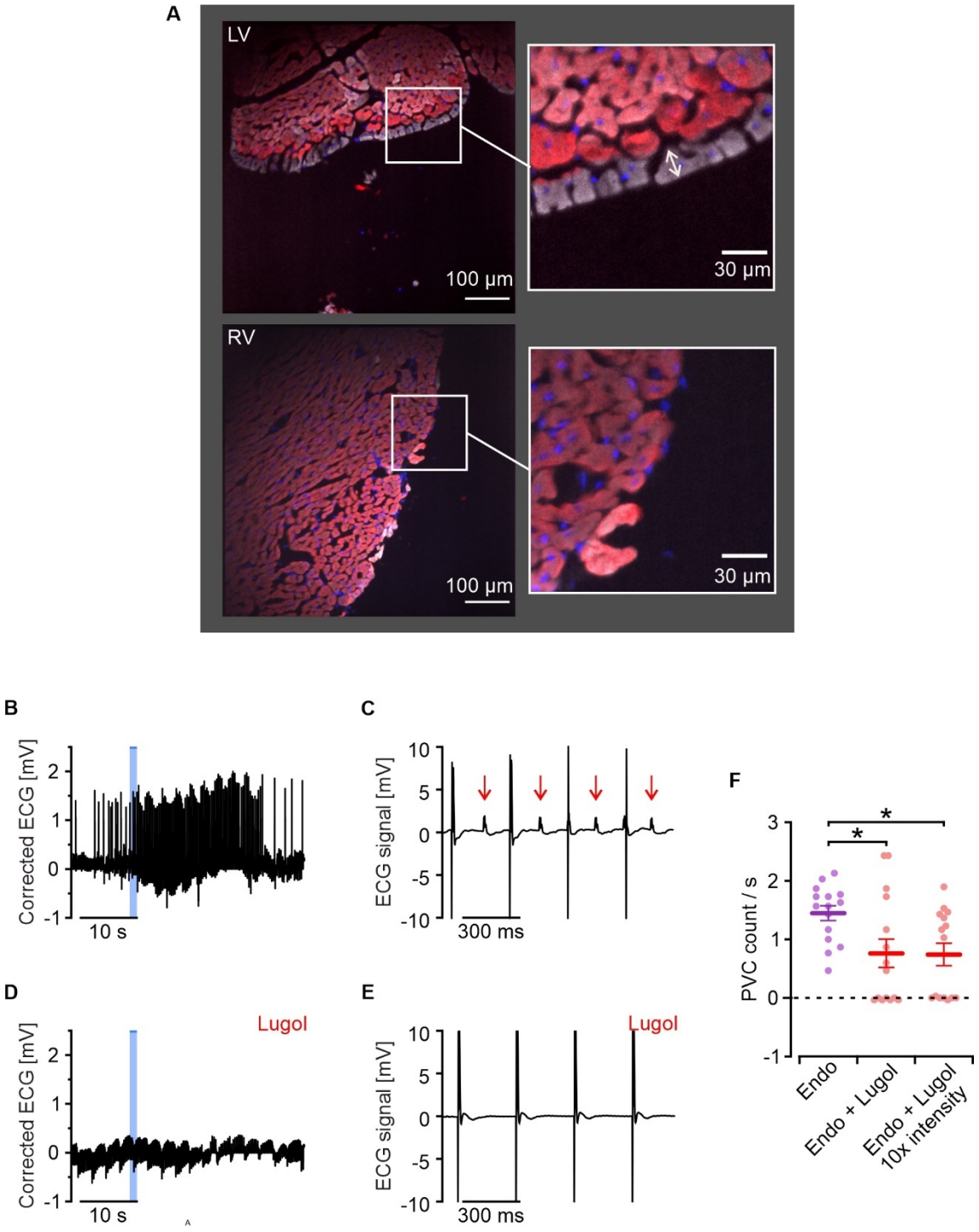

Figure 22: PVC induction after endocardial ablation.
A) Immunostaining of the LV (upper image) and RV (lower image) after endocardial ablation of the LV using Lugol solution; α-actinin (red), Cy3 autofluorescence (white) and DAPI (blue); left scale bar = 100 µm, right scale bar = 30 µm. White arrow (insert, right) indicates ablation of the first subendocardial cardiomyocyte layer identified by lack of α-actinin signal. B-E) Example traces of corrected ECG and original ECG traces before (B,C) and after (D,E) Lugol ablation (illumination: blue bar, C+E at 10 s after illu); PVCs marked by red arrows. F) PVC count per second after endocardial illumination (500 µW/mm^2 or 5 mW/mm^2 (10x intensity) before (purple) and after (red) endocardial ablation in Casq2 -/- JellyOp pos. hearts (N=5, n=15; Ordinary one-way ANOVA with Tukey's post-test).

3.9 Investigation of transmural JellyOp expression levels

Multiple factors could influence the increased sensitivity of the endocardium to produce JellyOp activation-induced arrhythmias, such as receptor expression levels, excitability of the cardiomyocytes or differences in downstream signaling and effector proteins of the G_s-signaling cascade. To investigate the origin of this increased susceptibility to generate PVCs, first immunofluorescence staining of a cross-section over the left ventricular wall of a JellyOp pos. heart was analyzed to ensure that JellyOp expression was not significantly higher in the endocardial cardiomyocytes (Fig. 23A,B). Intensity analysis of the native GFP signal (relative to α-actinin) showed a small but significant difference in JellyOp expression in the endocardium (defined as the first 300 µm of myocardial tissue from the LV lumen) compared to the mid-myocardium (defined as the myocardial tissue 300-600 µm from the LV lumen) and the epicardium (defined as myocardium more than 600 µm from the lumen) (Fig. 23C). There was no significant difference between mid-myocardial and epicardial tissue. The relative GFP signal measured in the endocardium (1.111 ± 0.006), however, was on average 4.0% and 5.7% lower than in the mid-myocardium (1.158 ± 0.0011) and the epicardium (1.178 ± 0.007), respectively. Therefore, the increased VT incidence by endocardial illumination cannot be explained by an increased JellyOp receptor expression. This indicates an endogenous difference in the endocardial compared to the epicardial cardiomyocytes as the cause for the increased arrhythmogenicity.

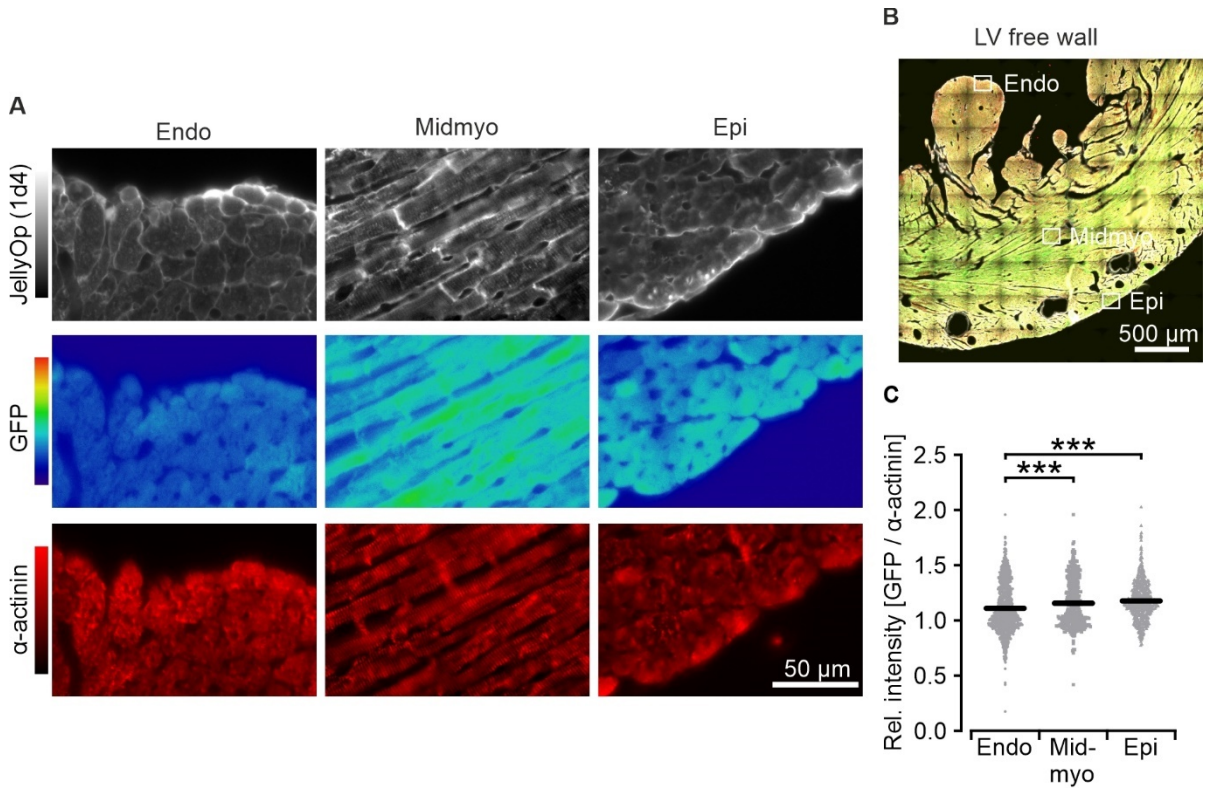

Figure 23: Transmural JellyOp expression.
A) JellyOp staining (1d4, upper panel, white), native GFP signal (middle panel, heat gradient) and α-actinin staining (lower panel, red) of a JellyOp pos. mouse heart. Depicted are excerpts of the endocardium (left panel, Endo), mid-myocardium (Midmyo, middle panel) and the epicardium (Epi, right panel). Scale bar = 50 µm. B) overview of the left ventricular free wall (merged image of α-actinin in red, GFP in green, 1d4 in white; scale bar = 500 µm). White boxes indicate the images depicted in A. C) Relative GFP intensity normalized to α-actinin in the three myocardial layers. Endocardium was defined as up to 299 µm from the lumen border, mid-myocardium 300-599 µm and epicardium ≥600 µm (Ordinary one-way ANOVA with Tukey's post-test).

3.10 Comparison of excitability of the endocardium and the epicardium

Another aspect that could be the underlying cause for the increased PVC generation in the endocardial cardiomyocytes is excitability, the propensity for a certain depolarization of the cardiomyocyte to cause an action potential. ChR2-expressing mouse hearts were used for the comparison of the excitability in the two areas, because Chr2 is a blue light-sensitive cation channel, which depolarizes the cells upon activation. Hereby, the depolarization of the cell is proportional to the applied light intensity. Short light pulses can thus be used to pace the heart. The lowest light intensity at which the heart can be paced is defined as the pacing threshold and used here as a read-out for the excitability of the cardiomyocytes upon depolarization. Langendorff-perfused ChR2-expressing mouse hearts were paced at 400 bpm by 10 ms long light pulses either using the light catheter in the LV (Fig. 24A) or macroscopic illumination (Fig. 24B) with identical configurations as for the JellyOp pos. hearts (Chapter

3.7) to determine pacing thresholds for endocardial and epicardial illumination. Interestingly, pacing thresholds in the endocardium were lower than in the epicardium (Endo: 36.9 ± 3.6 µW/mm^2; Epi: 71.1 ± 8.6 µW/mm^2), but only by a factor of two, which does not explain the more than ten-fold increased VT sensitivity of the endocardium (Fig. 24C). Thus, excitability – as well as differences in light application – were ruled out as causes for the increased VT occurrence in the endocardium.

Furthermore, pacing thresholds were determined during perfusion with the two previously used buffers – HEPES and KH buffer – to investigate whether the increased arrhythmic susceptibility in KH buffer (Chapter 3.3) could be explained by increased excitability, but no significant difference in pacing threshold between the two buffers was found (Fig. 24C).

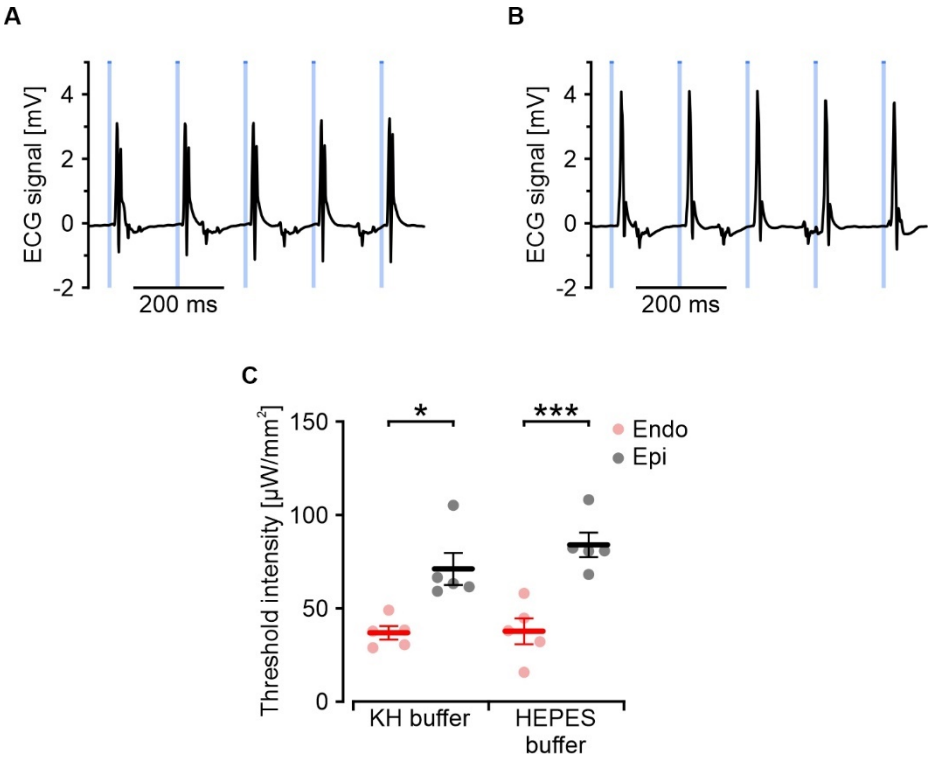

Figure 24: Endo- and epicardial ventricular pacing in ChR2 pos. hearts.
A) ECG trace of ventricular pacing of a ChR2 pos. mouse heart by endocardial illumination (blue bars, 39,5 µW/mm^2, 10 ms, 400 bpm). B) ECG trace of ventricular pacing of a ChR2 pos. mouse heart by epicardial illumination (blue bars, 68 µW/mm^2, 10 ms, 400 bpm). C) Pacing thresholds for endocardial and epicardial illumination in ChR2 pos. mouse hearts perfused with KH buffer or HEPES buffer (N=5; ordinary one-way ANOVA with Tukey's post-test).

3.11 Effect of PDE inhibition on PVC generation

It was shown in the previous chapters (3.9, 3.10) that the cause for the increased sensitivity of the endocardium to generate PVCs after illumination was neither found on the receptor level nor due to differences in illumination configuration or cell excitability. Thus, it can be expected that the difference lies downstream of the receptor in the G_s-signaling cascade. It is well established in the literature that PDEs regulate G_s-response in cardiomyocytes through the degradation of cAMP, which limits diffusion and thereby creates cAMP microdomains. Changes in PDE expression – e.g. in heart failure – severely alter G_s-effects, which can be pro-arrhythmogenic[92,103].

However, no previous literature was found on differences in endocardial and epicardial cardiomyocytes regarding PDE expression or phosphorylation of effector proteins. Thus, the influence of PDEs on endo- and epicardially-induced PVCs was investigated by applying IBMX – an unspecific PDE inhibitor. For this, light dose-response curves were generated: Hearts were illuminated endo- and epicardially with an illumination protocol of light pulses (1 s light duration, 30 s interval between pulses) with increasing light intensities. Fig. 25A,B depict PVCs occurring during the illumination protocol for endocardial (A) and epicardial (B) illumination without IBMX and during perfusion with 1 µM and 3 µM IBMX. Note the ten-fold higher maximal intensity used for epicardial illumination (11.9 mW/mm^2) compared to endocardial illumination (1.09 mW/mm^2). Light dose-response curves were generated for averaged PVC count per second (Fig. 25C,D). IBMX dose-dependently increased baseline occurrence of PVCs and total PVC count per second after endocardial as well as epicardial illumination (Fig. 25C,D, orange and red traces). To account for the increased occurrence of PVCs at baseline, the dose-response curves were corrected by subtraction of baseline PVC count (Fig. 25E). The corrected dose-response curves were fitted with a Hill1 equation to calculate the light intensity needed for half-maximal effect (Eli50). A slight shift in corrected light dose-response was apparent in the epicardial illumination, with the Eli50 shifting from 5.0 mW/mm^2 at 0 µM IBMX to 2.0 mW/mm^2 at 3 µM IBMX. However, IBMX did not shift Eli50 to endocardial levels, which displayed an Eli50 at 0 µM IBMX of 0.2 mW/mm^2. Endocardially, a slight shift also occurred after IBMX application to 0.12 mW/mm^2 at 3 µM. If PDE inhibition affected the sensitivity towards PVC generation, it would be expected that the strongest increase in corrected PVC count would occur at the ELi50. Therefore, corrected PVC counts at Eli50 of 0µM IBMX were compared. The corrected PVC count at ELi50 of 0 µM IBMX was not significantly changed by IBMX neither in the endocardial nor the epicardial illumination (Fig. 25F,G).

These results show that inhibition of PDE increased PVC occurrence, validating that increased cAMP levels caused the observed arrhythmias. PDE inhibition, however, does not abolish the endo-epicardial difference, indicating that presumable differences in PDE expression or activity are not the leading cause of increased arrhythmogenicity of the endocardium.

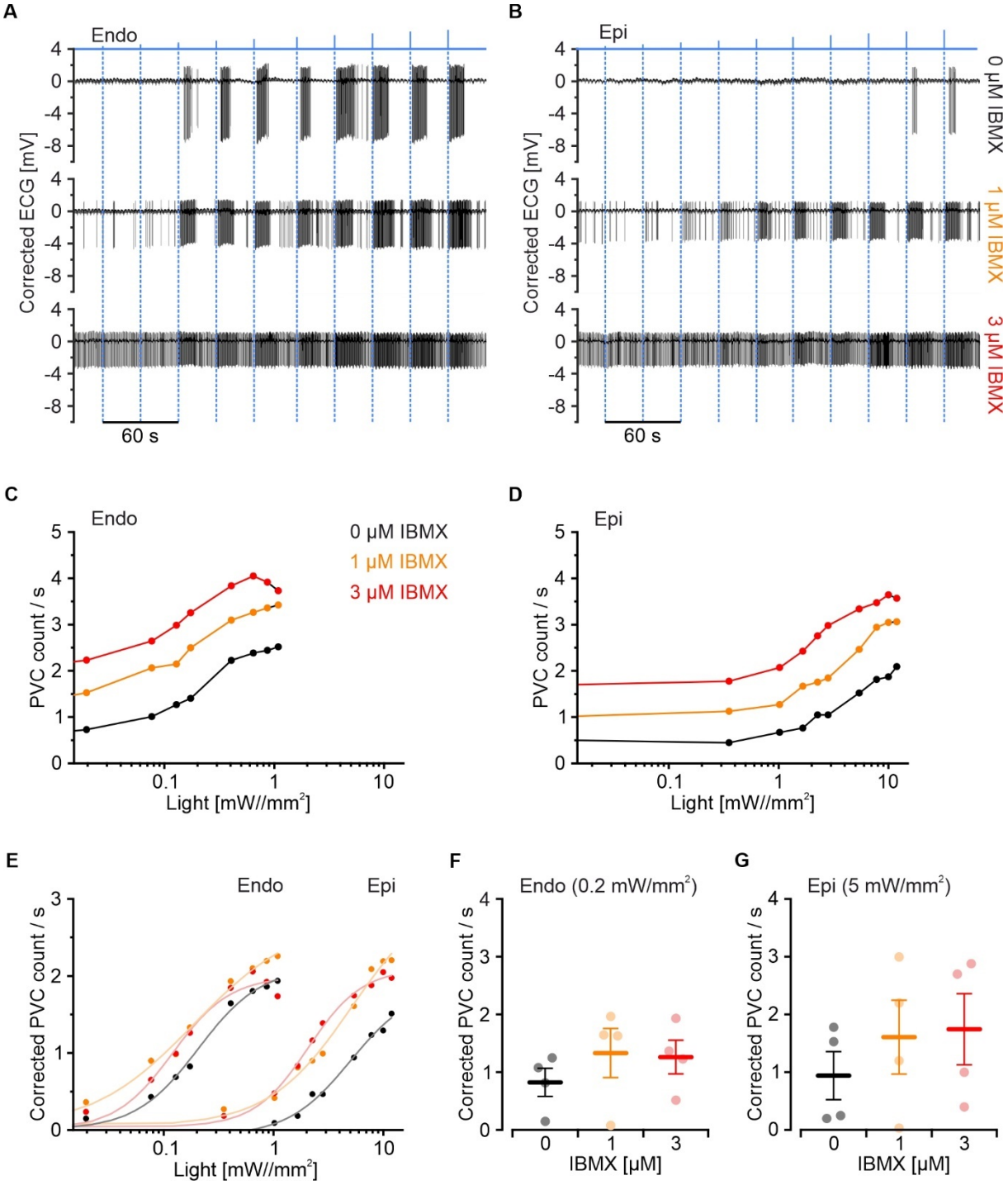

Figure 25: Light-induced PVCs during PDE inhibition.
A,B) Exemplary traces of corrected ECG only depicting PVCs of a heart perfused with 0 µM (upper panel), 1 µM (middle panel) or 3 µM (lower panel) IBMX upon endocardial (A) or epicardial (B) illumination with increasing light intensities (endocardial: 0.0035–1.09 mW/mm^2; epicardial: 0.35–11.9 mW/mm^2; 1 s). C-D) Dose response curves of averaged PVC count per second after endocardial (C) and epicardial (D) illumination as depicted in A+B (N=4). E) Dose response curves of corrected, averaged PVC count (baseline PVC count subtracted). Lines: Hill1 fit (Origin). F,G) corrected PVC counts at illumination closest to ELi50 of 0 µM IBMX for endocardial (F, $ELi50_{0\ \mu M,\ endo}$ = 0.2 mW/mm^2) and epicardial (G, $ELi50_{0\ \mu M,\ epi}$ = 5 mW/mm^2) illumination (N=4; Ordinary one-way ANOVA with Tukey's post-test).

3.12 Differential expression and phosphorylation status of SR calcium handling proteins in the endocardium and the mid-myocardium

Since differences in PDE activity seemed not to be the cause for the increased sensitivity in the endocardium, the next step was to investigate down-stream targets of the G_s-signaling cascade. PVCs observed in CPVT are known to be caused by calcium leak from the SR. Therefore, western blot analysis was used to investigate if effector proteins of the SR calcium handling machinery were differentially expressed. Therefore, tissue sample collection of subendocardial and mid-myocardial tissue was established by dissecting and freezing the LV free wall flat, endocardial side up on embedding medium (Fig. 10). Then, 300 µm of tissue from the endocardial side was cut and collected as the subendocardial sample. After discarding the next 500 µm of tissue, 300 µm mid-myocardial tissue was collected. Western blots for RyR2 (Fig. 26A,B), Serca2a (Fig. 26C,D) and PLN (Fig. 26E,F) showed no significant difference in expression between subendocardial and mid-myocardial tissue.

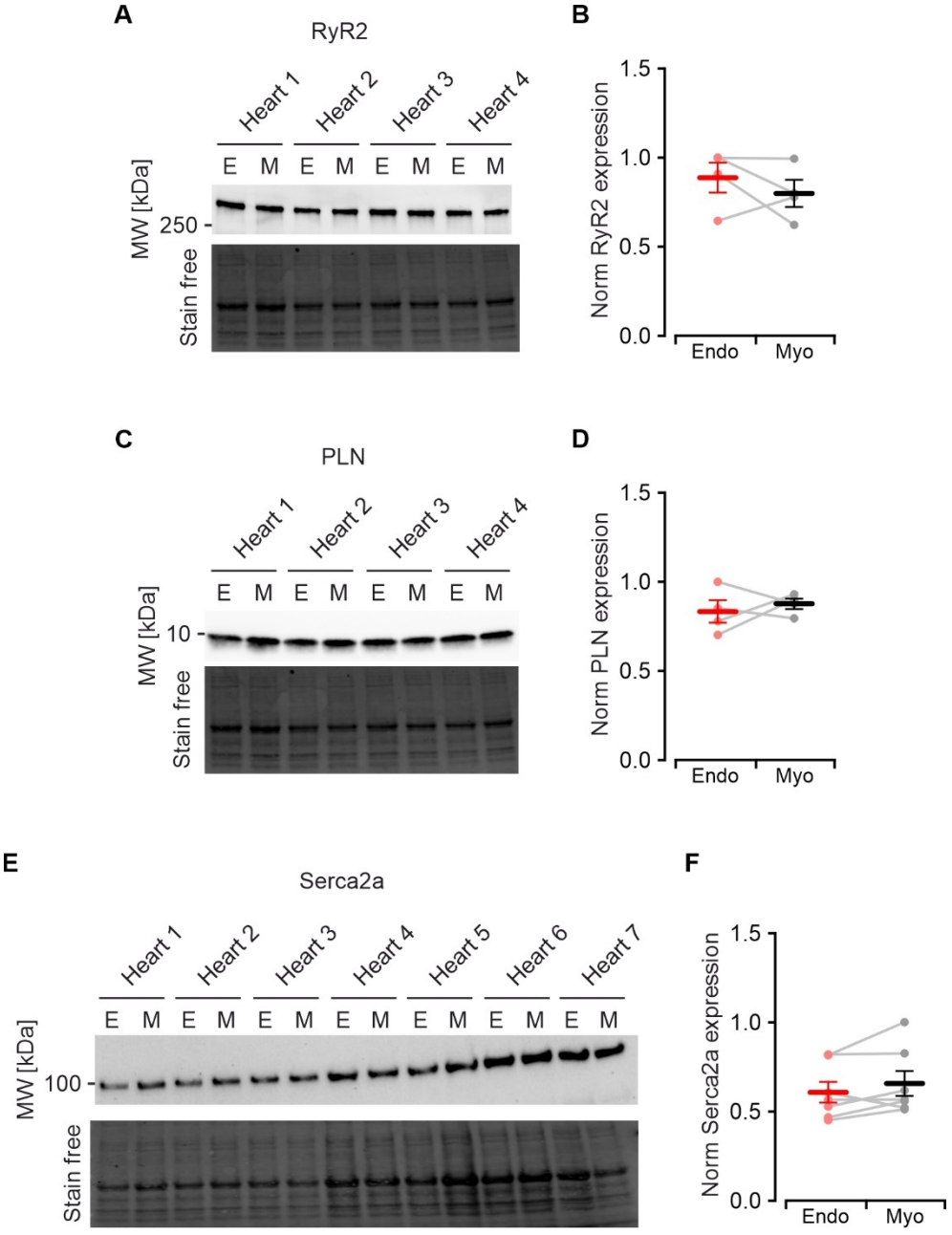

Figure 26: Local expression of calcium handling proteins.
A) Western Blot of RyR2 (565 kDa) and membrane staining of Bio-Rad stain free total protein (stain free). (E: subendocardial tissue; M: mid-myocardial tissue) B) RyR2 expression normalized to stain free and rel. to strongest band. (N=4) C) Western Blot of PLN (6 kDa) and membrane staining of Bio-Rad stain free total protein (stain free). D) PLN expression normalized to stain free and rel. to strongest band. (N=4) E) Western Blot of Serca2a (100 kDa) and membrane staining of Bio-Rad stain free total protein (stain free). F) Serca2a expression normalized to stain free protein quantification and relative to strongest band (N=7). Paired student's t-tests for B, D, F.

Since there was no difference in expression levels of SR calcium handling proteins, further investigation into the phosphorylation status in the heart regions was performed. For this, an antibody for PKA phosphorylated proteins at the PKA-specific recognition sequence RRXS*/T* was used for western blots. Western blot of tissue from Langendorff-perfused hearts at basal conditions revealed 5 distinct bands of phosphorylated proteins (Fig. 27A): band 1 - 147.7 kDa; band 2 - 120.6 kDa; band 3 - 67.5 kDa; band 4 - 26.1 kDa; band 5 - 10 kDa. Tissue samples from hearts stimulated by perfusion with Iso (1 µM, 5 min) had increased signal intensities compared to tissue samples from hearts at basal phosphorylation (Fig. 27B). Normalized intensities of each band (Fig. 27C-L) revealed significantly lower phosphorylation of bands 1 and 5 in the subendocardium at baseline. Band 5 also had lower phosphorylation in the subendocardium in Iso stimulated hearts. Furthermore, subendocardial and mid-myocardial tissue had differential phosphorylation in 3 out of 4 mice in band 2 at 120.6 kDa: while the subendocardial tissue showed a clear increase in phosphorylation after Iso stimulation, there was almost no increase in phosphorylation in the mid-myocardial stimulated tissue. The other bands (3+4) were not differentially phosphorylated.

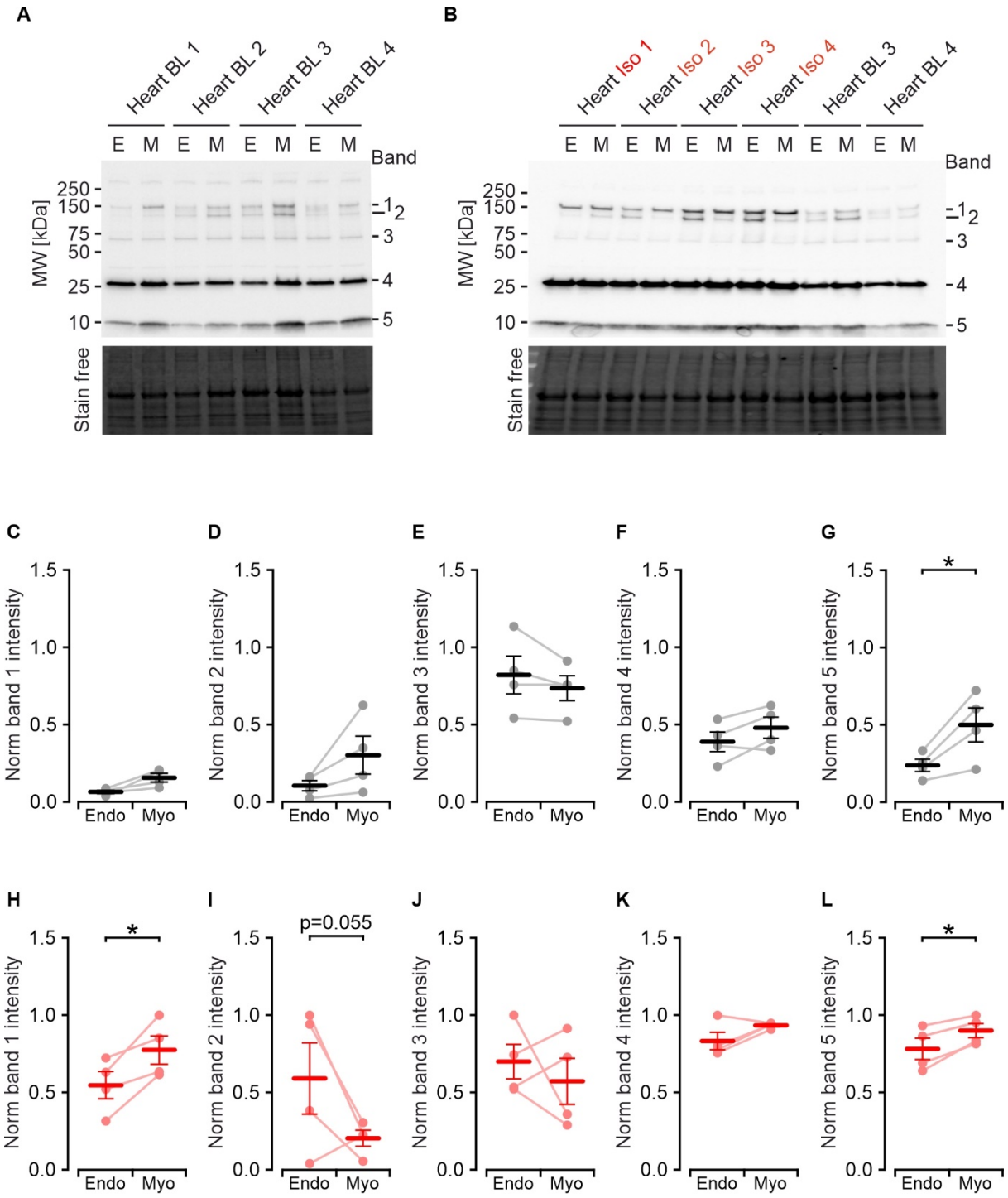

Figure 27: Local PKA phosphorylation status.
A+B) Western blot of RRXS*/T* phosphorylated proteins and corresponding membrane staining of Bio-Rad stain free total protein (stain free). Tissue collected from basal (BL, A + last 4 lanes in B for normalization of the 2 blots) or stimulated (iso in B, 1 µM, 5 min) Langendorff-perfused hearts (E: subendocardial tissue; M: midmyocardial tissue). C-G) Intensities of bands 1-5 in BL hearts as indicated in A normalized to stain free and rel. to strongest band in Iso hearts (N=4; paired student's t-test). H-L) Intensities of bands 1-5 in Iso stimulated hearts as indicated in B, normalized to stain free and relative to strongest band in Iso stimulated hearts (N=4; paired student's t-test).

To further analyze the transmurally differential phosphorylation status, endocardial to mid-myocardial ratios (endo/myo) for each heart were generated (Fig. 28). An increase of the endo/myo ratio after Iso stimulation compared to baseline would indicate a higher relative phosphorylation increase by Iso stimulation in the endocardium than the mid-myocardium. There was a significantly higher endo/myo ratio in band 5 (Fig. 28E). Bands 1 and 2 also showed a slightly increased endo/myo ratio (Fig. 28A,B). Especially, Band 2 might be a protein of interest because 3 out of 4 mice showed a clear increase of endo/myo ratio after Iso stimulation. However, these differences were not statistically significant.

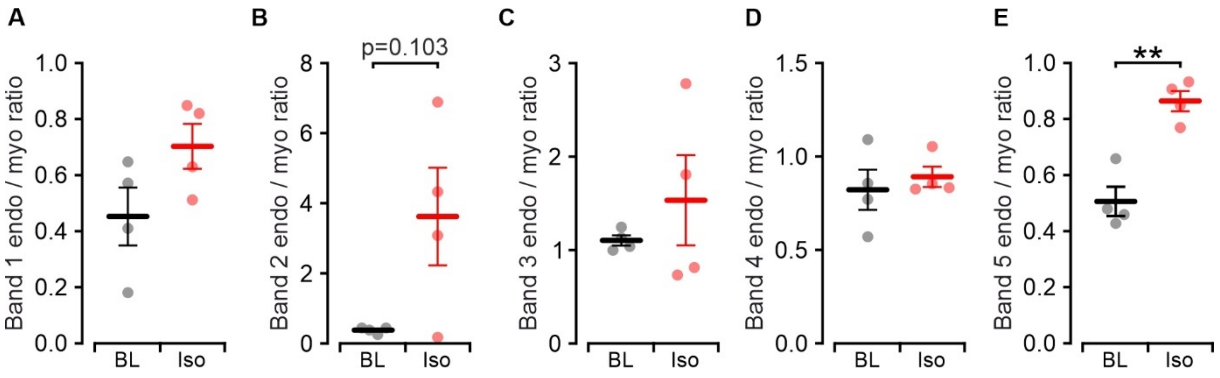

Figure 28: Endocardial-myocardial phosphorylation ratio upon adrenergic stimulation.
A-E) Endocardial to mid-myocardial ratio of phosphorylation in basal (BL, black) and Iso stimulated (red) tissue (band 1, 4, 5: unpaired student's t-test; band 2, 3: unpaired Welch's corrected t-test) for each band shown in Fig. 27A,B.

Because the estimated molecular weight of the protein in band 5 correlated with the PLN band at ~10kDa (Fig. 26C), a specific antibody for Ser16 phosphorylated PLN (P-PLN) was subsequently used to analyze PLN phosphorylation status. These results confirmed that basal PLN phosphorylation was significantly reduced in subendocardial tissue (Fig. 29A,C). Even though the difference was still significant in Iso perfused hearts (Fig. 29B,D), Iso stimulated hearts had a higher endo/myo ratio, indicating a stronger phosphorylation of PLN in the endocardium than the epicardium (Fig. 29E). However, this effect was not significant due to a higher variability in the Iso group (p=0.076). Nevertheless, the results of the western blot analyses of RRXS*/T* band 6 and P-PLN indicate a transmurally differential phosphorylation of PLN by PKA, which poses a potential explanation for the G_s-induced PVC generation in the subendocardium.

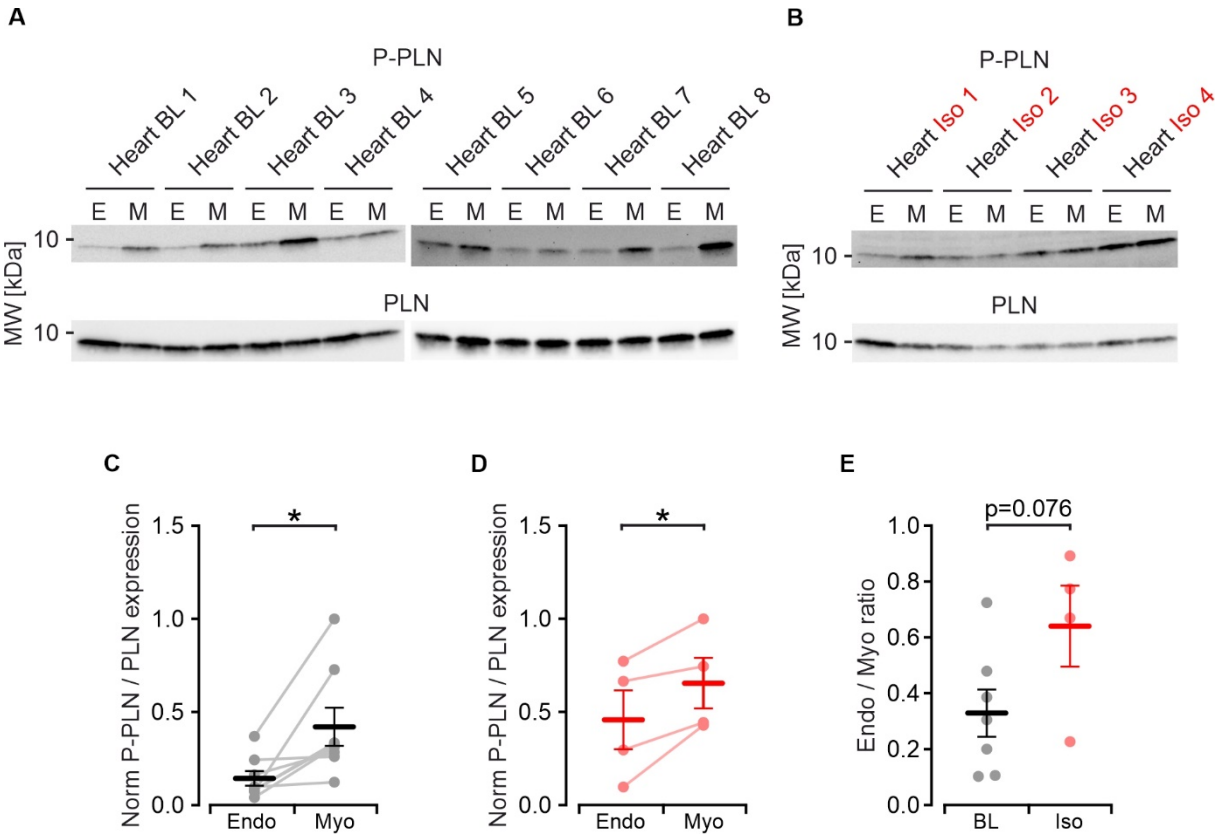

Figure 29: Local PLN phosphorylation.
A,B) Western blot of Ser16 phosphorylated PLN (P-PLN) and corresponding PLN expression. Tissue collected from basal (A) or stimulated (B, 1 µM iso, 5 min) Langendorff-perfused hearts (E: subendocardial tissue; M: midmyocardial tissue). C,D) Rel. PLN phosphorylation normalized to PLN expression and rel. to highest P-PLN/PLN ratio (bl (grey): N=8, Iso (red): N=4, paired student's t-test). E) Endocardial to myocardial ratio of phosphorylation in basal (black) and Iso stimulated (red) tissue (unpaired student's t-test).

3.13 Influence of G_s-activation on the refractory period and APD of ventricular cardiomyocytes

In the previous results sections, it was shown that G_s-signaling triggered PVCs and triggered VTs from the endocardium. However, CPVT patients specifically suffer from polymorphic and bidirectional reentry VT, which may further devolve into VF and thus cause sudden cardiac death. The molecular mechanism for VT trigger via G_s-induced SR calcium leak has been studied extensively. However, only limited studies were conducted on the influence of G_s-signaling on the modulation of the substrate of a reentry VT, which is critical for the duration and complexity of the VT leading to sudden cardiac death.

To first investigate G_s-effects on reentry VT inducibility, electrical S1S2 stimulation provided an ectopic premature trigger to the Langendorff-perfused hearts. For this, an electrode was placed onto the base of the RV and the heart was paced at 150 ms for 6 consecutive S1 pulses at 150 ms cycle length,

followed by an S2 pulse fixed at a delay close to the effective refractory period of each heart. This delay was determined before the start of the experiment as the last captured beat when shortening the S2 beat in 5 ms steps, resulting in 40-60 ms interpulse periods. The S1S2 protocol was repeated every 10 s. During this, the epicardium of the RV was illuminated after 30 s for a total of 70 s (Fig. 30A). It was observed that after the second S1S2 stimulation during illumination (approx. 10 s after start of illumination), the hearts did not capture the S2 beat anymore. This light effect lasted about 30 s before the S2 pulse was captured again, still during illumination (Fig. 30B,C). The illumination period was thus divided for the analysis into an early activation (P1, 10-40 s) and a late activation (P2, 40-70 s) phase. During P1, the S2 capture rate was significantly reduced compared to S2 capture rate before illumination as well as phase P2 (Fig. 30D). This could indicate a transient prolongation of the effective refractory period in the JellyOp hearts. This effect was independent of the Casq2 genotype (Fig. 30D, purple vs. blue dots).

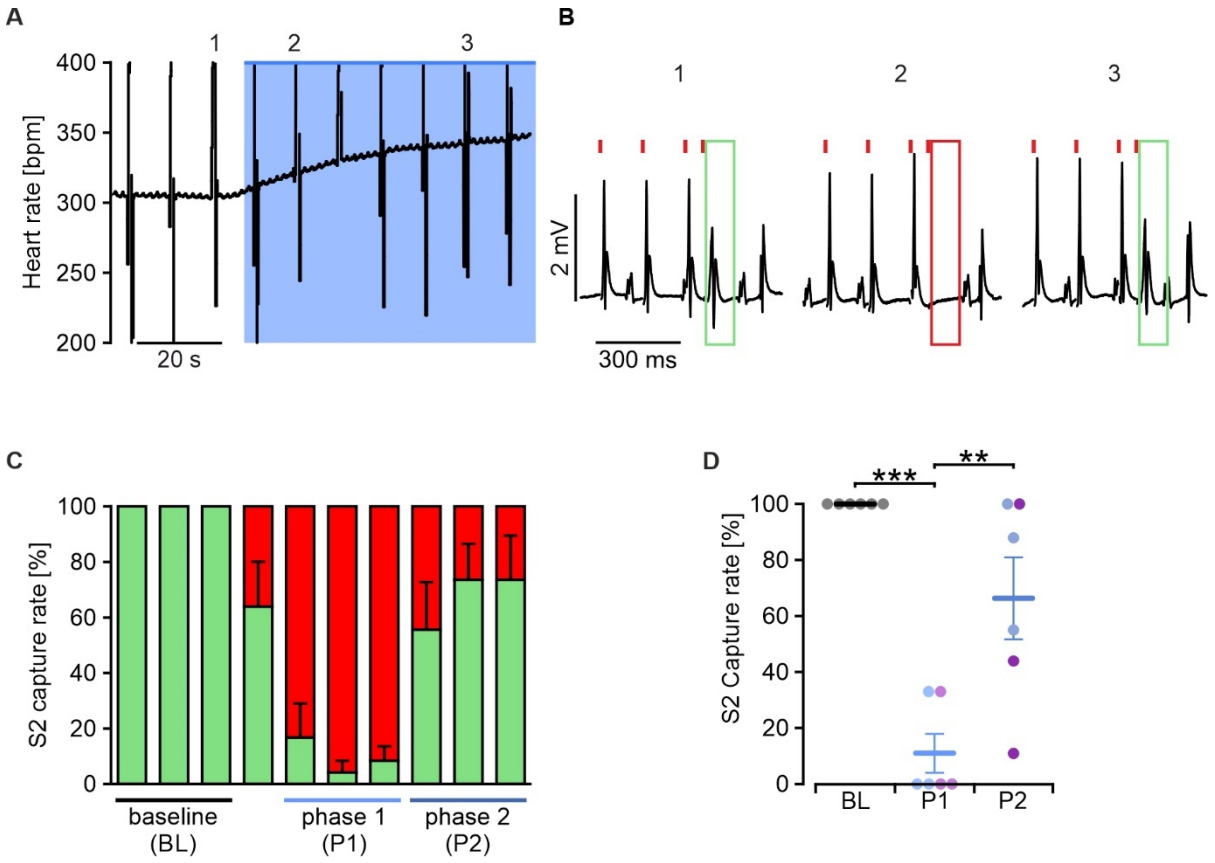

Figure 30: S1S2 capture rate upon illumination.
A) Exemplary heart rate trace during an illumination protocol. S1S2 electrical stimulation was performed every 10 s. After 3 baseline stimulations, the RV was illuminated for 70 s (2 mW/mm^2, blue bar). B) Exemplary ECG recordings of S1S2 electrical stimulation (red lines) before illumination (1), at 12 s illumination (2) and at 52 s illumination (3) (1-3 labeling corresponds to labeling in A); green box indicates capture, red box indicates no capture. C) S2 capture rate for the illumination protocol depicted in A (N=6) D) S2 capture rate grouped in baseline (black), early phase (P1: 10-40 s, Casq2 +/+: light blue; Casq2 -/-: light purple) and late phase (P2: 40-70 s; Casq2 +/+: dark blue; Casq2 -/-: dark purple;) as indicated in (C); one-way ANOVA with Tukey's multiple comparisons post-test.

To further characterize the cause for the increased effective refractory period, action potentials of cardiomyocytes were measured in the LV by sharp electrode in electrically paced Langendorff-perfused Casq2 -/- JellyOp pos. hearts. For this, the hearts were paced electrically at a steady interpulse period of 185 ms. Action potential duration at 60% repolarization (APD60) increased upon illumination by 5.6 ± 1.0 ms (Fig. 31). Thus, the transient increase of the effective refractory period in the S1S2 stimulation protocol can be explained by an APD prolongation upon G_s-stimulation.

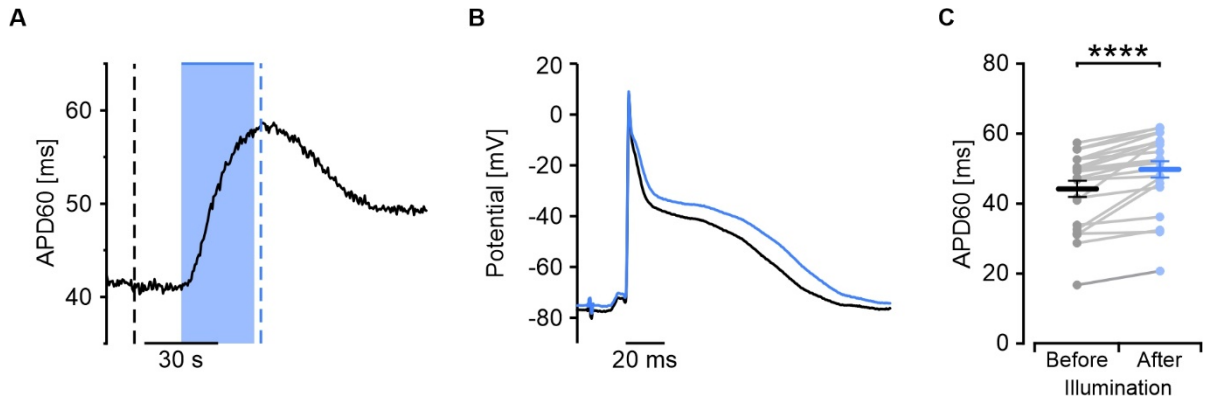

Figure 31: APD prolongation upon G_s-stimulation.
A) Exemplary trace of APD60 of a Casq2 -/- JellyOp pos. cardiomyocyte in the LV during illumination (blue bar; 30 s, 0.83 mW/mm^2 epicardial on the LV) during ventricular, electrical pacing at 185 ms interpulse period. B) Exemplary action potential traces before illumination (black trace, corresponding to dotted black line in A) and at peak response of illumination (blue trace, corresponding to dotted blue line in A). C) APD60 before and at maximal response of illumination of Casq2 -/- JellyOp pos. LV cardiomyocytes (n=14; N=3, paired student's t-test).

3.14 VT incidence during optogenetic G_s-stimulation upon arrhythmic triggering

This transient increase of the refractory period may indicate an interesting mechanism in the temporal activation kinetics of the G_s-signaling cascade. Nevertheless, when evaluating the risk of arrhythmia during G_s-activation, S2 capture had to be ensured. Thus, in the next experiment, S2 pacing was increased to 5 ms above the capture threshold to compensate for the light-induced 5 ms increase in APD60. In this setting, S1S2 reliably captured and VTs could be induced. VT incidence was significantly increased in Casq2 -/- JellyOp pos. mice during illumination compared to Casq2 -/- JellyOp neg. mice (Fig. 32). The comparison to illuminated Casq2 -/- JellyOp neg. mice proved a clear role of G_s-activation on the VT generation and excluded unspecific phototoxic light effects. Incidence of sustained VTs longer than >300 ms was also significantly increased and displayed a polymorphic reentry VT morphology (Fig. 32A). Interestingly, Casq2 +/+ JellyOp neg. mice had significantly less VTs, indicating that SR calcium handling might not only be involved in the VT trigger due to the generation of DAD but also modulate the VT substrate to favor the stabilization of reentry VT.

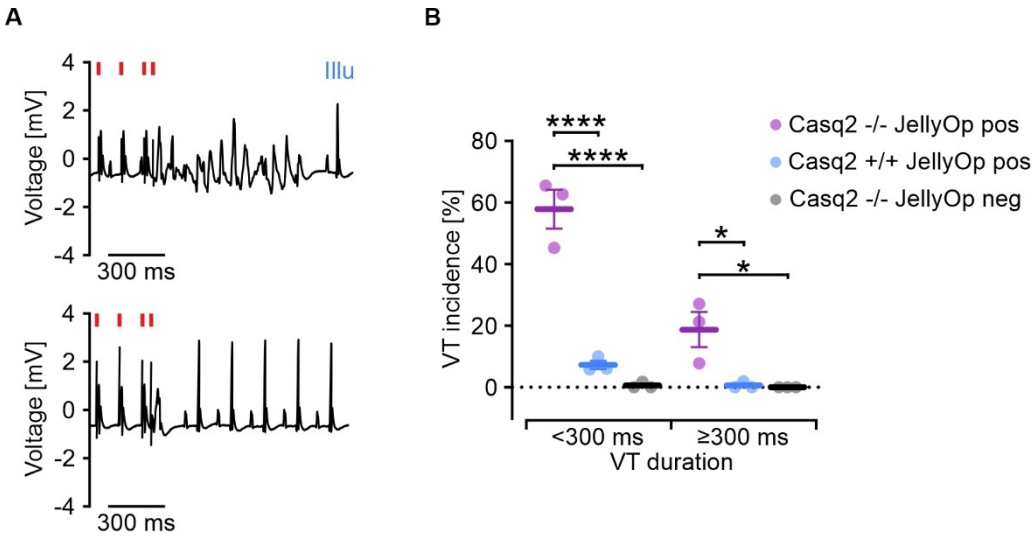

Figure 32: Triggered VT incidence upon G_s-stimulation.
A) Exemplary trace of an S1S2 electrical stimulation during (upper panel) and before (lower panel) illumination (4 mW/mm^2, 90 s). B) VT incidence during illumination (90 s from start of illumination of the RV, S1S2 protocol every 10 s) in the three genotypes (Casq2 -/- JellyOp pos: purple; Casq2 +/+ JellyOp pos.: blue; Casq2 -/- JellyOp neg.: grey) grouped by VT duration (<300 ms or ≥ 300 ms); one-way ANOVA with Tukey's multiple comparisons post-test.

Voltage mapping was performed to investigate the source of the generation of a reentry VT upon S1S2 premature triggering. For the combination of voltage mapping with optogenetic stimulation, a red-shifted voltage-sensitive dye was used because its excitation and emission spectrum (exc. 660 nm; em. 795 nm) are outside of the activation spectrum of JellyOp (Fig. 11F).

In a JellyOp pos. heart displaying reentry VT upon S1S2 trigger after illumination, the conduction of the excitation during the last S1 pulse and the S2 pulse was visualized using the activation map of the action potential. Under baseline conditions before illumination, the conduction velocity measured in three areas of the heart (Cv1: anterior LV base; Cv2 and Cv3: anterior RV apex) was lower in the S2 pulse than in the S1 pulse (Fig. 33A+B). Illumination only had a small effect on the conduction velocities of the S1 pulse (Fig. 33A+C), but a strong effect on the conduction velocities of the S2 pulse (Fig. 33B+D): After illumination, the conduction velocity of Cv1 of the S2 pulse was increased compared to baseline (0.55 m/s after illumination and 0.36 m/s at baseline), Cv2 was strongly increased (2.72 m/s after illumination and 0.32 m/s at baseline), and Cv3, which was selected adjacent to Cv2 following the excitation wave of the S1 pulse, was strongly reduced (0.14 m/s after illumination and 0.25 ms at baseline). The S2 activation map (Fig. 33D) indicated a conduction block and an excitation of the remote area behind the conduction block from the LV.

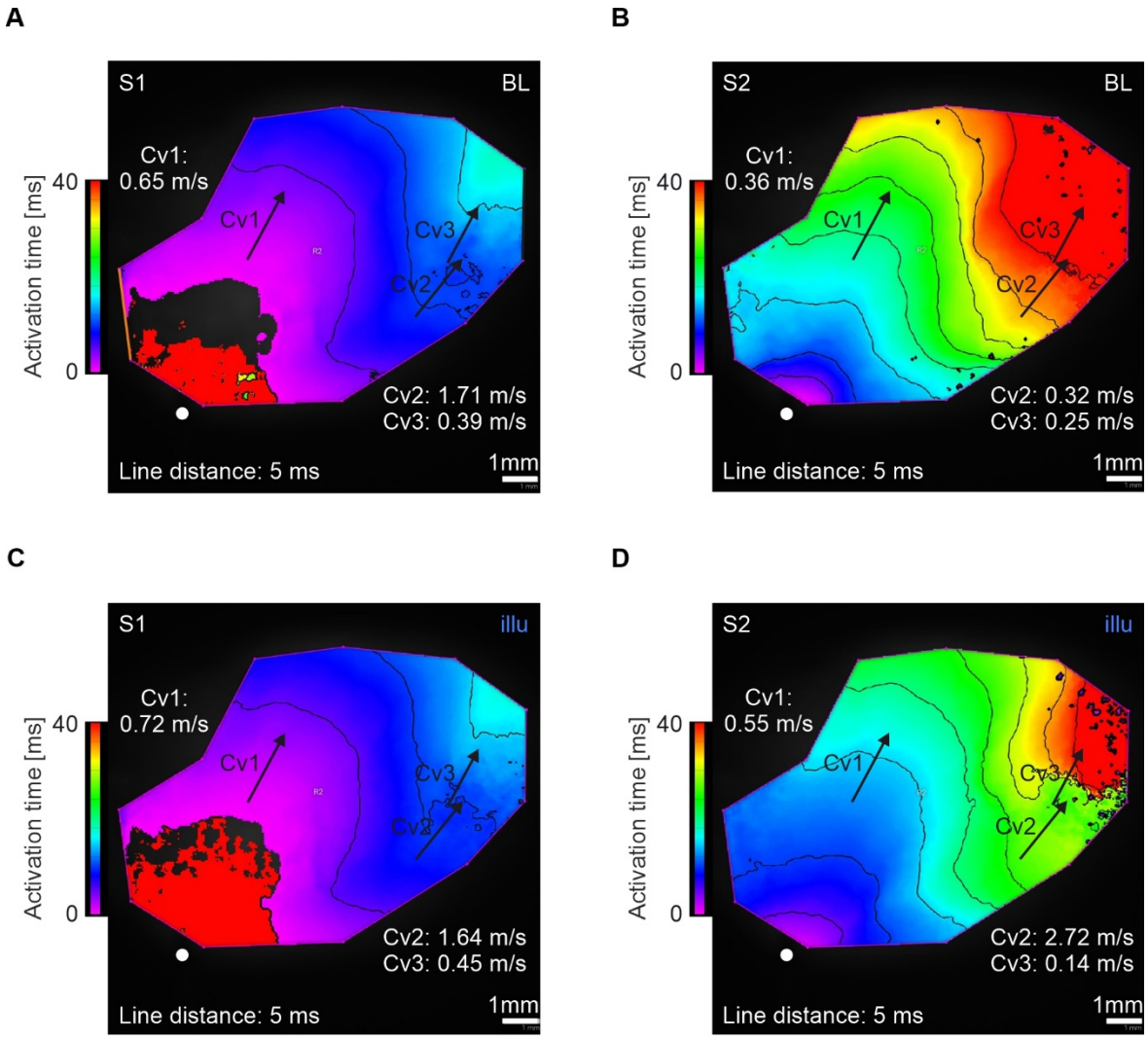

Figure 33: Conduction of S1 and S2 stimulated excitation.
A+B) Activation map of S1 (A) and S2 (B) stimulated excitation under baseline conditions (BL). C+D) Activation map of S1 (C) and S2 (D) stimulated excitation 30 s after start of illumination. Black arrows indicate line selections for conduction velocity measurements (Cv1, Cv2, Cv3); White dots show pacing electrodes, from which the excitation wave propagates. Voltage mapping was performed after staining with Di-4-ANEQ(F)PTEA.

3.15 Modulation of VT complexity by optogenetic G_s-stimulation

The previous experiments showed that G_s-activation influenced VT substrate, increasing VT incidence after a premature trigger. However, the resulting VTs were too short to assess the influence of G_s-activation on VT complexity. JellyOp mice were, thus, perfused with the ATP-sensitive potassium (K_{ATP}) channel opener pinacidil for this assessment. Pinacidil shortens the APD, so that stable-running reentry VTs, similar to VTs in humans, can be induced. By electrical burst pacing (20 Hz, 2 s) on the base of the RV, reentry VTs with a predominantly monomorphic morphology were induced. These VTs were investigated by ECG recording and voltage mapping.

After a stable-running monomorphic VT was induced, the anterior ventricles were illuminated (5 s, 1.5 mW/mm^2). Illumination decreased VT frequency from 19.8 ± 0.4 Hz to 18.1 ± 0.4 Hz (n=10, N=4) (Fig 34A,B). In rare cases (n=3, N=3), the frequency of the VT became unstable after illumination and the ECG signal exhibited a clear shift from a monomorphic VT to a polymorphic VT (Fig. 34C,D). In a case of such a shift in the ECG morphology, voltage mapping of the anterior epicardial surface of the ventricles revealed a stable rotor before illumination (Fig. 34D, upper panel) with a dominant frequency of 19.5 Hz in the LV as well as the RV (Fig. 34E, upper panel). After illumination, the rotor became unstable, with the rotor core meandering through the RV (Fig. 34D, lower panel). The dominant frequency in the LV decreased slightly to 17.1 Hz, while in the RV, the dominant frequency doubled to 34.2 Hz (Fig. 34E, lower panel).

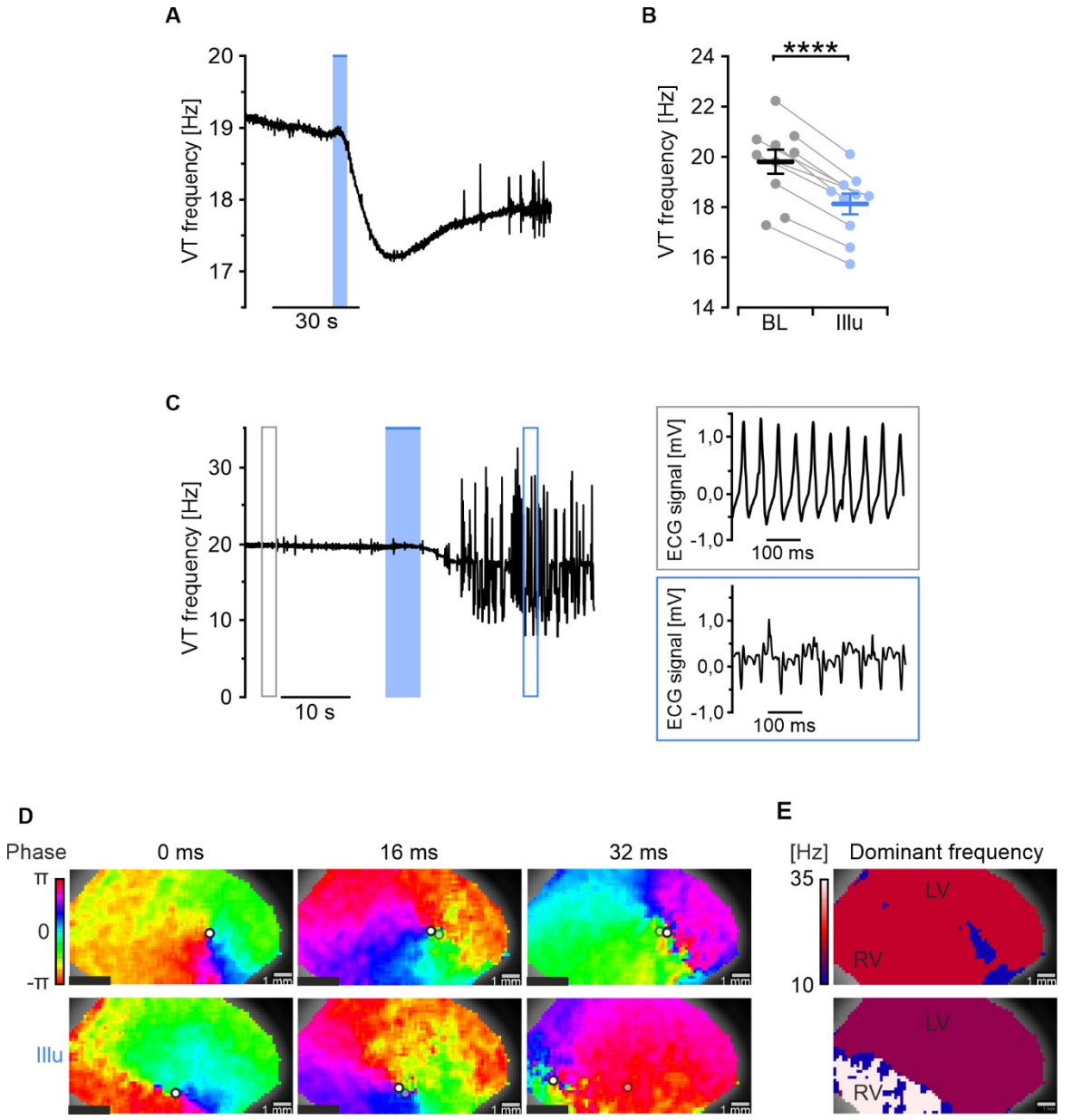

Figure 34: G_s-activation influences reentry VT frequency and morphology.
A) Frequency response of a reentry VT induced by burst pacing during perfusion with 100 nM pinacidil upon illumination (blue bar, 5 s, 1.5 mW/mm^2) in a JellyOp pos. heart. B) VT frequency before (BL, black) and upon maximal illumination effect (Illu, blue); n=10; N=4; paired student's t-test. C) VT frequency trace of a reentry VT that shows a switch from a regular to an irregular frequency upon illumination (blue bar, 5 s 1.5 mW/mm^2) with corresponding ECG traces before (right panel, grey inlet) and after illumination (right panel, purple inlet). D) Voltage mapping of the anterior wall of the LV and RV of the heart depicted in C reveals a stable rotor before (upper panel) and a meandering rotor (lower panel) after illumination. Depicted are phase maps at three time points before and after illumination; rotor core marked with ○ and previous core position in transparent. E) Dominant frequency of a 1.5 s recording before and after illumination as shown in C+D. Voltage mapping was performed after staining with PGH-1.

3.16 Ventricle-specific optogenetic modulation of VT complexity

The previous chapter showed a differential response upon transition to a higher complexity VT in the RV and the LV. To further investigate the differential complexity of the VTs in the LV and RV, local ECG recordings of the LV and RV were recorded by placing a silver-chloride electrode onto the free wall of the respective ventricle and using the metal spoon placed on the dorsal septal area of the heart as the indifferent electrode (Fig. 35A). Half of the anterior ventricular walls were illuminated to activate JellyOp selectively in the LV or the RV. This local illumination led to an observed increase in complexity of the ECG morphology. While RV ECG, after illumination, showed a polymorphic or VF-like morphology (Fig. 35B, blue box), LV ECG mostly displayed alternans morphology (Fig. 35C, blue box).

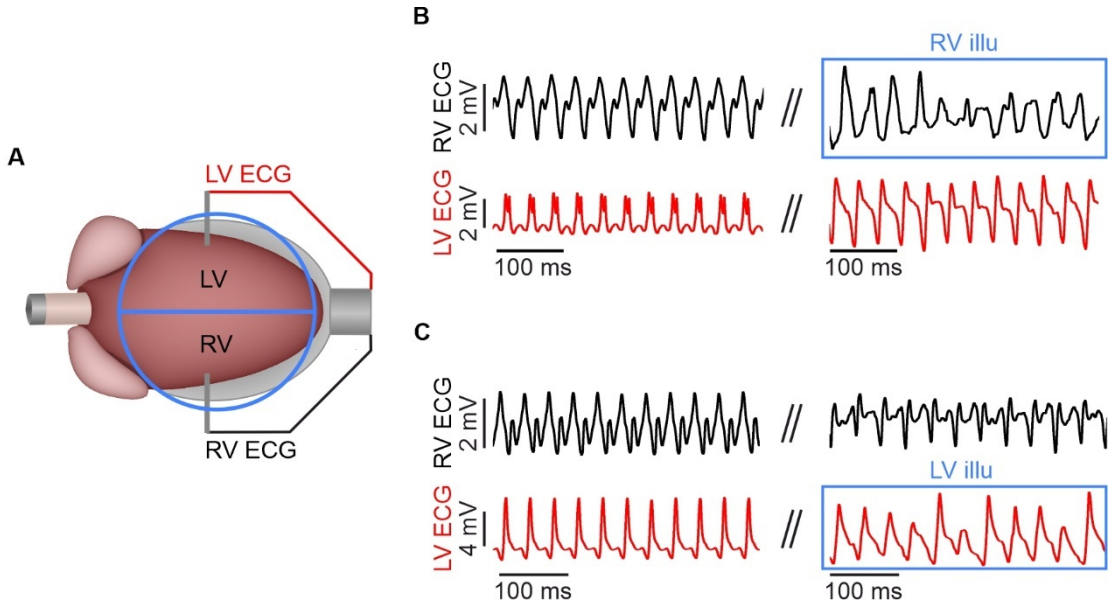

Figure 35: Ventricle-specific VT modulation.
A) Schematic of a Langendorff-perfused heart with the electrodes placed for local ventricular ECG (LV ECG in red and RV ECG in black) with half-circular illumination indicated by blue outline. B,C) Representative local electrograms with ECG leads placed on the RV (black) and LV (red) free wall before (left panel) and after (right panel) illumination (2 s, 1.0 mW/mm^2) of the RV (B) and LV (C). Note the higher VT complexity and frequency in the ECG leads of the illuminated regions.

To analyze and quantify the observed change in morphology of the ECG signals, the frequency components of the ECGs displayed in Fig. 35B,C were further analyzed using an FFT analysis. Under baseline conditions, the FFT amplitude spectrum consisted of one dominant frequency with its harmonics at approx. 22 Hz. After RV illumination (Fig. 36 A,B), several irregular frequencies occurred in the RV ECG FFT in addition to the dominant frequency (Fig. 36B, green box). The LV ECG FFT mostly remained stable with a slight shift to the higher harmonics of the dominant frequency. LV illumination

(Fig. 36C,D) induced a pronounced disarray in the LV ECG FFT (Fig. 36D, green box). The RV ECG FFT was altered by an almost complete loss of the lower baseline frequency and a shift to the higher harmonics (double) frequency.

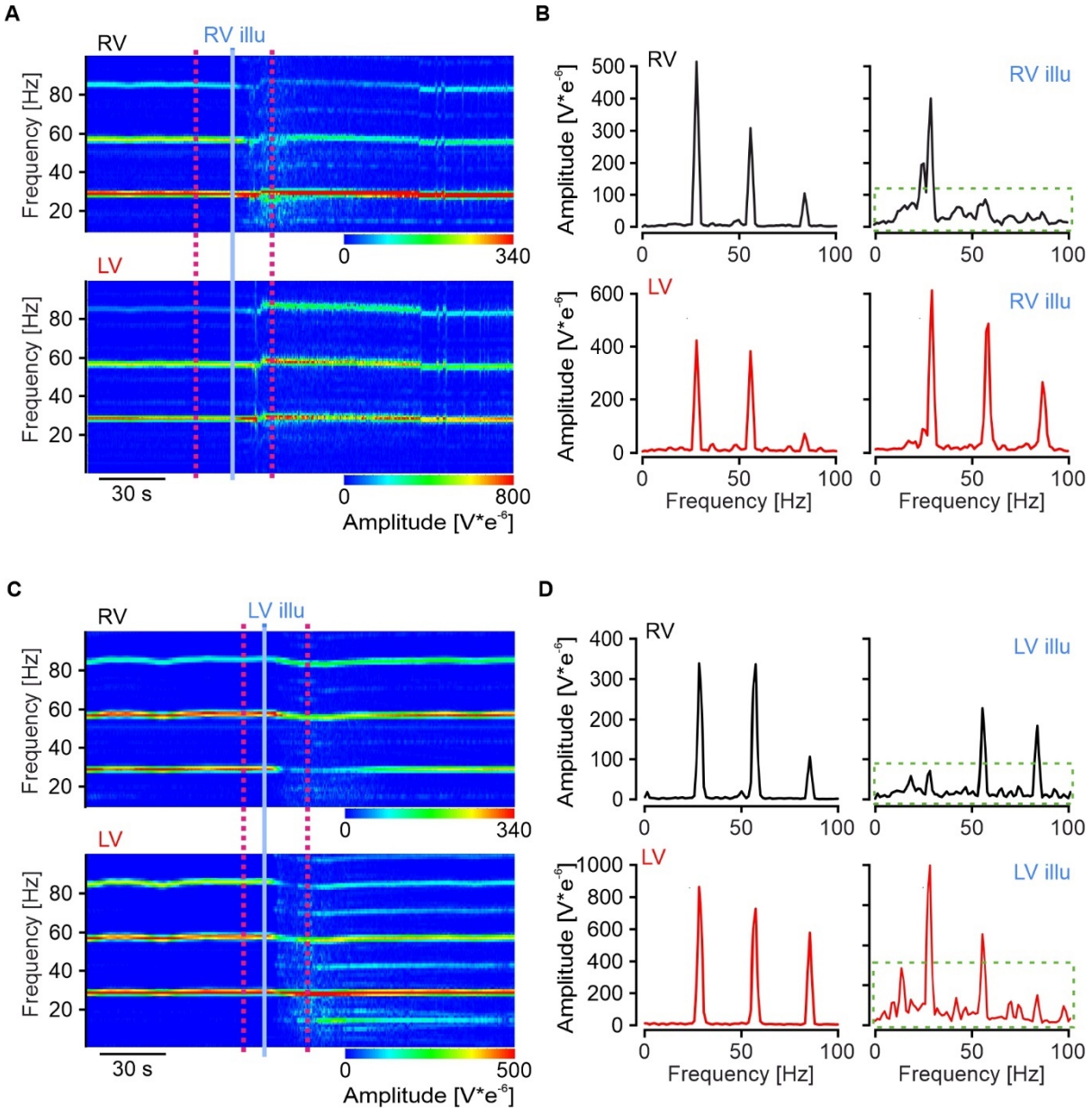

Figure 36: FFT of a reentry VT upon G_s-stimulation.
A) Time course of the FFT amplitudes of the RV ECG (upper panel) and the LV ECG (lower panel) during RV illumination (blue bar). B) FFT Amplitudes corresponding to time points before (left panel) and after (right panel) RV illumination as indicated in A by pink dotted lines. C) Time course of the FFT amplitudes of the RV ECG (upper panel) and the LV ECG (lower panel) during LV illumination (blue bar). D) FFT Amplitudes corresponding to time points before (left panel) and after (right panel) RV illumination as indicated in C by pink dotted lines.

Especially the irregularity of the higher frequency interval could be an indicator for a polymorphic or VF like morphology. To quantify the irregularity in the high-frequency component, the standard deviation (SD) of the frequency in an interval including the second harmonic (35-40 Hz) up to 100 Hz was calculated. Fig. 37A shows an exemplary time course of the SD of the RV ECG (upper panel) and the LV ECG (lower panel) during illumination of the RV (the example corresponds to the traces in Fig. 35B and Fig. 36 A,B). The SD increases rapidly in the RV and the LV after illumination. For statistical analysis the mean of the high frequency SD in a 30 s interval before illumination (BL) and 30 s interval after illumination (Illu) were compared. RV illumination induced a significant increase in the SD in the RV ECG and the LV ECG. The increase of the SD was slightly larger for the RV ECG with an increase of 17.19 ± 4.46 % compared to the LV ECG, which showed an increase of 9.37 ± 4.11 %. Illumination of the LV, however, did not show a significant change in SD of the high-frequency component in either ventricle, even though in some cases an increase in complexity was observed as shown in the previous examples (Fig. 36 C,D).

Taken together, the illumination of both ventricles simultaneously during a monomorphic VT induced a doubling of the dominant frequency in the RV (Fig. 34D,E). This led to the investigation of local G_s-stimulation of the RV and the LV. This local stimulation further implicated the RV as the driving force in the switch of the VT to higher complexity with increased irregularity in the higher frequencies.

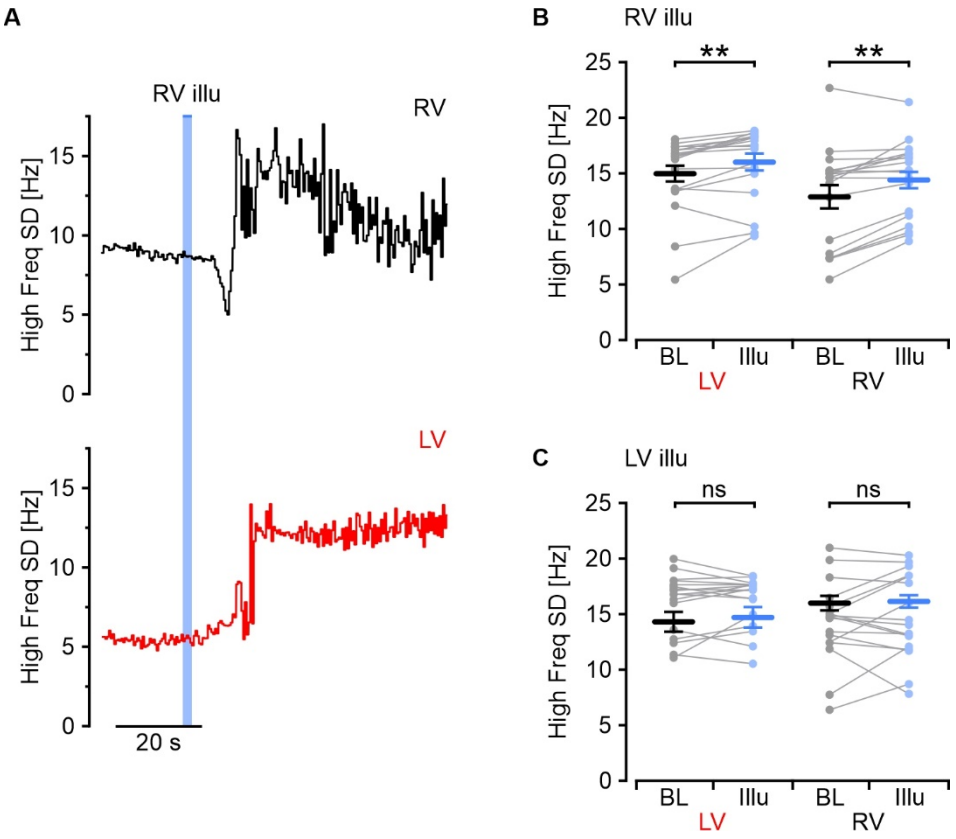

Figure 37: Irregularity of high frequencies during ventricle-specific G_s-stimulation.
A) Exemplary traces of the standard deviation of the high-frequency FFT component (High Freq SD; 35-100 Hz) during RV illumination (blue bar). Upper panel shows High Freq SD of the RV ECG (black), lower panel shows that of the LV ECG (red). B,C) Mean High Freq SD 30 s before (BL) and 30 s after illumination (illu) during RV illumination (B) or LV illumination (C) (RM one-way ANOVA; n=17-18; N=3).

4 Discussion

4.1 The significance of G_s-induced ventricular arrhythmias

Sudden cardiac death is one of the leading causes of death worldwide accounting for an estimated 15-20% of all deaths[184]. Most commonly, it occurs due to fatal ventricular arrhythmias in structurally diseased hearts, e.g. after myocardial infarction or in heart failure, but also due to hereditary arrhythmia syndromes. Apart from ICDs, β-blockers are one of the most effective therapies against ventricular arrhythmias in patients with increased risk showing that G_s-signaling has a strong proarrhythmic effect. The main mechanism for VT generation after β-adrenergic activation is DADs due to calcium leak from the SR. The prerequisite for this is an increased leakiness of the RyR2. In the hereditary disease CPVT, this leakiness can be caused by mutations in RyR2, which can cause increased opening of the receptor, or Casq2, which leads to more free calcium in the SR. β-adrenergic stimulation then further enhances this leak, e.g. by phosphorylation of RyR2. Another mechanism of acquired calcium leak has been observed in heart failure, where cardiomyocytes show hyperphosphorylation of RyR2 at baseline, which leads to increased diastolic calcium leak. Because both heart failure patients and CPVT patients display increased sensitivity to β-adrenergic VT generation by diastolic calcium leak, insights gained from CPVT mouse models could also be transferred to the arrhythmia formation in other heart diseases like heart failure.

β-blockers are one of the most effective treatments against VT to date. However, many patients are unresponsive to currently available antiarrhythmic drug therapies, suffer from recurrent VT and have to rely on an ICD. ICDs can prevent sudden cardiac death with a high success rate but they do not prevent the onset of arrhythmias and thus still severely impact the patients' quality of life. Adverse effects of ICDs include severe pain, especially by inappropriate shocks, which can additionally cause a psychological burden[185]. Moreover, damage of cardiac tissue by electroshocks and risk of infection lead to increased mortality[186,187].

Thus, it is necessary to investigate further the cause of the arrhythmogenic potential in the G_s-signaling cascade and identify vulnerable areas in the heart to develop drugs to target the origin and mechanisms of G_s-induced arrhythmias more directly. This can lead to more effective treatments with fewer side effects to reduce cardiac death and improve quality of life in CPVT patients as well as other heart disease patients with increased risk for ventricular arrhythmias.

4.2 Optogenetics as a tool to study ventricular arrhythmias

Optogenetics has been used to study heart function and arrhythmia for several years. Bruegmann et al., for example, demonstrated the potential of depolarization with ChR2 to be used as a tool for defibrillation of VT[159], while Funken et al. also terminated VT using hyperpolarization by the light-gated proton pump ArchT[188]. Most studies have focused on tools directly influencing membrane potential using light-activated ion channels. In this thesis, a light-inducible GPCR was used for the first time to investigate the influence of G_s-signaling on VT in the whole heart. Previously, a transgenic mouse line expressing JellyOp, a blue light-activated G_s-coupled GPCR, was established and characterized by Makowka et al.[160]. JellyOp signaling activated by light in embryonic as well as adult cardiomyocytes has similar effects on pacemaking activity and contractility as pharmacological activation of the endogenous β-adrenergic signaling cascade by iso. In this thesis and as part of the previously mentioned publication[160], JellyOp response was further characterized in Langendorff-perfused hearts. JellyOp effectively elevated heart rate upon SA node stimulation with much faster activation and deactivation kinetics than Iso perfusion (Fig. 11A-E). The measured activation times and deactivation times of the heart rate response much more directly correlate with the activation and deactivation of the G_s-signaling cascade and can give temporal insights into cAMP production and hydrolyzation, while this is not possible with agonist perfusion and wash-out. The heart rate response during illumination (Fig. 11A) shows an initial peak, after which the heart rate decreases slightly to a stable plateau during prolonged illumination. This corresponds well with previously observed cAMP concentration responses during β-adrenergic stimulation in rabbit and mouse cardiomyocytes, which also display a slightly decreased plateau after the initial peak with similar kinetics[189,190]. The fact that no wash-out is necessary also permits repeatedly activating G_s-signaling in a short period, which is made possible by the fact that JellyOp activation does not show a “bleaching” effect upon repeated activation[170]. This allows direct comparison of different activation areas, intensities and durations. Important for the combination with voltage mapping, the activation spectrum of JellyOp was defined by measuring the heart rate increase at different wavelengths. Activation up to 600 nm was detected without effects at 650 nm (Fig. 11F). This makes JellyOp compatible with far-red imaging, which was used for optical voltage mapping of VT in the JellyOp hearts.

4.3 Establishing a model for local light-activated G_s-signaling in Langendorff-perfused hearts

To show that distinct areas of the Langendorff-perfused heart could be selectively activated by light, three areas (atria, AV septal area and ventricles) were separately illuminated. Each illumination area

led to distinct responses upon illumination in the ECG: heart rate increase and supraventricular arrhythmias upon atrial illumination, junctional rhythm upon illumination of the AV node and only a small effect on heart rate upon illumination of the ventricle (Fig. 12).

Arrhythmias in the form of junctional arrhythmias were observed under baseline heart rate in the Langendorff-perfused hearts upon Iso injection as well as illumination specifically of the AV septal region, where the AV node is located. These arrhythmias have also been described to precede VT in Casq2 -/- mice[30] and could indicate a hypersensitive AV node and/or conduction system to G_s-stimulation.

The main aim of the thesis, however, was to study the influence of adrenergic G_s-signaling on PVC and VT. Therefore, the JellyOp mouse line was crossed with a mouse model for CPVT due to a knockout of Casq2 (Casq2 -/-)[173,178]. Casq2 deficiency promotes diastolic calcium leak from the SR, commonly described as one of the central mechanisms for the induction of VT in CPVT[131]. In previous publications on the Casq2 -/- mouse, PVCs were induced in anesthetized mice upon Iso injection under a heart rate, which was only slightly reduced due to the anesthesia. However, in the Langendorff-perfused hearts used in this thesis, ventricular PVCs did not occur at normal heart rate but only after heart rate reduction by Cch perfusion or atria removal (Fig. 13,14). The lack of VT at baseline frequency (approx. 300-350 bpm) in the Langendorff-perfused heart might be explained by the lack of innervation due to excision of the heart, which abolishes normal sympathetic and parasympathetic tonus, thus potentially making it more difficult to induce PVCs by Iso than in anesthetized mice with intact autonomic innervation. Moreover, PVCs and VTs only occurred when hearts were perfused with bicarbonate-buffered KH buffer but not with HEPES buffer. This might indicate that pH fluctuations could play a role in the contribution to PVC generation.

After pharmacological reduction of the heart rate (to approx. 100-150 bpm), stimulation of JellyOp was capable of inducing VTs in the JellyOp x Casq2 -/- mice in a similar fashion as Iso perfusion and morphologically similar to what was previously reported by Knollmann et al. in anesthetized Casq2 -/- mice[173] (Fig. 16).

4.4 Slow heart rate promotes VT generation

Stimulation of M2 muscarinic acetylcholine receptors in the SA node with Cch was used to decrease heart rate, which led to an increase of VT occurrence after G_s-stimulation with Iso or light. However, it cannot be excluded that Cch perfusion had additional effects on the ventricle besides the observed heart rate reduction in the SA node. The general understanding is that the parasympathetic nervous

system mainly affects the SA node and the AV node in the atria by the release of acetylcholine, which activates M2 receptors. However, cholinergic nerves can be found in lower density also in the ventricles and ventricular cardiomyocytes were found to express M2 receptors[59,191]. Thus, an additional effect of Cch perfusion on the ventricles, which could modulate VT inducibility, cannot be excluded. Abolishing the sinus rhythm by surgical removal of the atria allowed a more direct assessment of the influence of heart rate on PVC and VT generation because the ventricles could then be paced electrically at low frequencies without additional pharmacological manipulations. At 200 bpm, PVCs occurred reliably upon illumination of the endocardium in the Casq2 -/- JellyOp pos. hearts. Notably, an increase of pacing frequency to 400 bpm completely abolished these PVCs (Fig. 18). This could be explained by the mechanism of PVC induction through slow calcium leak via RyR2 and accumulation in the cytosol until a threshold for the generation of an action potential is reached. If the intrinsic or the paced beating frequency is higher, and thus the diastolic interval is shorter, there is not enough time for calcium leak to accumulate in the cytosol. When the diastolic interval is longer, enough calcium accumulates in the cytosol and is subsequently electrogenically exchanged for sodium by NCX to depolarize the cell to its threshold potential for spontaneous action potential initiation. The PVC burst period after illumination of the endocardium also supports this mechanism: The time from one PVC to the next was on average 173.5 ± 6.0 ms (Fig. 21C), thus the pacing interval at high pacing frequency (150ms pacing interval at 400 bpm) is shorter and overrides PVC generation.

Low beating frequency might also play an important role in human G_s-induced VT generation, as CPVT patients often present with resting bradycardia[143], with a resting heart rate of 60 bpm in children with diagnosed CPVT (approx. 30-40 bpm lower than normal resting heart rate in children)[132]. Moreover, CPVT patients also displayed an impaired chronotropic response upon β-adrenergic stimulation[192,193]. An impaired chronotropic response was defined by the heart rate reserve, the difference between the peak heart rate and the resting heart rate, relative to the age-predicted relative heart rate. CPVT patients with such chronotropic incompetence, with a heart rate reserve <80%, also displayed higher ventricular arrhythmia scores and more syncope events during exercise-stress testing. Asymptomatic CPVT patients had a heart rate reserve of 93.2%, while CPVT patients displaying syncope or sudden cardiac arrest during exercise-stress testing had heart rate reserves of 85.9% and 64.7%, respectively[192]. Chronotropic incompetence was also reproduced in a RyR2 mutant mouse model. SA nodal cells were found to have reduced SR calcium content in the presence of Iso and reduced LTCC current density[194]. In CPVT models these SA node dysfunctions are hypothesized to be caused by alterations in the so-called Ca^{2+}-clock mechanism, wherein calcium release from the SR contributes to (especially late-phase) diastolic depolarization. However, the exact mechanism is yet unknown[194–196]. Also, it is unclear whether SA node dysfunction is only a byproduct of a stronger CPVT phenotype or directly contributes to a more severe ventricular arrhythmia score. The results of this thesis showing

that slow heart rate could be an important risk factor for calcium leak-induced arrhythmias is in accordance with previous work in CPVT mice by Faggioni et al.[197]. This study performed in Casq2 -/- mice and mice with RyR2 mutation ($RyR2^{R4496C/+}$) reported that an increase in sinus rate by blocking of the parasympathetic system with atropine injection or atrial tachypacing before Iso injection significantly reduced the occurrence of VT *in vivo*. This was also transferred to patients in a small study with six CPVT patients[198]. Ventricular ectopy was observed in all six patients in exercise-stress tests, even though four of these patients had β-blocker (nadolol) medication. Pre-exercise intravenous injection of atropine reduced and, in four patients, entirely prevented the generation of ectopic ventricular activity. Atropine injection was accompanied by a baseline increase in sinus rate (52 bpm to 98 bpm), but there was no significant difference in peak sinus rate during exercise. Therefore, increasing the resting heart rate either pharmacologically or by atrial tachypacing could improve CPVT patient treatment in addition to β-blockers.

Atropine is used for the acute treatment of bradycardia, but various side-effects of parasympathetic inhibition make it incompatible with long-term use. Another drug tested in the treatment of SA node dysfunction is the adenosine antagonist theophylline[199]. However, theophylline also has adverse effects, including increased arrhythmogenicity[200]. Rate-responsive atrial tachypacing could be the treatment option with the most reliable effect and least side effects. According to the CPVT patient study[198] 90-100 bpm resting heart rate could be an effective heart rate to prevent VTs but a patient-specific threshold to the development of ectopic ventricular beats during exercise could also be tested.

4.5 Subendocardial cardiomyocytes are prone to the generation of PVCs

In patients with episodes of VT without structural heart disease, the endocardium has been often found to be the source of VT trigger and often VT can be treated by endocardial ablation. Especially the right or left ventricular outflow tract is implicated as a focal point of VT initiation in patients[201]. Nevertheless, a direct comparison of local transmural G_s-effects on VT trigger susceptibility has yet to be performed. The molecular differences in the different regions of the ventricular wall are yet to be fully discovered. Optogenetics using JellyOp provides a unique advantage for the investigation of local G_s-signaling effects by precise spatial and temporal light application in the Langendorff-perfused heart.

With this advantage, endocardial illumination of the RV and LV were compared. VT onset was significantly faster in the LV, but no significant differences in the number of PVCs or VT duration have been found (Fig. 17). To study the difference between endo- and epicardial G_s-signaling, the LV was used because its thicker ventricular wall enables separate illumination of subendocardial and subepicardial tissue while minimizing overlap by light penetration.

To accurately compare endo- and epicardial illumination, light intensity emitted from the light catheter was measured with an integrating sphere and epicardial illumination area via a macroscope was matched according to the estimated left ventricular endocardial area (Fig. 15). While this was the best available setup to compare the endocardium with the epicardium, the different illumination methods harbor some limitations: the circular illumination on the epicardium only partially compares to the illumination of the whole endocardial surface of the LV lumen. The source-sink relationship has to be considered here as well. The circular epicardial illumination is surrounded by unstimulated tissue on the borders of the illumination creating a sink, while the 360° illuminated endocardium constitutes a fully stimulated surface. Moreover, the catheter could potentially be in contact with a particular part of the endocardium, thus changing the illumination area or leading to inhomogeneous illumination intensities. These considerations have to be kept in mind in the interpretation of the results.

At the previously tested slow pacing frequency of 200 bpm, only endocardial illumination of the Casq2 -/- JellyOp pos. hearts produced a significant amount of PVCs in all hearts. Epicardial illumination, even with ten-fold higher light intensity, induced significantly fewer PVCs (Fig. 20). This indicates that the endocardium is significantly more sensitive to the generation of G_s-induced PVCs than the epicardium. Echocardiographic data estimate the LV wall thickness of mice to be 0.7 (diastole) to 1 (systole) mm[180]. Experiments of our working group on the light transmission in heart tissue slices estimate a light transmission of approx. 10% at 1 mm thickness. Therefore, the PVCs observed at 10x light intensity on the epicardium might also originate from the endocardial cardiomyocytes due to activation by penetrated light. The increased time to PVC burst start and shorter duration of these “epicardially”-induced PVC bursts could be due to an overall lower activation of the endocardial cardiomyocytes by penetrated light compared to direct endocardial illumination.

To confirm the origin of the PVCs upon endocardial illumination, the innermost endocardial cardiomyocytes were ablated using an iodine-containing Lugol solution. Lugol solution has been previously established to ablate the conduction system and Purkinje cells preferentially but has also been reported to ablate subendocardial working myocardium[181–183]. Immunohistochemical staining after Lugol solution confirmed that in these experiments, a consistent layer of subendocardial tissue had been ablated (Fig. 22A). This subendocardial ablation significantly reduced PVC generation, and in some hearts even completely abolished it, confirming the subendocardial origin of the PVCs generated after G_s-activation (Fig. 22B-F).

Multiple factors could influence the higher PVC generation in the subendocardial cardiomyocytes. The first possible cause to investigate was the expression levels of the light-sensitive receptor. Immunohistochemical staining of a JellyOp pos. heart revealed slightly lower GFP expression levels in

the subendocardium than in the mid-myocardium as well as the subepicardium, excluding higher expression in the subendocardium as the cause for higher PVC sensitivity (Fig. 23).

Another aspect is the excitability of the cardiomyocytes, which describes how easily an action potential is initiated. This depends on two main factors: the threshold membrane potential at which an action potential is elicited and the input resistance of the cell, which, according to Ohm's law, determines how much a given current changes the membrane potential. In the case of SR calcium leak, the same resulting NCX current could lead to a bigger depolarization in the endocardial cells if their input resistance is higher. Alternatively, if their threshold potential would be lower, the same depolarization could trigger an action potential in the endocardial but not the epicardial cardiomyocytes. To investigate these potential differences in excitability of the subendocardial cardiomyocytes, the same illumination methods for endo- and epicardial illumination were used to determine pacing thresholds in ChR2 pos. mice. Chr2 is a non-selective cation channel activated by blue light, thus, depolarizing the cell upon light stimulation. Hereby, the ChR2 current is proportional to the applied light intensity[158]. If the endocardial cardiomyocytes had increased excitability either by a reduced action potential threshold or by an increased input resistance, this would translate to less ChR2 current needed for the pacing of the endocardial cells. This directly correlates with a reduced light intensity needed for pacing. The excitation threshold of the subendocardial cardiomyocytes was lower than that of the subepicardial cardiomyocytes (36.9 ± 8.0 µW/mm^2 and 71.1 ± 19.2 µW/mm^2, respectively; Fig. 24) pointing to increased excitability. However, this approx. two-fold difference cannot adequately explain the more than ten-fold higher arrhythmogenic sensitivity towards light in the endocardium as seen in Fig. 20 and 25.

This two-fold difference also accounts for the possible limitations of using two different methods of light application, such as placement of the catheter and different source-sink ratios between the circular epicardial illumination and the 360° endocardial illumination, as well as the approximation of the endocardial surface area.

Therefore, differences in light application, cell excitability and receptor expression have been excluded, indicating that the higher PVC generation must be an intrinsic feature in the G_s-signaling response in subendocardial cardiomyocytes. The endocardium has been reported as an important factor in arrhythmia generation by several studies[181,182,202]. In these studies, VF was induced in dog hearts by S1S2 stimulation. Lugol ablation of the endocardium increased the threshold of VF induction[202], and in another study, also caused the termination of long-duration VF[181]. Lin et al. furthermore showed that the maintenance of long-duration VF relies on focal activation in the endocardium, specifically in Purkinje fibers, and that endocardial ablation by Lugol solution abolished these focal activations[182].

Purkinje fibers build an abundant network along the endocardial myocytes to facilitate the fast conduction of the excitation from the His-bundle to the working myocardium. More evidence that Purkinje fibers might be essential in VT generation was found in transgenic mice carrying a CPVT mutation in the RyR2 ($RyR2^{R4496C/+}$). Cerrone et al. used endocardial mapping in these mice to show that focal activity in VT originated from the His-Purkinje system[175]. Kang et al. crossed this mouse line with a Purkinje cell reporter mouse line (Contactin-2 (Cntn2)-EGFP) to investigate calcium handling in isolated Purkinje cells compared to ventricular cardiomcyotes[176]. $RyR2^{R4496C/+}$ Purkinje cells displayed more arrhythmic calcium release events than ventricular cardiomyocytes at rest and after Iso stimulation.

However, some studies could not confirm the role of Purkinje cells in VT generation. Myles et al. used local noradrenaline injection into the ventricular wall to induce PVCs. While they identified that injection into the RV, which reached the endocardium, induced more PVCs than injection into the LV, which only reached the mid-myocardium, they saw no difference in PVC occurrence after Lugol ablation, excluding Purkinje cells as the source of the observed PVCs[203]. Blackwell et al. generated a mouse line with a selective Casq2 knockout only in Purkinje cells by Cre-recombinase under the Cntn2 promoter[204]. Selective Casq2 knockout only in Purkinje cells did not induce a CPVT phenotype, but Casq2 knockout only in ventricular cardiomyocytes, with conserved expression in the Purkinje cells, displayed the same phenotype as complete Casq2 -/-. This indicates that aberrant calcium handling in the Purkinje cells is not necessary to induce VT. However, they found that endocardial ablation, as well as Casq2 expression in Purkinje cell-neighboring endocardial ventricular cardiomyocytes, protected against VT. Therefore, the junction between Purkinje cells and endocardial cardiomyocytes might play an important role in the generation of VT.

In conclusion, there is supporting evidence that the endocardium and the Purkinje system are important for PVC triggering by diastolic calcium leak. Moreover, focal activity in the endocardium was also shown to play a role in the maintenance of VF. The mechanisms underlying the increased focal activity, especially regarding G_s-signaling, however, still need to be fully understood. This thesis supports the importance of the endocardium and was able to characterize further the extent of the difference of endocardial cardiomyocytes towards G_s-induced arrhythmia triggers.

4.6 PDE activity does not explain the subendocardial G_s-sensitivity

The G_s-signaling response is tightly regulated in cardiomyocytes. As described in Chapter 1.2.4., PDEs play an essential role in this regulation by degradation of the main second messenger, cAMP. Expression and localization of the different PDE subtypes create cAMP microdomains, which regulate

PKA activation and subsequent phosphorylation in the subcellular compartments of the cardiomyocyte. Especially PDE4D[103], as well as PDE2[205] have previously been indicated to play a role in the generation of VT. Lehnart et al. observed exercise-induced arrhythmias in PDE4D knockout mice[103]. They found an increased leakiness and a hyperphosphorylation of the RyR2 in these mice. They furthermore analyzed heart tissue samples from heart failure patients and found reduced levels of PDE4D3 directly associated with RyR2 compared to non-failing hearts and hyperphosphorylation of RyR2 at S2808. Vettel et al. generated transgenic mice with heart-specific PDE2 expression and saw reduced arrhythmic events and fewer calcium sparks in PDE2 transgenic mice, again indicating a protective role of PDE activity[205]. They did not see a difference in S2808 phosphorylation at the RyR2, but a reduced S2814 phosphorylation, thought to be preferentially CaMKII phosphorylated. They also observed reduced PLN phosphorylation in the PDE2 transgenic mice.

In order to test whether PDE activity might influence the generation of PVCs in the endocardium and epicardium, hearts were perfused with IBMX, an unspecific PDE inhibitor, thus abolishing the effect of a different expression or localization of PDEs. Light dose-response curves of PVCs without IMBX and during perfusion with 1 and 3 µM IMBX were acquired for endocardial and epicardial illumination to quantify the effect of PDE inhibition. Without IBMX, the difference in the endocardium and epicardium was further confirmed with a difference of approx. 25-fold in the light intensity at which the half-maximal effect was reached (Eli50 (0 µM IBMX) endo: 0.2 mW/mm^2, epi: 5 mW/mm^2) (Fig. 25).

More PVCs occurred during IBMX perfusion even without illumination, indicating that under baseline conditions, AC produces cAMP, but PDEs degrade cAMP at a similar rate, thus keeping cAMP concentration low. When PDEs are inhibited, however, cAMP accumulates in the cell and can cause PVCs. To analyze the effect by illumination, the PVC count at baseline was subtracted from the PVC count after illumination. The Eli50 of this corrected dose-response curve shifted from 5 mW/mm^2 at 0 µM IBMX to 2 mW/mm^2 at 3 µM IBMX for the epicardial illumination. For the endocardial illumination, a shift occurred from 0.2 mW/mm^2 at 0 µM IBMX to 0.12 mW/mm^2 at 3 µM IBMX. Consequently, the ELi50 of the epicardial illumination remained 16-fold higher than the endocardial illumination with IBMX. The increase in baseline PVC count and a slight shift in Eli50s indicate that PDEs play a role in the inhibition of PVC generation but are not the deciding differential factor in the subendocardial cardiomyocytes.

However, it has to be noted that IBMX does not inhibit PDE8 and thus PDE8 cannot entirely be excluded as a possible factor, even though the role of PDE8 in VT generation is not well established yet. One study was found, in which cardiomyocytes from PDE8 knockout mice display a stronger increase of calcium transients after Iso stimulation and a higher calcium spark frequency than wildtype cardiomyocytes[106], which may be indicative of diastolic calcium leak from the SR.

4.7 Subendocardial cardiomyocytes have distinct phosphorylation levels of calcium-handling proteins

Endocardial and epicardial cardiomyocytes differ significantly in their electrophysiological properties. Endocardial cardiomyocytes have been described to have a longer APD. Thus, endocardial cardiomyocytes are the first to depolarize but the last to repolarize, resulting in the ECG's positive T-wave. Differences in the expression of voltage-gated potassium channels mainly explain the differences in the action potential. In mice, especially $I_{to,s}$ and $I_{K,slow}$ densities are lower in the endocardium than the epicardium[206]. In canine hearts, lower expression of I_{to} and I_{Ks} have been reported in the endocardium compared to the epicardium[207,208]. The lower I_{to} current in the endocardium than the epicardium has also been found in human cardiomyocytes[209]. The stronger I_{to} in epicardial cardiomyocytes leads to a more prominent phase 1 early depolarization in the epicardial cardiomyocytes. Meanwhile, endocardial cardiomyocytes have a more positive overshoot in the initial phase 0 depolarization[210,211].

Although APD plays a role in EAD generation, it seems unlikely to be the cause of diastolic calcium leak-induced DADs. There are some indications that the endocardium and the epicardium also differ in calcium handling. In mice, endocardial cardiomyocytes have a slower calcium transient upstroke as well as slower decay times than epicardial cardiomyocytes[212]. Longer calcium transients in the endocardium were also found in humans, with a reduction of the transmural difference in heart failure patients[213]. This indicates that there could be differences in the expression or activity of calcium handling proteins, such as Serca2a, PLN and RyR2 at the SR calcium handling side, or LTCC and NXC in regard to calcium flux at the plasma membrane. However, few studies have been performed on the transmural differences in the expression of calcium-handling proteins, which could explain the different calcium responses. Investigations by Xiong et al. have seen mRNA and protein expression differences in NCX in canine hearts, with NCX being less expressed in the endocardium[214]. Laurita et al. also in canine hearts, however, saw no difference in NCX expression[215]. But lower expression of SERCA2a in the endocardium compared to the epicardium was found. This expression difference in SERCA2a was also observed in two studies on human failing hearts and non-failing control hearts. The difference in SERCA2a expression was more pronounced in heart failure than in control hearts due to decreased expression in the endocardium[213,216]. Prestle et al. furthermore saw a slightly, but not significantly, lower expression of PLN in the endocardium, which was also reduced in heart failure[216].

Moreover, the phosphorylation status of calcium-handling proteins changes in heart failure. While RyR2 is hyperphosphorylated, PLN has been found to be less phosphorylated[217,218].

Hyperphosphorylation of RyR2 in heart failure leads to a dissociation of FKBP12.6, which increases the open probability of RyR2 and increases RyR2 sensitivity to cytosolic calcium[219,220].

While cytosolic calcium is an important regulator of the RyR2, the open probability of RyR2 is also increased by an increase in SR calcium. RyR2 phosphorylation at S2808 increases RyR2 luminal calcium sensitivity, which can trigger diastolic calcium leak[73].The SR calcium content is regulated by Serca2a activity and higher Serca2a activity leads to higher SR calcium content. This leads to increased calcium release and transients during diastole and, thus, stronger contraction. Serca2a overexpression has been studied as a potential therapy to increase pump function in heart failure. Most notably, the "Calcium Upregulation by Percutaneous Administration of Gene Therapy in Cardiac Disease" (CUPID) phase 2 clinical study investigated the outcome of adeno-associated viral gene transfer of Serca2a in late-stage heart failure patients. While the first study had promising results on heart function and mortality[221], a more extensive follow-up study (CUPID2) could not confirm this and saw no significant improvement after Serca2a gene transfer compared to the placebo group[222]. The possible negative effect of increased SR calcium content could be an accompanied increase in diastolic calcium leak, a mechanism referred to as store-overload induced calcium release (SOICR). SOICR can be especially prominent when paired with increased RyR2 sensitivity due to mutations or hyperphosphorylation. Nevertheless, neither study (CUPID and CUPID2) noted any increase in cardiac events in the AAV1/Serca2a group.

The role of Serca2a in the generation of VT was further studied in rodent models. Chen et al. saw increased mortality from VT in transgenic rats with Serca2a overexpression after myocardial infarction[223]. Myles et al., moreover, saw a reduction in noradrenaline-induced PVCs by Serca2a inhibition[203]. In contrast, Del Monte et al. showed fewer VT episodes in rats after ischemia/reperfusion when Serca2a was overexpressed by adenoviral gene transfer[224]. Thus, the role of Serca2a activity in the generation of arrhythmias is still controversially discussed.

To analyze if a differential expression of Serca2a or other calcium-handling proteins in the endocardium could explain the endocardial G_s-sensitivity in Casq2 -/- mice, a method to extract endocardial tissue from the LV free wall of mouse hearts has been established in this thesis. Western blot analysis, however, could not reveal significant differences in Serca2a, PLN or RyR2 expression in endocardial versus myocardial tissue (Fig. 26). Therefore, the most important SR calcium-handling proteins were excluded from differential expression. The experiments with IMBX perfusion also indicated that differential PDE or cAMP levels do not play a deciding role. Thus, the next target was the downstream signaling of cAMP by investigating PKA phosphorylation levels. As described above, the phosphorylation status of these SR calcium-handling proteins is an important regulator of calcium release and could explain the difference in response to G_s-stimulation. For this, a global PKA

phosphorylation antibody (RRXS*/T*), which detects all phosphorylated sites at the PKA recognition sequences RRXS or RRXT, was used. Western blots revealed 5 distinct bands of highly phosphorylated proteins (Fig. 27). Band 2 at 120 kDa might be of interest as it showed lower basal phosphorylation but higher iso-stimulated phosphorylation in the endocardium in three mice. The protein responsible for this band is not identified yet. Particularly band 5 at approx. 10 kDa had lower phosphorylation levels in the subendocardial samples at baseline and under Iso stimulation but also had an increased endo/myo phosphorylation ratio upon Iso stimulation (Fig. 28), indicating a stronger response to β-adrenergic activation in the subendocardium. The molecular weight of band 5 fit with the molecular weight of PLN. Western blot of Ser16 phosphorylated PLN confirmed that PLN is significantly lower phosphorylated in subendocardial tissue than in myocardial tissue basally and had a higher increase of phosphorylation in the subendocardial tissue upon Iso stimulation (Fig. 29).

Several factors could influence the baseline phosphorylation level as well as the phosphorylation increase of PLN. Firstly, PLN is known to be mainly dephosphorylated by the phosphatase PP1[107,225]. Thus, higher expression or activity of PP1 in the endocardium could explain lower baseline phosphorylation levels of PLN. PP1 is inhibited by PKA-phosphorylation of inhibitor-1[226] and heat shock protein 20 (Hsp20)[227] upon β-AR stimulation. A stronger inhibition of PP1 by inhibitor-1 or Hsp20 upon PKA stimulation could thus explain the stronger phosphorylation increase (higher endo/myo ratio) during Iso stimulation in the endocardium compared to the mid-myocardium. Another factor that could influence the phosphorylation of PLN is its compartmentalization. PLN builds a macromolecular complex with Serca2a, PKA and AKAP18δ[228]. Differences in AKAP18δ expression or localization could influence the recruitment of PKA to PLN and PKA-dependent phosphorylation of PLN.

The increased phosphorylation of PLN upon Iso stimulation could indicate a stronger increase of Serca2a activity due to the reduced PLN-dependent Serca2a inhibition. This increased Serca2a activity could lead to a higher increase in SR calcium up to a point of SOICR, which then causes the increased PVC inducibility in the endocardial cardiomyocytes (see also discussion above).

4.8 Proarrhythmic potential of APD modulation by G_s-activation

PVCs and triggered VTs were induced by local G_s-stimulation of the endocardium in JellyOp-expressing mice. However, CPVT patients suffer from polymorphic and bidirectional reentry VT, which can cause sudden cardiac death, especially when it devolves into VF. The substrate of a reentry VT is critical for the duration and complexity of the VT. To investigate the role of G_s-signaling on the inducibility by a VT trigger and the duration of reentry VTs in Casq2 -/- JellyOp pos. mice, S1S2 electrical stimulation was applied. When choosing S2 pulse interval close to the baseline S2 capture threshold, illumination

led to non-capture of the S2 pulse within the first approx. 45 s of illumination, followed by recapture even during prolonged illumination (Fig. 30). This indicates that G_s-signaling leads to a transient prolongation of the effective refractory period. This was also confirmed in sharp electrode measurements, which showed an increase in APD60 (Fig. 31). The effect of the G_s-signaling cascade on APD can be due to multiple effector proteins, with I_{CaL} and I_{Ks} as the most prominent ones. Increased I_{CaL} by PKA phosphorylation can prolong APD, while an increase in I_{Ks} current by PKA phosphorylation would decrease APD by enhancing repolarization[229,230]. Whether one or the other effect is stronger might depend on activation rate, frequency as well as on the species. In mice I_{Ks} does not play a prominent role in repolarization, which explains the observed APD prolongation upon G_s-stimulation. But even in species with more prominent I_{Ks}, APD prolongation by G_s-signaling might be an important VT modulator. A mathematical model of rabbit ventricular cardiomyocytes by Xie et al.[177,229] revealed that a fast and strong G_s-activation especially leads to an initial imbalance between I_{CaL} activation and I_{Ks} activation. Specifically, I_{CaL} activation reaches its maximum faster than I_{Ks}, which transiently prolongs the APD, until maximal I_{Ks} activation counteracts the prolongation. This publication further showed that the G_s-induced APD prolongation, when it occurs during reentry VT, can lead to wave break and transition from monomorphic VT to VF.

In the physiological G_s-response the increase in beating frequency due to sinus node stimulation is faster than phosphorylation as it is directly affected by the effect of cAMP on HCN4 channels. Increased beating frequency leads to a rate-dependent reduction in APD[231]. Thus, an increase in beating frequency can potentially mask the effect of I_{CaL} / I_{Ks} imbalance. However, CPVT patients often present with bradycardia and an impaired chronotropic response to G_s-stimulation[192,193]. An impaired chronotropic response of the heart rate results in a lower increase in heart rate during β-AR stimulation. A smaller heart rate response would also lead to less chronotropic APD shortening. Therefore, the transient APD increase by I_{CaL} phosphorylation might potentially play a more important role in APD regulation in CPVT patients with impaired chronotropic response. It could in combination with the increased PVC occurrence after G_s-activation increase the probability of R-on-T PVCs, which can trigger fatal VTs.

4.9 G_s-signaling increases VT incidence upon premature trigger through inhomogeneous conduction

Due to the transient prolongation of the APD after G_s-stimulation, S2 intervals had to be increased to ensure S2 capture throughout the experiment, which is a prerequisite to analyze the VT inducibility. Therefore, S1S2 electrical stimulation protocols with S2 pulses 5 ms above the refractory threshold

were performed. Illumination of Casq2 -/- JellyOp pos. hearts led to a significantly increased VT incidence compared to Casq2 +/+ JellyOp pos. and Casq2 -/- JellyOp neg. mice and affected VT maintenance with increased incidence of VT with longer duration (≥ 300 ms). As discussed in Chapter 1.1.5, a functional reentry depends on the electrophysiological properties of the tissue favoring the generation and propagation of a spiral wave. A short wavelength, which is the result of a short action potential and a slow conduction velocity, is an important factor in the propagation of a spiral wave[43]. Moreover, heterogenous APD and conduction velocity throughout the tissue increase the likelihood for the generation of a spiral wave.

To investigate the underlying mechanism of the VT induction, voltage mapping of a S1S2-induced reentry VT in a JellyOp pos. mouse before and after illumination was performed. The S2 pulse showed a clear decrease in conduction velocity compared to S1 under baseline conditions. This can be explained by reduced sodium channel availability with lower I_{Na} upon S2 stimulation due to incomplete repolarization. After illumination the conduction velocity changes. While G_s-activation seems to increase conduction velocity in S1, the conduction of the S2 pulse appears to be modulated very heterogeneously. One area specifically in the RV of the imaged heart had a strong increase of conduction velocity, while the immediately neighboring, more remote area developed a conduction block. This could be a functional conduction block caused by the preceding fast conduction wave, which then encounters refractory tissue, which has not recovered enough to be excited by the incoming wave. Since other areas conduct at a slower velocity, the wave still propagates and can rotate around the functional conduction block, thereby creating a substrate for a reentry VT.

Zykov et al. showed in a mathematical model that regions with relatively fast propagation in tissue with slower conduction in other parts can induce a spiral wave[232]. This is due to a steep mismatch in cell-coupling, which generates a unidirectional conduction block. The fast-conducting region has a high coupling between cells allowing the fast conduction. This, however, also means that, in the unexcited state, this tissue represents a strong electrical sink. If the excitation wave arrives from a region with much slower conduction and thus less cell-coupling, the sink of the well-coupled tissue can be too high for the arriving source of the wave front to reach the threshold for excitation, which stops the transmission of the excitation. Suppose the tissue is heterogenous in coupling with some regions displaying a gradient of coupling that can overcome the source-sink mismatch and other regions with very high source-sink mismatch. In that case, this can result in asymmetrical conduction and lead to the generation of a rotor.

Multiple factors determine the conduction velocity of the tissue. As mentioned upstroke velocity of the action potential created by I_{Na} is one major determinant. The other factor is intercellular coupling via gap junctions, mostly located at the intercalated disks.

I_{Na} is affected by G_s-signaling as $Na_v1.5$ can be phosphorylated by PKA, which increases sodium current and action potential upstroke velocity[233]. Cx43 and Cx40 can also be phosphorylated by PKA, although Cx43 appears to be a poor substrate[234]. While Cx40 phosphorylation enhances channel conductance[235], the effect on Cx43 is less clear. Studies report a more indirect mechanism of PKA-mediated increase of cell conduction by enhanced channel trafficking to the membrane and channel assembly[235–237]. The stronger effect of the conduction velocity by G_s-activation on the S2 pulse compared to the S1 pulse further indicates a more prominent role of G_s-activation on the I_{Na} than gap junctions, as I_{Na} is more influenced by the repolarization state of the cells than gap junction conductance.

In conclusion, a heterogeneity of conduction velocity upon illumination was observed (Fig. 33), which led to a reentry VT. To explain the underlying mechanisms further studies on the influence of G_s-effects on I_{Na} compared to gap junctions and on the conduction velocity in the different areas of the heart have to be performed. A difference in expression levels of $Na_v1.5$ and Cx43 in different regions of the heart or a heterogenous response to G_s-stimulation could lead to well-coupled regions with fast conduction neighboring regions with lower coupling. This would provide a substrate for the generation and propagation of reentry VTs.

4.10 G_s-signaling exacerbates reentry VT complexity

Further influence of G_s-signaling on the complexity of the VT could not be determined in the set of experiments discussed above because the VTs overall were too short, with the majority being shorter than 300 ms. Therefore, hearts were perfused with pinacidil in the subsequent experiments to activate K_{ATP} channels. This reduces APD and the wavelength of the VT to be able to generate long-running, stable monomorphic VT even in small mouse hearts[159]. Illumination of the anterior ventricular walls during a VT decreased VT frequency significantly (Fig. 34A,B). The shift in VT frequency from an average 19.8 Hz to 18.1 Hz corresponds to a shift in cycle length from 50.5 ms to 55.2 ms. This increase in cycle length thus correlates with the previously observed increase in APD upon illumination of approx. 5 ms. The decrease in frequency of the VT can destabilize the rotor due to an increase of the wavelength. This could promote wave break, when the head of the wave encroaches on the tail, and lead to destabilization of the rotor.

Accordingly, in three experiments, the morphology of the VT shifted from a monomorphic to a polymorphic VT after an initial frequency reduction. In these cases, voltage mapping revealed the transition from a stable, stationary rotor to an unstable, meandering rotor (Fig. 34C-E). Moreover, in one case the dominant frequency doubled specifically in the RV. In combination with the previously discussed prolongation of APD upon illumination measured by sharp electrode, this depicts an

experimental affirmation of the mathematical model by Xie et al., which predicted a transition to VF after G_s-induced APD prolongation[177].

To further investigate the differential response in the RV and LV, local ECG recordings were generated during ventricle-specific illumination. ECG recordings were used in favor of voltage mapping because voltage mapping is limited to show only the effect in the first epicardial layers and only the anterior wall. ECG recordings can give an overall impression of the complexity throughout the whole ventricular wall. Local illumination of the anterior walls of the RV and the LV with simultaneous local ECG recordings revealed distinct shifts of the morphology of the ECG signals in the illuminated areas, with the RV exhibiting higher complexity in the ECG morphology (Fig. 35). FFT amplitude of the ECG signals consisted of a stable single frequency with its harmonics before illumination. After illumination, multiple other frequencies emerged (Fig. 36). While the single, stable frequency indicates a stable rotor within the ventricles driving the VT, multiple frequencies indicate the emergence of multiple rotors typical for polymorphic VT and VF. Unstable, high-frequency rotors especially characterize VF. Therefore, an analysis of the variability of the high-frequency component of the FFT was performed (Fig. 37). This revealed that RV-specific illumination significantly increased the variability of the high-frequency component in both ventricles. LV-specific illumination did not significantly alter the variability.

Differences in electrophysiological properties between the LV and the RV have been reported across species. The APD of the RV is shorter than the LV, which can be explained by larger repolarizing potassium currents. Increased currents in the RV have been reported for I_{to} (in mouse and dog) and I_{Ks} (in human and dog)[238,239]. Moreover, higher expression of $I_{K,ATP}$ has been reported in rabbit[240]. Regarding the I_{KATP} expression, the effect of pinacidil used in this thesis (Fig. 34-37), thus, might have been stronger in the RV due to higher expression of I_{KATP}.

Interestingly, Molina et al. showed that cardiomyocytes isolated from dog RV had a stronger response to β-AR stimulation by Iso than LV cardiomyocytes, which was measured by increased sarcomere shortening and calcium transient increase[241]. This further correlated with a higher increase of cytosolic cAMP concentration. Inhibition of PDE3 and PDE4 showed that the LV response was more sensitive to PDE3 inhibition, while the RV response was more regulated by PDE4 inhibition, indicating an interventricular difference in PDE activity.

The shorter APD in the RV than the LV could lead to a higher propensity of the RV towards higher frequency rotors due to a shorter wavelength. A stronger response to β-AR stimulation in the RV than the LV could further enhance the likelihood of high-frequency rotors, e.g., by further reduction of the wavelength by an increase of conduction velocity, especially at high frequencies as observed in the S2

pulse after illumination (Fig. 33). In Fig. 33 it was also shown that the increase in conduction velocity of the S2 pulse in the RV can lead to conduction block, which in a stable-running VT could induce wave break, which transitions a monomorphic to a polymorphic VT.

Another possible reason for the higher tendency towards increased complexity and doubling of the dominant frequency in the RV could be the much thinner ventricular wall of the RV compared to the LV, leading to a more transmural G_s-activation of the RV when both ventricles are illuminated with the same light intensity. G_s-activation in the LV only penetrates into the first epicardial layers of the ventricular wall and thus the LV could be more resistant to epicardial illumination-induced increase in VT complexity. This might also indicate that the endocardium might not only play a role in the triggering of the VT but also its stability. This thesis showed that the endocardium is prone to the generation of ectopic beats. These extrabeats may also occur during a VT, which could destabilize the rotor, leading to wave breaks due to the local stimulations interfering with the rotor propagation. Cerrone et al. found that focal activity during VT originated in the endocardium in CPVT mice[175]. Lin et al. also observed focal activity in the endocardium during ventricular fibrillation in dogs and that abolishing this focal activity by ablation of the endocardium shortens the duration of VF[182]. A similar mechanism could lead to the switch in complexity during RV illumination by focal endocardial activity disturbing the stability of the rotor and leading to a switch to higher frequency rotors or wavelets with multiple focal points.

4.11 Study limitations

The mouse as a model organism for ventricular arrhythmias has some important limitations. One factor is the size difference between human and mouse hearts. The small size of the mouse heart normally prevents long-running reentry VT, as observed in humans and other larger mammals. This can also be seen as an advantage in certain experimental settings, because the short-running, self-terminating VTs in the mouse heart make it possible to repeatedly observe the initiation of the VT, as was done in this study by S1S2 stimulation. Moreover, shortening of the APD by the K_{ATP} channel activator pinacidil shortens the wavelength so that stable-running VT can also be investigated in mouse hearts.

In addition, there are also key differences in ion channel expression, such as repolarizing potassium channels, as well as calcium handling between species. The high dependence of the mouse cardiomyocyte on SR calcium release in the generation of the calcium transient following an action potential, however, makes it a good model for studying SR calcium leak-induced arrhythmias. Moreover, the mouse has been the model organism of choice for the majority of studies on a number

of hereditary ventricular arrhythmias, due to the wide availability of transgenic mouse models, the handling and the relative similarity to the human heart.

The second limitation of the study is the use of an exogenous receptor for the activation of G_s-signaling. Even though the optogenetic activation of JellyOp grants many advantages over traditional pharmacological approaches, it still has to be considered that localization, expression levels and downstream signaling of JellyOp might differ from that of endogenous β-ARs. To mitigate these concerns, JellyOp activation has been compared to the activation of β-ARs by iso, in which similar responses were found. Moreover, immunostaining of JellyOp heart slices revealed expression on the cytoplasmic membrane as well as the t-tubule system[160], which indicates similar distribution of the receptor to β1-ARs. Even still, differences in downstream signaling and receptor activation as well as β-arrestin recruitment and desensitization compared to endogenous β-AR cannot be excluded entirely.

JellyOp activation by light also removes the influence of sympathetic innervation density on the response of different heart regions on sympathetic activation. This can be seen as a limitation of the model, however, it could also serve as a chance to be able to simulate innervation changes and heterogeneities observed in heart disease by choosing specific patterns of heterogenous illumination intensities.

4.12 Future perspectives

This thesis strongly implicates the innermost subendocardial cardiomyocytes as the source of G_s-induced VTs. Furthermore, protein analysis uncovered a possible mechanism for the increased VT sensitivity in the endocardium by investigating the PKA-mediated phosphorylation status and depicting that endocardial tissue has distinct phosphorylation characteristics compared to mid-myocardial tissue under basal as well as β-AR stimulated conditions. PLN has subsequently been uncovered as a differentially phosphorylated protein, with lower basal phosphorylation in the subendocardium, but higher relative phosphorylation increase upon β-AR stimulation. A number of other proteins were differentially phosphorylated in western blots using an antibody against the phosphorylated PKA recognition site RRXS*/T*. To identify these proteins and potential other targets, the endocardial tissue collection protocol established in this thesis can be used to perform further analyses on the proteome as well as the phosphoproteome to reveal the identity of the differentially PKA phosphorylated proteins, but also to potentially unveil further phosphorylation differences, e.g. of CamKII phosphorylated proteins. Moreover, it was out of the scope of this thesis to further research the cause of differential phosphorylation. Potentially interesting targets for future studies could be

phosphatases. Especially PP1 and its regulators, such as inhibitor-1, are known to dephosphorylate PLN and thus could be interesting targets to study in the future.

In regard to the high sensitivity to G_s-induced arrhythmias of the endocardium, it would be desirable to investigate further the role of the conduction system and, in particular, the Purkinje cells, as they have been implicated to have increased arrhythmogenic potential previously[176]. To investigate whether it is sufficient to activate G_s-signaling in Purkinje cells or whether the surrounding working myocardium is necessary for the generation of the VT trigger, a mouse line with conduction system-specific JellyOp expression under the Cx40 promotor[242] should be established next.

Regarding the modulation of VT complexity, further investigation of the mechanism behind the heterogenous modulation of the conduction velocity could be of future interest. Here, Nav1.5 and Cx43 are interesting targets. It would furthermore be insightful to perform these experiments under pathological conditions, such as in a heart failure model or after myocardial infarction to see whether the heterogenous conduction velocity is exacerbated in these conditions. Thereby, the difference between light-induced G_s-receptor activation and direct activation of the endogenous sympathetic innervation can be additionally compared.

5 Summary

Ventricular arrhythmias are one of the major causes of death worldwide, occurring especially in structurally remodeled hearts, but also in hereditary conditions, such as CPVT, in which mutations in RyR2 or Casq2 cause diastolic calcium leak. In this thesis optogenetic activation of the G_s-signaling pathway was used to investigate regionally specific effects of β-adrenergic stimulation on ventricular arrhythmias, which could in the future lead to the development of more selective drug treatments with increased efficacy and reduced adverse effects.

In mice expressing the blue light sensitive GPCR JellyOp and carrying a Casq2 knockout (Casq2 -/- JellyOp pos.) the influence of the regional sensitivity towards diastolic calcium leak induced VT trigger by G_s-signaling was investigated. The local stimulation of the endocardium and the epicardium with matching light intensities and area of illumination uncovered a more than ten-fold higher propensity for G_s-induced PVCs in the endocardium than the epicardium. High intrinsic sinus rhythm as well as fast ventricular pacing protected against G_s-induced PVCs. Pacing threshold in ChR2 expressing mice as well as quantitative analysis of JellyOp expression excluded differences in light application, receptor expression as well as excitability of the cardiomyocytes and thereby confirmed an inherent difference in the G_s-signaling response of the endocardium. PDE inhibition by IBMX did not abolish the endo- to epicardial difference, thus suggesting a regulatory mechanism downstream of cAMP. Western blot analysis of calcium handling proteins as well as PKA phosphorylation revealed a significant difference in phosphorylation levels of PKA phosphorylated proteins, and in particular PLN phosphorylation, with a higher relative increase in phosphorylation in the endocardium than the mid-myocardium upon adrenergic stimulation.

Inducibility of reentry VTs was characterized using S1S2 electrical stimulation to generate a premature trigger during the vulnerable repolarization phase of the ventricle. Casq2 -/- JellyOp pos. hearts had significantly higher VT incidence after optogenetic G_s-stimulation. Voltage mapping of a S1S2 triggered excitation revealed increased conduction velocity heterogeneity and local, functional conduction block after illumination. In long-running monomorphic VTs, illumination significantly decreased VT frequency and in some cases led to the transition to a polymorphic VT with higher complexity of the ECG signal and destabilization of the rotor core observed in voltage mapping.

In conclusion, optogenetic G_s-activation enabled regional discrimination of β-adrenergic effects on ventricular arrhythmias, revealing that G_s-activation promotes VT trigger by generation of PVCs in the endocardium. Furthermore, optogenetic G_s-activation enhanced inducibility and maintenance of reentry VT and increased the risk of transition to higher frequency and complexity as observed in the

transition to highly lethal VF in patients. In the future, identification of the new endocardial mechanism will help to develop concepts to prevent PVCs triggering VT.

6 References

1. Speckmann, E. J., Hescheler, J. & Köhling, R. *Physiologie, 5. Auflage*. (2008).

2. Stieber, J. *et al.* The hyperpolarization-activated channel HCN4 is required for the generation of pacemaker action potentials in the embryonic heart. *Proc. Natl. Acad. Sci. U. S. A.* **100**, 15235–15240 (2003).

3. Hund, T. J., Smith, S. A., Makara, M. A. & Mohler, P. J. Chapter 7 - Cellular and Molecular Pathobiology of the Cardiac Conduction System. in *Cellular and Molecular Pathobiology of Cardiovascular Disease* (eds. Willis, M. S., Homeister, J. W. & Stone, J. R.) 121–134 (Academic Press, 2014). doi:10.1016/B978-0-12-405206-2.00007-7.

4. Klabunde, R. E. Cardiac electrophysiology: normal and ischemic ionic currents and the ECG. *Adv. Physiol. Educ.* **41**, 29–37 (2017).

5. Monfredi, O., Dobrzynski, H., Mondal, T., Boyett, M. R. & Morris, G. M. The Anatomy and Physiology of the Sinoatrial Node—A Contemporary Review. *Pacing Clin. Electrophysiol.* **33**, 1392–1406 (2010).

6. Kus, T. & Sasyniuk, B. I. Electrophysiological actions of disopyramide phosphate on canine ventricular muscle and purkinje fibers. *Circ. Res.* **37**, 844–854 (1975).

7. Nichols, C. g., Makhina, E. n., Pearson, W. l., Sha, Q. & Lopatin, A. n. Inward Rectification and Implications for Cardiac Excitability. *Circ. Res.* **78**, 1–7 (1996).

8. Verheule, S. & Kaese, S. Connexin diversity in the heart: insights from transgenic mouse models. *Front. Pharmacol.* **4**, (2013).

9. Cohen, S. A. & Barchi, R. L. Cardiac sodium channel structure and function. *Trends Cardiovasc. Med.* **2**, 133–140 (1992).

10. Gellens, M. E. *et al.* Primary structure and functional expression of the human cardiac tetrodotoxin-insensitive voltage-dependent sodium channel. *Proc. Natl. Acad. Sci.* **89**, 554–558 (1992).

11. Bondarenko, V. E., Szigeti, G. P., Bett, G. C. L., Kim, S.-J. & Rasmusson, R. L. Computer model of action potential of mouse ventricular myocytes. *Am. J. Physiol.-Heart Circ. Physiol.* **287**, H1378–H1403 (2004).

12. Lopatin, A. N., Makhina, E. N. & Nichols, C. G. The mechanism of inward rectification of potassium channels: 'long-pore plugging' by cytoplasmic polyamines. *J. Gen. Physiol.* **106**, 923–955 (1995).

13. Benitah, J.-P., Alvarez, J. L. & Gómez, A. M. L-type Ca(2+) current in ventricular cardiomyocytes. *J. Mol. Cell. Cardiol.* **48**, 26–36 (2010).

14. Chen, L. Q., Santarelli, V., Horn, R. & Kallen, R. G. A unique role for the S4 segment of domain 4 in the inactivation of sodium channels. *J. Gen. Physiol.* **108**, 549–556 (1996).

15. Kaese, S. & Verheule, S. Cardiac electrophysiology in mice: a matter of size. *Front. Physiol.* **3**, (2012).

16. Oudit, G. Y. *et al.* The Molecular Physiology of the Cardiac Transient Outward Potassium Current (Ito) in Normal and Diseased Myocardium. *J. Mol. Cell. Cardiol.* **33**, 851–872 (2001).

17. Li, G.-R., Feng, J., Yue, L., Carrier, M. & Nattel, S. Evidence for Two Components of Delayed Rectifier K+ Current in Human Ventricular Myocytes. *Circ. Res.* **78**, 689–696 (1996).

18. Nerbonne, J. M. Molecular basis of functional voltage-gated K+ channel diversity in the mammalian myocardium. *J. Physiol.* **525**, 285–298 (2000).

19. Fiset, C., Clark, R. B., Larsen, T. S. & Giles, W. R. A rapidly activating sustained K+ current modulates repolarization and excitation–contraction coupling in adult mouse ventricle. *J. Physiol.* **504**, 557–563 (1997).

20. Zhou, J., Jeron, A., London, B., Han, X. & Koren, G. Characterization of a slowly inactivating outward current in adult mouse ventricular myocytes. *Circ. Res.* **83**, 806–814 (1998).

21. Joukar, S. A comparative review on heart ion channels, action potentials and electrocardiogram in rodents and human: extrapolation of experimental insights to clinic. *Lab. Anim. Res.* **37**, 25 (2021).

22. Gettes, L. S., Morehouse, N. & Surawicz, B. Effect of Premature Depolarization on the Duration of Action Potentials in Purkinje and Ventricular Fibers of the Moderator Band of the Pig Heart: ROLE OF PROXIMITY AND THE DURATION OF THE PRECEDING ACTION POTENTIAL. *Circ. Res.* **30**, 55–66 (1972).

23. Knollmann, B. C., Schober, T., Petersen, A. O., Sirenko, S. G. & Franz, M. R. Action potential characterization in intact mouse heart: steady-state cycle length dependence and electrical restitution. *Am. J. Physiol.-Heart Circ. Physiol.* **292**, H614–H621 (2007).

24. Nerbonne, J. M. & Kass, R. S. Molecular Physiology of Cardiac Repolarization. *Physiol. Rev.* **85**, 1205–1253 (2005).

25. Bers, D. M. Cardiac excitation–contraction coupling. *Nature* **415**, 198–205 (2002).

26. Scriven, D. R. L., Asghari, P., Schulson, M. N. & Moore, E. D. W. Analysis of Cav1.2 and Ryanodine Receptor Clusters in Rat Ventricular Myocytes. *Biophys. J.* **99**, 3923–3929 (2010).

27. Scriven, D. R., Dan, P. & Moore, E. D. Distribution of proteins implicated in excitation-contraction coupling in rat ventricular myocytes. *Biophys. J.* **79**, 2682–2691 (2000).

28. Scriven, D. R. L., Asghari, P. & Moore, E. D. W. Microarchitecture of the dyad. *Cardiovasc. Res.* **98**, 169–176 (2013).

29. Györke, S., Stevens, S. C. W. & Terentyev, D. Cardiac calsequestrin: quest inside the SR. *J. Physiol.* **587**, 3091–3094 (2009).

30. Mezu, U. L. *et al.* Accelerated Junctional Rhythm and Nonalternans Repolarization Lability Precede Ventricular Tachycardia in *Casq2* −/− Mice. *J. Cardiovasc. Electrophysiol.* **23**, 1355–1363 (2012).

31. Antzelevitch, C. & Burashnikov, A. Overview of Basic Mechanisms of Cardiac Arrhythmia. *Card. Electrophysiol. Clin.* **3**, 23–45 (2011).

32. Wang, Q. *et al.* SCN5A mutations associated with an inherited cardiac arrhythmia, long QT syndrome. *Cell* **80**, 805–811 (1995).

33. January, C. T. & Riddle, J. M. Early afterdepolarizations: mechanism of induction and block. A role for L-type Ca2+ current. *Circ. Res.* **64**, 977–990 (1989).

34. Marban, E., Robinson, S. W. & Wier, W. G. Mechanisms of arrhythmogenic delayed and early afterdepolarizations in ferret ventricular muscle. *J. Clin. Invest.* **78**, 1185–1192 (1986).

35. Schlotthauer, K. & Bers, D. M. Sarcoplasmic Reticulum Ca^{2+} Release Causes Myocyte Depolarization: Underlying Mechanism and Threshold for Triggered Action Potentials. *Circ. Res.* **87**, 774–780 (2000).

36. Cheng, H., Lederer, W. & Cannell, M. Calcium sparks: elementary events underlying excitation-contraction coupling in heart muscle. *Science* **262**, 740–744 (1993).

37. Capogrossi, M. C., Houser, S. R., Bahinski, A. & Lakatta, E. G. Synchronous occurrence of spontaneous localized calcium release from the sarcoplasmic reticulum generates action potentials in rat cardiac ventricular myocytes at normal resting membrane potential. *Circ. Res.* **61**, 498–503 (1987).

38. Xie, Y., Sato, D., Garfinkel, A., Qu, Z. & Weiss, J. N. So Little Source, So Much Sink: Requirements for Afterdepolarizations to Propagate in Tissue. *Biophys. J.* **99**, 1408–1415 (2010).

39. Rohr, S. Role of gap junctions in the propagation of the cardiac action potential. *Cardiovasc. Res.* **62**, 309–322 (2004).

40. King, J., Huang, C. & Fraser, J. Determinants of myocardial conduction velocity: implications for arrhythmogenesis. *Front. Physiol.* **4**, 154 (2013).

41. Faber, G. M., Silva, J., Livshitz, L. & Rudy, Y. Kinetic Properties of the Cardiac L-Type Ca2+ Channel and Its Role in Myocyte Electrophysiology: A Theoretical Investigation. *Biophys. J.* **92**, 1522–1543 (2007).

42. Allessie, M. A., Bonke, F. I. & Schopman, F. J. Circus movement in rabbit atrial muscle as a mechanism of tachycardia. III. The 'leading circle' concept: a new model of circus movement in cardiac tissue without the involvement of an anatomical obstacle. *Circ. Res.* **41**, 9–18 (1977).

43. Pandit, S. V. & Jalife, J. Rotors and the Dynamics of Cardiac Fibrillation. *Circ. Res.* **112**, 849–862 (2013).

44. Jalife, J. Inward rectifier potassium channels control rotor frequency in ventricular fibrillation. *Heart Rhythm* **6**, S44–S48 (2009).

45. Winfree, A. T. Electrical instability in cardiac muscle: Phase singularities and rotors. *J. Theor. Biol.* **138**, 353–405 (1989).

46. Baher, A. A. *et al.* Bidirectional ventricular tachycardia: Ping pong in the His–Purkinje system. *Heart Rhythm* **8**, 599–605 (2011).

47. Jalife, J. Ventricular Fibrillation: Mechanisms of Initiation and Maintenance. *Annu. Rev. Physiol.* **62**, 25–50 (2000).

48. Chen, J., Mandapati, R., Berenfeld, O., Skanes, A. C. & Jalife, J. High-Frequency Periodic Sources Underlie Ventricular Fibrillation in the Isolated Rabbit Heart. *Circ. Res.* **86**, 86–93 (2000).

49. Yousuf, O., Chrispin, J., Tomaselli, G. F. & Berger, R. D. Clinical management and prevention of sudden cardiac death. *Circ. Res.* **116**, 2020–2040 (2015).

50. King, G. S., Goyal, A., Grigorova, Y. & Hashmi, M. F. Antiarrhythmic Medications. in *StatPearls* (StatPearls Publishing, 2022).

51. Cardiac Arrhythmia Suppression Trial (CAST) Investigators. Preliminary report: effect of encainide and flecainide on mortality in a randomized trial of arrhythmia suppression after myocardial infarction. *N. Engl. J. Med.* **321**, 406–412 (1989).

52. The Cardiac Insufficiency Bisoprolol Study II (CIBIS-II): a randomised trial. *Lancet Lond. Engl.* **353**, 9–13 (1999).

53. MERIT-HF Study Group. Effect of metoprolol CR/XL in chronic heart failure: Metoprolol CR/XL Randomised Intervention Trial in-Congestive Heart Failure (MERIT-HF). *The Lancet* **353**, 2001–2007 (1999).

54. Norwegian Multicenter Study Group. Timolol-induced reduction in mortality and reinfarction in patients surviving acute myocardial infarction. *N. Engl. J. Med.* **304**, 801–807 (1981).

55. A randomized trial of propranolol in patients with acute myocardial infarction. I. Mortality results. *JAMA* **247**, 1707–1714 (1982).

56. Kuck, K. H., Cappato, R., Siebels, J. & Rüppel, R. Randomized comparison of antiarrhythmic drug therapy with implantable defibrillators in patients resuscitated from cardiac arrest : the Cardiac Arrest Study Hamburg (CASH). *Circulation* **102**, 748–754 (2000).

57. Antiarrhythmics versus Implantable Defibrillators (AVID) Investigators. A comparison of antiarrhythmic-drug therapy with implantable defibrillators in patients resuscitated from near-fatal ventricular arrhythmias. *N. Engl. J. Med.* **337**, 1576–1583 (1997).

58. Lei, M., Wu, L., Terrar, D. A. & Huang, C. L.-H. Modernized Classification of Cardiac Antiarrhythmic Drugs. *Circulation* **138**, 1879–1896 (2018).

59. Dhein, S., van Koppen, C. J. & Brodde, O.-E. Muscarinic receptors in the Mammalian Heart. *Pharmacol. Res.* **44**, 161–182 (2001).

60. Jansen, A. S. P., Van Nguyen, X., Karpitskiy, V., Mettenleiter, T. C. & Loewy, A. D. Central Command Neurons of the Sympathetic Nervous System: Basis of the Fight-or-Flight Response. *Science* **270**, 644–646 (1995).

61. Vincentz, J. W., Rubart, M. & Firulli, A. B. Ontogeny of Cardiac Sympathetic Innervation and Its Implications for Cardiac Disease. *Pediatr. Cardiol.* **33**, 923–928 (2012).

62. Ieda, M. & Fukuda, K. Cardiac Innervation and Sudden Cardiac Death. *Curr. Cardiol. Rev.* **5**, 289–295 (2009).

63. Ieda, M. *et al.* Sema3a maintains normal heart rhythm through sympathetic innervation patterning. *Nat. Med.* **13**, 604–612 (2007).

64. Di Bona, A., Vita, V., Costantini, I. & Zaglia, T. Towards a clearer view of sympathetic innervation of cardiac and skeletal muscles. *Prog. Biophys. Mol. Biol.* **154**, 80–93 (2020).

65. Prando, V. *et al.* Dynamics of neuro-effector coupling at 'cardiac sympathetic' synapses. 51.

66. Shcherbakova, O. G. *et al.* Organization of beta-adrenoceptor signaling compartments by sympathetic innervation of cardiac myocytes. *J. Cell Biol.* **176**, 521–533 (2007).

67. Esler, M. *et al.* Overflow of catecholamine neurotransmitters to the circulation: source, fate, and functions. *Physiol. Rev.* **70**, 963–985 (1990).

68. Graham, R. M., Perez, D. M., Hwa, J. & Piascik, M. T. α1-Adrenergic Receptor Subtypes. *Circ. Res.* **78**, 737–749 (1996).

69. Weis, W. I. & Kobilka, B. K. The Molecular Basis of G Protein–Coupled Receptor Activation. *Annu. Rev. Biochem.* **87**, 897–919 (2018).

70. Defer, N., Best-Belpomme, M. & Hanoune, J. Tissue specificity and physiological relevance of various isoforms of adenylyl cyclase. *Am. J. Physiol. Renal Physiol.* **279**, F400-416 (2000).

71. Kamp, T. J. & Hell, J. W. Regulation of Cardiac L-Type Calcium Channels by Protein Kinase A and Protein Kinase C. *Circ. Res.* **87**, 1095–1102 (2000).

72. Carter, S., Colyer, J. & Sitsapesan, R. Maximum Phosphorylation of the Cardiac Ryanodine Receptor at Serine-2809 by Protein Kinase A Produces Unique Modifications to Channel Gating and Conductance Not Observed at Lower Levels of Phosphorylation. *Circ. Res.* **98**, 1506–1513 (2006).

73. Ullrich, N. D., Valdivia, H. H. & Niggli, E. PKA phosphorylation of cardiac ryanodine receptor modulates SR luminal Ca2+ sensitivity. *J. Mol. Cell. Cardiol.* **53**, 33–42 (2012).

74. James, P., Inui, M., Tada, M., Chiesi, M. & Carafoli, E. Nature and site of phospholamban regulation of the Ca2+ pump of sarcoplasmic reticulum. *Nature* **342**, 90–92 (1989).

75. Li, L., Desantiago, J., Chu, G., Kranias, E. G. & Bers, D. M. Phosphorylation of phospholamban and troponin I in β-adrenergic-induced acceleration of cardiac relaxation. *Am. J. Physiol.-Heart Circ. Physiol.* **278**, H769–H779 (2000).

76. Rao, V. *et al.* PKA Phosphorylation of Cardiac Troponin I Modulates Activation and Relaxation Kinetics of Ventricular Myofibrils. *Biophys. J.* **107**, 1196–1204 (2014).

77. Grimm, M. & Brown, J. H. β-Adrenergic receptor signaling in the heart: Role of CaMKII. *J. Mol. Cell. Cardiol.* **48**, 322–330 (2010).

78. Ferrero, P. *et al.* Ca2+/calmodulin kinase II increases ryanodine binding and Ca2+-induced sarcoplasmic reticulum Ca2+ release kinetics during β-adrenergic stimulation. *J. Mol. Cell. Cardiol.* **43**, 281–291 (2007).

79. Nikolaev, V. O. *et al.* b2-Adrenergic Receptor Redistribution in Heart Failure Changes cAMP Compartmentation. **327**, 6 (2010).

80. Nikolaev, V. O., Bünemann, M., Schmitteckert, E., Lohse, M. J. & Engelhardt, S. Cyclic AMP Imaging in Adult Cardiac Myocytes Reveals Far-Reaching β_1-Adrenergic but Locally Confined β_2-Adrenergic Receptor–Mediated Signaling. *Circ. Res.* **99**, 1084–1091 (2006).

81. Rybin, V. O., Xu, X., Lisanti, M. P. & Steinberg, S. F. Differential Targeting of β-Adrenergic Receptor Subtypes and Adenylyl Cyclase to Cardiomyocyte Caveolae: A MECHANISM TO FUNCTIONALLY REGULATE THE cAMP SIGNALING PATHWAY. *J. Biol. Chem.* **275**, 41447–41457 (2000).

82. Bhogal, N., Hasan, A. & Gorelik, J. The Development of Compartmentation of cAMP Signaling in Cardiomyocytes: The Role of T-Tubules and Caveolae Microdomains. *J. Cardiovasc. Dev. Dis.* **5**, 25 (2018).

83. MacDougall, D. A. *et al.* Caveolae compartmentalise β2-adrenoceptor signals by curtailing cAMP production and maintaining phosphatase activity in the sarcoplasmic reticulum of the adult ventricular myocyte. *J. Mol. Cell. Cardiol.* **52**, 388–400 (2012).

84. Xiao, R. P. *et al.* Beta 2-adrenergic receptor-stimulated increase in cAMP in rat heart cells is not coupled to changes in Ca2+ dynamics, contractility, or phospholamban phosphorylation. *J. Biol. Chem.* **269**, 19151–19156 (1994).

85. Best, J. M. & Kamp, T. J. Different Subcellular Populations of L-type Ca2+ Channels Exhibit Unique Regulation and Functional Roles in Cardiomyocytes. *J. Mol. Cell. Cardiol.* **52**, 376–387 (2012).

86. Balijepalli, R. C., Foell, J. D., Hall, D. D., Hell, J. W. & Kamp, T. J. Localization of cardiac L-type Ca(2+) channels to a caveolar macromolecular signaling complex is required for beta(2)-adrenergic regulation. *Proc. Natl. Acad. Sci. U. S. A.* **103**, 7500–7505 (2006).

87. Cahill, T. J. *et al.* Distinct conformations of GPCR–β-arrestin complexes mediate desensitization, signaling, and endocytosis. *Proc. Natl. Acad. Sci.* **114**, 2562–2567 (2017).

88. Daaka, Y., Luttrell, L. M. & Lefkowitz, R. J. Switching of the coupling of the beta2-adrenergic receptor to different G proteins by protein kinase A. *Nature* **390**, 88–91 (1997).

89. Richter, W. *et al.* Signaling from β1- and β2-adrenergic receptors is defined by differential interactions with PDE4. *EMBO J.* **27**, 384–393 (2008).

90. Perry, S. J. *et al.* Targeting of Cyclic AMP Degradation to β2-Adrenergic Receptors by β-Arrestins. *Science* **298**, 834–836 (2002).

91. Fischmeister, R. *et al.* Compartmentation of Cyclic Nucleotide Signaling in the Heart. *Circ. Res.* **99**, 816–828 (2006).

92. Miller, C. L. & Yan, C. Targeting cyclic nucleotide phosphodiesterase in the heart: therapeutic implications. *J Cardiovasc. Transl. Res.* **3**, 507–515 (2010).

93. Guellich, A., Mehel, H. & Fischmeister, R. Cyclic AMP synthesis and hydrolysis in the normal and failing heart. *Pflüg. Arch. - Eur. J. Physiol.* **466**, 1163–1175 (2014).

94. Miller, C. L. *et al.* Role of Ca2+/calmodulin-stimulated cyclic nucleotide phosphodiesterase 1 in mediating cardiomyocyte hypertrophy. *Circ. Res.* **105**, 956–964 (2009).

95. Dittrich, M. *et al.* Local response of L-type Ca(2+) current to nitric oxide in frog ventricular myocytes. *J. Physiol.* **534**, 109–121 (2001).

96. Mongillo, M. *et al.* Compartmentalized phosphodiesterase-2 activity blunts beta-adrenergic cardiac inotropy via an NO/cGMP-dependent pathway. *Circ. Res.* **98**, 226–234 (2006).

97. Vandecasteele, G., Verde, I., Rücker-Martin, C., Donzeau-Gouge, P. & Fischmeister, R. Cyclic GMP regulation of the L-type Ca(2+) channel current in human atrial myocytes. *J. Physiol.* **533**, 329–340 (2001).

98. Beca, S. *et al.* Phosphodiesterase type 3A regulates basal myocardial contractility through interacting with sarcoplasmic reticulum calcium ATPase type 2a signaling complexes in mouse heart. *Circ. Res.* **112**, 289–297 (2013).

99. Packer, M. *et al.* Effect of Oral Milrinone on Mortality in Severe Chronic Heart Failure. *http://dx.doi.org/10.1056/NEJM199111213252103* https://www.nejm.org/doi/10.1056/NEJM199111213252103 (2010) doi:10.1056/NEJM199111213252103.

100. Ding, B. *et al.* Functional Role of Phosphodiesterase 3 in Cardiomyocyte Apoptosis. *Circulation* **111**, 2469–2476 (2005).

101. Dodge, K. L. *et al.* mAKAP assembles a protein kinase A/PDE4 phosphodiesterase cAMP signaling module. *EMBO J.* **20**, 1921–1930 (2001).

102. Verde, I. *et al.* Myomegalin is a novel protein of the golgi/centrosome that interacts with a cyclic nucleotide phosphodiesterase. *J. Biol. Chem.* **276**, 11189–11198 (2001).

103. Lehnart, S. E. *et al.* Phosphodiesterase 4D Deficiency in the Ryanodine-Receptor Complex Promotes Heart Failure and Arrhythmias. *Cell* **123**, 25–35 (2005).

104. Mongillo, M. *et al.* Fluorescence Resonance Energy Transfer–Based Analysis of cAMP Dynamics in Live Neonatal Rat Cardiac Myocytes Reveals Distinct Functions of Compartmentalized Phosphodiesterases. *Circ. Res.* **95**, 67–75 (2004).

105. Terrenoire, C., Houslay, M. D., Baillie, G. S. & Kass, R. S. The cardiac IKs potassium channel macromolecular complex includes the phosphodiesterase PDE4D3. *J. Biol. Chem.* **284**, 9140–9146 (2009).

106. Patrucco, E., Albergine, M. S., Santana, L. F. & Beavo, J. A. Phosphodiesterase 8A (PDE8A) Regulates Excitation-Contraction Coupling in Ventricular Myocytes. *J. Mol. Cell. Cardiol.* **49**, 330–333 (2010).

107. MacDougall, L. K., Jones, L. R. & Cohen, P. Identification of the major protein phosphatases in mammalian cardiac muscle which dephosphorylate phospholamban. *Eur. J. Biochem.* **196**, 725–734 (1991).

108. Hescheler, J., Kameyama, M., Trautwein, W., Mieskes, G. & Söling, H. D. Regulation of the cardiac calcium channel by protein phosphatases. *Eur. J. Biochem.* **165**, 261–266 (1987).

109. Ponikowski, P. *et al.* Heart failure: preventing disease and death worldwide. *ESC Heart Fail.* **1**, 4–25 (2014).

110. Roger, V. L. Epidemiology of Heart Failure. *Circ. Res.* **128**, 1421–1434 (2021).

111. Packer, M., Medina, N. & Yushak, M. Hemodynamic and clinical limitations of long-term inotropic therapy with amrinone in patients with severe chronic heart failure. *Circulation* **70**, 1038–1047 (1984).

112. Promise Study Research Group *et al.* Effect of Oral Milrinone on Mortality in Severe Chronic Heart Failure. *N. Engl. J. Med.* **325**, 1468–1475 (1991).

113. Packer, M. *et al.* Double-blind, placebo-controlled study of the effects of carvedilol in patients with moderate to severe heart failure. The PRECISE Trial. Prospective Randomized Evaluation of Carvedilol on Symptoms and Exercise. *Circulation* **94**, 2793–2799 (1996).

114. Fukuda, K., Kanazawa, H., Aizawa, Y., Ardell, J. L. & Shivkumar, K. Cardiac innervation and sudden cardiac death. *Circ. Res.* **116**, 2005–2019 (2015).

115. Triposkiadis, F. *et al.* The Sympathetic Nervous System in Heart Failure. *J. Am. Coll. Cardiol.* **54**, 1747–1762 (2009).

116. Pepper, G. S. & Lee, R. W. Sympathetic Activation in Heart Failure and Its Treatment With β-Blockade. *Arch. Intern. Med.* **159**, 225–234 (1999).

117. Cohn, J. N. *et al.* Plasma norepinephrine as a guide to prognosis in patients with chronic congestive heart failure. *N. Engl. J. Med.* **311**, 819–823 (1984).

118. Engelhardt, S., Hein, L., Wiesmann, F. & Lohse, M. J. Progressive hypertrophy and heart failure in β1-adrenergic receptor transgenic mice. *Proc. Natl. Acad. Sci.* **96**, 7059–7064 (1999).

119. Communal, C., Singh, K., Pimentel, D. R. & Colucci, W. S. Norepinephrine Stimulates Apoptosis in Adult Rat Ventricular Myocytes by Activation of the β-Adrenergic Pathway. *Circulation* **98**, 1329–1334 (1998).

120. Zhu, W.-Z. *et al.* Linkage of β_1-adrenergic stimulation to apoptotic heart cell death through protein kinase A–independent activation of Ca^{2+}/calmodulin kinase II. *J. Clin. Invest.* **111**, 617–625 (2003).

121. Zhu, W. Z. *et al.* Dual modulation of cell survival and cell death by beta(2)-adrenergic signaling in adult mouse cardiac myocytes. *Proc. Natl. Acad. Sci. U. S. A.* **98**, 1607–1612 (2001).

122. Bristow, M. R. *et al.* Beta 1- and beta 2-adrenergic-receptor subpopulations in nonfailing and failing human ventricular myocardium: coupling of both receptor subtypes to muscle contraction and selective beta 1-receptor down-regulation in heart failure. *Circ. Res.* **59**, 297–309 (1986).

123. Luttrell, L. M. & Gesty-Palmer, D. Beyond Desensitization: Physiological Relevance of Arrestin-Dependent Signaling. *Pharmacol. Rev.* **62**, 305–330 (2010).

124. DeSantiago, J. *et al.* Arrhythmogenic Effects of β_2-Adrenergic Stimulation in the Failing Heart Are Attributable to Enhanced Sarcoplasmic Reticulum Ca Load. *Circ. Res.* **102**, 1389–1397 (2008).

125. Lang, D. *et al.* Arrhythmogenic Remodeling of β_2 Versus β_1 Adrenergic Signaling in the Human Failing Heart. *Circ. Arrhythm. Electrophysiol.* **8**, 409–419 (2015).

126. Bigger, J. T. Why patients with congestive heart failure die: arrhythmias and sudden cardiac death. *Circulation* **75**, IV28-35 (1987).

127. Packer, M. What causes sudden death in patients with chronic heart failure and a reduced ejection fraction? *Eur. Heart J.* **41**, 1757–1763 (2020).

128. Vaseghi, M., Lux, R. L., Mahajan, A. & Shivkumar, K. Sympathetic stimulation increases dispersion of repolarization in humans with myocardial infarction. *Am. J. Physiol.-Heart Circ. Physiol.* **302**, H1838–H1846 (2012).

129. Zhou, S. *et al.* Mechanisms of Cardiac Nerve Sprouting After Myocardial Infarction in Dogs. *Circ. Res.* **95**, 76–83 (2004).

130. Leenhardt, A., Denjoy, I. & Guicheney, P. Catecholaminergic Polymorphic Ventricular Tachycardia. *Circ. Arrhythm. Electrophysiol.* **5**, 1044–1052 (2012).

131. Faggioni, M., Kryshtal, D. O. & Knollmann, B. C. Calsequestrin Mutations and Catecholaminergic Polymorphic Ventricular Tachycardia. *Pediatr. Cardiol.* **33**, 959–967 (2012).

132. Leenhardt, A. *et al.* Catecholaminergic polymorphic ventricular tachycardia in children. A 7-year follow-up of 21 patients. *Circulation* **91**, 1512–1519 (1995).

133. Postma, A. V. *et al.* Catecholaminergic polymorphic ventricular tachycardia: RYR2 mutations, bradycardia, and follow up of the patients. *J. Med. Genet.* **42**, 863–870 (2005).

134. Sumitomo, N. Catecholaminergic polymorphic ventricular tachycardia: electrocardiographic characteristics and optimal therapeutic strategies to prevent sudden death. *Heart* **89**, 66–70 (2003).

135. Reid, D. S., Tynan, M., Braidwood, L. & Fitzgerald, G. R. Bidirectional tachycardia in a child. A study using His bundle electrography. *Heart* **37**, 339–344 (1975).

136. Swan, H. *et al.* Arrhythmic disorder mapped to chromosome 1q42–q43 causes malignant polymorphic ventricular tachycardia in structurally normal hearts. *J. Am. Coll. Cardiol.* **34**, 2035–2042 (1999).

137. Priori, S. G. *et al.* Mutations in the Cardiac Ryanodine Receptor Gene (hRyR2) Underlie Catecholaminergic Polymorphic Ventricular Tachycardia. 5.

138. Lahat, H. *et al.* Autosomal recessive catecholamine- or exercise-induced polymorphic ventricular tachycardia: clinical features and assignment of the disease gene to chromosome 1p13-21. *Circulation* **103**, 2822–2827 (2001).

139. Lahat, H. *et al.* A missense mutation in a highly conserved region of CASQ2 is associated with autosomal recessive catecholamine-induced polymorphic ventricular tachycardia in Bedouin families from Israel. *Am. J. Hum. Genet.* **69**, 1378–1384 (2001).

140. Roux-Buisson, N. *et al.* Absence of triadin, a protein of the calcium release complex, is responsible for cardiac arrhythmia with sudden death in human. *Hum. Mol. Genet.* **21**, 2759–2767 (2012).

141. Nyegaard, M. *et al.* Mutations in calmodulin cause ventricular tachycardia and sudden cardiac death. *Am. J. Hum. Genet.* **91**, 703–712 (2012).

142. Gomez-Hurtado, N. *et al.* Novel CPVT-Associated Calmodulin Mutation in *CALM3* (CALM3-A103V) Activates Arrhythmogenic Ca Waves and Sparks. *Circ. Arrhythm. Electrophysiol.* **9**, (2016).

143. Sumitomo, N. Current topics in catecholaminergic polymorphic ventricular tachycardia. *J. Arrhythmia* **32**, 344–351 (2016).

144. Wleklinski, M. J., Kannankeril, P. J., Forsythe, I. & Bers, D. Molecular and tissue mechanisms of catecholaminergic polymorphic ventricular tachycardia. *J Physiol* 18 (2020).

145. Wehrens, X. H. T. *et al.* FKBP12.6 Deficiency and Defective Calcium Release Channel (Ryanodine Receptor) Function Linked to Exercise-Induced Sudden Cardiac Death. *Cell* **113**, 829–840 (2003).

146. Zhang, J. Z. *et al.* FKBPs facilitate the termination of spontaneous Ca2+ release in wild-type RyR2 but not CPVT mutant RyR2. *Biochem. J.* **473**, 2049–2060 (2016).

147. Jiang, D. *et al.* RyR2 mutations linked to ventricular tachycardia and sudden death reduce the threshold for store-overload-induced Ca2+ release (SOICR). *Proc. Natl. Acad. Sci. U. S. A.* **101**, 13062–13067 (2004).

148. Ikemoto, N. & Yamamoto, T. Regulation of calcium release by interdomain interaction within ryanodine receptors. *Front. Biosci. J. Virtual Libr.* **7**, d671-683 (2002).

149. George, C. H. *et al.* Arrhythmogenic mutation-linked defects in ryanodine receptor autoregulation reveal a novel mechanism of Ca2+ release channel dysfunction. *Circ. Res.* **98**, 88–97 (2006).

150. Wang, Q. *et al.* Phylogenetic and biochemical analysis of calsequestrin structure and association of its variants with cardiac disorders. *Sci. Rep.* **10**, (2020).

151. Gray, B. *et al.* A novel heterozygous mutation in cardiac calsequestrin causes autosomal dominant catecholaminergic polymorphic ventricular tachycardia. *Heart Rhythm* **13**, 1652–1660 (2016).

152. Titus, E. W. *et al.* The structure of a calsequestrin filament reveals mechanisms of familial arrhythmia. *Nat. Struct. Mol. Biol.* 1–10 (2020) doi:10.1038/s41594-020-0510-9.

153. Györke, I., Hester, N., Jones, L. R. & Györke, S. The Role of Calsequestrin, Triadin, and Junctin in Conferring Cardiac Ryanodine Receptor Responsiveness to Luminal Calcium. *Biophys. J.* **86**, 2121–2128 (2004).

154. Oesterhelt, D. & Stoeckenius, W. Rhodopsin-like Protein from the Purple Membrane of Halobacterium halobium. *Nature. New Biol.* **233**, 149–152 (1971).

155. Nagel, G. *et al.* Channelrhodopsin-1: A Light-Gated Proton Channel in Green Algae. *Science* **296**, 2395–2398 (2002).

156. Nagel, G. *et al.* Channelrhodopsin-2, a directly light-gated cation-selective membrane channel. *Proc. Natl. Acad. Sci.* **100**, 13940–13945 (2003).

157. Boyden, E. S., Zhang, F., Bamberg, E., Nagel, G. & Deisseroth, K. Millisecond-timescale, genetically targeted optical control of neural activity. *Nat. Neurosci.* **8**, 1263–1268 (2005).

158. Bruegmann, T. *et al.* Optogenetic control of heart muscle in vitro and in vivo. *Nat. Methods* **7**, 897–900 (2010).

159. Bruegmann, T. *et al.* Optogenetic defibrillation terminates ventricular arrhythmia in mouse hearts and human simulations. *J. Clin. Invest.* **126**, 3894–3904 (2016).

160. Makowka, P. *et al.* Optogenetic stimulation of G s -signaling in the heart with high spatio-temporal precision. *Nat. Commun.* **10**, 1281 (2019).

161. Cokić, M., Bruegmann, T., Sasse, P. & Malan, D. Optogenetic Stimulation of Gi Signaling Enables Instantaneous Modulation of Cardiomyocyte Pacemaking. *Front. Physiol.* **12**, 768495 (2021).

162. Wagdi, A. *et al.* Selective optogenetic control of Gq signaling using human Neuropsin. *Nat. Commun.* **13**, 1765 (2022).

163. Beiert, T., Bruegmann, T. & Sasse, P. Optogenetic activation of Gq signalling modulates pacemaker activity of cardiomyocytes. *Cardiovasc. Res.* **102**, 507–516 (2014).

164. Wengrowski, A. M. *et al.* Optogenetic release of norepinephrine from cardiac sympathetic neurons alters mechanical and electrical function. *Cardiovasc. Res.* **105**, 143–150 (2015).

165. Li, X. *et al.* Fast noninvasive activation and inhibition of neural and network activity by vertebrate rhodopsin and green algae channelrhodopsin. *Proc. Natl. Acad. Sci. U. S. A.* **102**, 17816–17821 (2005).

166. Gutierrez, D. V. *et al.* Optogenetic Control of Motor Coordination by Gi/o Protein-coupled Vertebrate Rhodopsin in Cerebellar Purkinje Cells. *J. Biol. Chem.* **286**, 25848–25858 (2011).

167. Kim, J.-M. *et al.* Light-Driven Activation of β2-Adrenergic Receptor Signaling by a Chimeric Rhodopsin Containing the β2-Adrenergic Receptor Cytoplasmic Loops. *Biochemistry* **44**, 2284–2292 (2005).

168. Airan, R. D., Thompson, K. R., Fenno, L. E., Bernstein, H. & Deisseroth, K. Temporally precise in vivo control of intracellular signalling. *Nature* **458**, 1025–1029 (2009).

169. Siuda, E. R. *et al.* Optodynamic simulation of β-adrenergic receptor signalling. *Nat. Commun.* **6**, 8480 (2015).

170. Bailes, H. J., Zhuang, L.-Y. & Lucas, R. J. Reproducible and Sustained Regulation of Gαs Signalling Using a Metazoan Opsin as an Optogenetic Tool. *PLoS ONE* **7**, e30774 (2012).

171. Koyanagi, M. *et al.* Jellyfish vision starts with cAMP signaling mediated by opsin-G_s cascade. *Proc. Natl. Acad. Sci.* **105**, 15576–15580 (2008).

172. Coates, M. M. The spectral sensitivity of the lens eyes of a box jellyfish, Tripedalia cystophora (Conant). *J. Exp. Biol.* **209**, 3758–3765 (2006).

173. Knollmann, B. C. Casq2 deletion causes sarcoplasmic reticulum volume increase, premature Ca2+ release, and catecholaminergic polymorphic ventricular tachycardia. *J. Clin. Invest.* JCI29128 (2006) doi:10.1172/JCI29128.

174. Govardovskii, V. I., Fyhrquist, N., Reuter, T., Kuzmin, D. G. & Donner, K. In search of the visual pigment template. *Vis. Neurosci.* **17**, 509–528 (2000).

175. Cerrone, M. *et al.* Arrhythmogenic Mechanisms in a Mouse Model of Catecholaminergic Polymorphic Ventricular Tachycardia. *Circ. Res.* **101**, 1039–1048 (2007).

176. Kang, G. *et al.* Purkinje Cells From RyR2 Mutant Mice Are Highly Arrhythmogenic But Responsive to Targeted Therapy. *Circ. Res.* **107**, 512–519 (2010).

177. Xie, Y., Grandi, E., Bers, D. M. & Sato, D. How does β-adrenergic signalling affect the transitions from ventricular tachycardia to ventricular fibrillation? *EP Eur.* **16**, 452–457 (2014).

178. Chopra, N. *et al.* Modest Reductions of Cardiac Calsequestrin Increase Sarcoplasmic Reticulum Ca^{2+} Leak Independent of Luminal Ca^{2+} and Trigger Ventricular Arrhythmias in Mice. *Circ. Res.* **101**, 617–626 (2007).

179. Collins, K. A. *et al.* Accuracy of echocardiographic estimates of left ventricular mass in mice. *Am. J. Physiol.-Heart Circ. Physiol.* **280**, H1954–H1962 (2001).

180. Vinhas, M., Araújo, A. C., Ribeiro, S., Rosário, L. B. & Belo, J. A. Transthoracic echocardiography reference values in juvenile and adult 129/Sv mice. *Cardiovasc. Ultrasound* **11**, 12 (2013).

181. Dosdall, D. J. *et al.* Chemical ablation of the Purkinje system causes early termination and activation rate slowing of long-duration ventricular fibrillation in dogs. *Am. J. Physiol.-Heart Circ. Physiol.* **295**, H883–H889 (2008).

182. Lin, C. *et al.* Endocardial focal activation originating from Purkinje fibers plays a role in the maintenance of long duration ventricular fibrillation. *Croat. Med. J.* **55**, 121–127 (2014).

183. Spach, M. S., Huang, S. & Ayers, C. R. Electrical and anatomic study of the Purkinje system of the canine heart. *Am. Heart J.* **65**, 664–673 (1963).

184. Hayashi, M., Shimizu, W. & Albert, C. M. The Spectrum of Epidemiology Underlying Sudden Cardiac Death. *Circ. Res.* **116**, 1887–1906 (2015).

185. Marcus, G. M., Chan, D. W. & Redberg, R. F. Recollection of Pain Due to Inappropriate Versus Appropriate Implantable Cardioverter-Defibrillator Shocks. *Pacing Clin. Electrophysiol.* **34**, 348–353 (2011).

186. Larsen, G. K., Evans, J., Lambert, W. E., Chen, Y. & Raitt, M. H. Shocks burden and increased mortality in implantable cardioverter-defibrillator patients. *Heart Rhythm* **8**, 1881–1886 (2011).

187. Sohail, M. R., Henrikson, C. A., Braid-Forbes, M. J., Forbes, K. F. & Lerner, D. J. Mortality and cost associated with cardiovascular implantable electronic device infections. *Arch. Intern. Med.* **171**, 1821–1828 (2011).

188. Funken, M., Malan, D., Sasse, P. & Bruegmann, T. Optogenetic Hyperpolarization of Cardiomyocytes Terminates Ventricular Arrhythmia. *Front. Physiol.* **10**, 498 (2019).

189. Buxton, I. L. & Brunton, L. L. Compartments of cyclic AMP and protein kinase in mammalian cardiomyocytes. *J. Biol. Chem.* **258**, 10233–10239 (1983).

190. Bondarenko, V. E. A Compartmentalized Mathematical Model of the β1-Adrenergic Signaling System in Mouse Ventricular Myocytes. *PLOS ONE* **9**, e89113 (2014).

191. Coote, J. H. Myths and realities of the cardiac vagus. *J. Physiol.* **591**, 4073–4085 (2013).

192. Franciosi, S. *et al.* Chronotropic incompetence as a risk predictor in children and young adults with catecholaminergic polymorphic ventricular tachycardia. *J. Cardiovasc. Electrophysiol.* **30**, 1923–1929 (2019).

193. Moore, J. P. Slow and steady or fast and furious? Sinus node dysfunction in catecholaminergic polymorphic ventricular tachycardia. *J. Cardiovasc. Electrophysiol.* **30**, 1930–1931 (2019).

194. Neco, P. *et al.* Paradoxical Effect of Increased Diastolic Ca^{2+} Release and Decreased Sinoatrial Node Activity in a Mouse Model of Catecholaminergic Polymorphic Ventricular Tachycardia. *Circulation* **126**, 392–401 (2012).

195. Stern, M. D. *et al.* Hierarchical clustering of ryanodine receptors enables emergence of a calcium clock in sinoatrial node cells. *J. Gen. Physiol.* **143**, 577–604 (2014).

196. Glukhov, A. V. *et al.* Calsequestrin 2 deletion causes sinoatrial node dysfunction and atrial arrhythmias associated with altered sarcoplasmic reticulum calcium cycling and degenerative fibrosis within the mouse atrial pacemaker complex1. *Eur. Heart J.* **36**, 686–697 (2015).

197. Faggioni, M. *et al.* Accelerated Sinus Rhythm Prevents Catecholaminergic Polymorphic Ventricular Tachycardia in Mice and in Patients. *Circ. Res.* **112**, 689–697 (2013).

198. Kannankeril, P. J. *et al.* Atropine-induced sinus tachycardia protects against exercise-induced ventricular arrhythmias in patients with catecholaminergic polymorphic ventricular tachycardia. *EP Eur.* **22**, 643–648 (2020).

199. Alboni, P. *et al.* Effects of Permanent Pacemaker and Oral Theophylline in Sick Sinus Syndrome. *Circulation* **96**, 260–266 (1997).

200. Bittar, G. & Friedman, H. S. The arrhythmogenicity of theophylline. A multivariate analysis of clinical determinants. *Chest* **99**, 1415–1420 (1991).

201. Leandro, H. I. C., Lebedev, D. S. & Mikhaylov, E. N. Discrimination of ventricular tachycardia and localization of its exit site using surface electrocardiography. *J. Geriatr. Cardiol. JGC* **16**, 362–377 (2019).

202. Damiano, R. J. *et al.* The effect of chemical ablation of the endocardium on ventricular fibrillation threshold. *Circulation* **74**, 645–652 (1986).

203. Myles, R. C., Wang, L., Kang, C., Bers, D. M. & Ripplinger, C. M. Local ₙₜAdrenergic Stimulation Overcomes Source-Sink Mismatch to Generate Focal Arrhythmia. 25.

204. Blackwell, D. J. *et al.* The Purkinje–myocardial junction is the anatomic origin of ventricular arrhythmia in CPVT. *JCI Insight* **7**, e151893.

205. Vettel Christiane *et al.* Phosphodiesterase 2 Protects Against Catecholamine-Induced Arrhythmia and Preserves Contractile Function After Myocardial Infarction. *Circ. Res.* **120**, 120–132 (2017).

206. Brunet, S. *et al.* Heterogeneous expression of repolarizing, voltage-gated K+ currents in adult mouse ventricles. *J. Physiol.* **559**, 103–120 (2004).

207. Nerbonne, J. M. & Guo, W. Heterogeneous Expression of Voltage-Gated Potassium Channels in the Heart: Roles in Normal Excitation and Arrhythmias. *J. Cardiovasc. Electrophysiol.* **13**, 406–409 (2002).

208. Litovsky, S. H. & Antzelevitch, C. Transient outward current prominent in canine ventricular epicardium but not endocardium. *Circ. Res.* **62**, 116–126 (1988).

209. Wettwer, E., Amos, G. J., Posival, H. & Ravens, U. Transient outward current in human ventricular myocytes of subepicardial and subendocardial origin. *Circ. Res.* **75**, 473–482 (1994).

210. Antzelevitch, C. *et al.* Heterogeneity within the ventricular wall. Electrophysiology and pharmacology of epicardial, endocardial, and M cells. *Circ. Res.* **69**, 1427–1449 (1991).

211. Furukawa, T., Myerburg, R. J., Furukawa, N., Bassett, A. L. & Kimura, S. Differences in transient outward currents of feline endocardial and epicardial myocytes. *Circ. Res.* **67**, 1287–1291 (1990).

212. Pan, W., Yang, Z., Cheng, J., Qian, C. & Wang, Y. Contractile heterogeneity in ventricular myocardium. *J. Cell. Physiol.* **233**, 6273–6279 (2018).

213. Lou, Q. *et al.* Transmural Heterogeneity and Remodeling of Ventricular Excitation-Contraction Coupling in Human Heart Failure. *Circulation* **123**, 1881–1890 (2011).

214. Xiong, W., Tian, Y., DiSilvestre, D. & Tomaselli, G. F. Transmural Heterogeneity of Na+–Ca2+ Exchange. *Circ. Res.* **97**, 207–209 (2005).

215. Laurita, K. R., Katra, R., Wible, B., Wan, X. & Koo, M. H. Transmural Heterogeneity of Calcium Handling in Canine. *Circ. Res.* **92**, 668–675 (2003).

216. Prestle, J. Heterogeneous transmural gene expression of calcium-handling proteins and natriuretic peptides in the failing human heart. *Cardiovasc. Res.* **43**, 323–331 (1999).

217. Sande, J. B. *et al.* Reduced level of serine16 phosphorylated phospholamban in the failing rat myocardium: a major contributor to reduced SERCA2 activity. *Cardiovasc. Res.* **53**, 382–391 (2002).

218. Schwinger, R. H. G. *et al.* Reduced Ca2+-Sensitivity of SERCA 2a in Failing Human Myocardium due to Reduced Serin-16 Phospholamban Phoshorylation. *J. Mol. Cell. Cardiol.* **31**, 479–491 (1999).

219. Marx, S. O. *et al.* PKA phosphorylation dissociates FKBP12.6 from the calcium release channel (ryanodine receptor): defective regulation in failing hearts. *Cell* **101**, 365–376 (2000).

220. Reiken, S. *et al.* β-Adrenergic Receptor Blockers Restore Cardiac Calcium Release Channel (Ryanodine Receptor) Structure and Function in Heart Failure. *Circulation* **104**, 2843–2848 (2001).

221. Jessup, M. *et al.* Calcium Upregulation by Percutaneous Administration of Gene Therapy in Cardiac Disease (CUPID). *Circulation* **124**, 304–313 (2011).

222. Greenberg, B. *et al.* Calcium upregulation by percutaneous administration of gene therapy in patients with cardiac disease (CUPID 2): a randomised, multinational, double-blind, placebo-controlled, phase 2b trial. *The Lancet* **387**, 1178–1186 (2016).

223. Chen, Y. *et al.* Constitutive cardiac overexpression of sarcoplasmic/endoplasmic reticulum Ca2+-ATPase delays myocardial failure after myocardial infarction in rats at a cost of increased acute arrhythmias. *Circulation* **109**, 1898–1903 (2004).

224. del Monte, F. *et al.* Abrogation of ventricular arrhythmias in a model of ischemia and reperfusion by targeting myocardial calcium cycling. *Proc. Natl. Acad. Sci. U. S. A.* **101**, 5622–5627 (2004).

225. Steenaart, N. A., Ganim, J. R., Di Salvo, J. & Kranias, E. G. The phospholamban phosphatase associated with cardiac sarcoplasmic reticulum is a type 1 enzyme. *Arch. Biochem. Biophys.* **293**, 17–24 (1992).

226. Endo, S., Zhou, X., Connor, J., Wang, B. & Shenolikar, S. Multiple Structural Elements Define the Specificity of Recombinant Human Inhibitor-1 as a Protein Phosphatase-1 Inhibitor,. *Biochemistry* **35**, 5220–5228 (1996).

227. Qian, J. *et al.* Small heat shock protein 20 interacts with protein phosphatase-1 and enhances sarcoplasmic reticulum calcium cycling. *Circ. Res.* **108**, 1429–1438 (2011).

228. Lygren, B. *et al.* AKAP complex regulates Ca2+ re-uptake into heart sarcoplasmic reticulum. *EMBO Rep.* **8**, 1061–1067 (2007).

229. Xie, Y., Grandi, E., Puglisi, J. L., Sato, D. & Bers, D. M. β-adrenergic stimulation activates early afterdepolarizations transiently via kinetic mismatch of PKA targets. *J. Mol. Cell. Cardiol.* **58**, 153–161 (2013).

230. Terrenoire, C., Clancy, C. E., Cormier, J. W., Sampson, K. J. & Kass, R. S. Autonomic Control of Cardiac Action Potentials. *Circ. Res.* **96**, e25–e34 (2005).

231. Ravens, U. & Wettwer, E. Electrophysiological aspects of changes in heart rate. *Basic Res. Cardiol.* **93**, s060–s065 (1998).

232. Zykov, V., Krekhov, A. & Bodenschatz, E. Fast propagation regions cause self-sustained reentry in excitable media. *Proc. Natl. Acad. Sci. U. S. A.* **114**, 1281–1286 (2017).

233. Iqbal, S. M. & Lemmens-Gruber, R. Phosphorylation of cardiac voltage-gated sodium channel: Potential players with multiple dimensions. *Acta Physiol.* **225**, e13210 (2019).

234. Shah, M. M., Martinez, A.-M. & Fletcher, W. H. The connexin43 gap junction protein is phosphorylated by protein kinase A and protein kinase C: in vivo and in vitro studies. *Mol. Cell. Biochem.* **238**, 57–68 (2002).

235. Salameh, A. & Dhein, S. Adrenergic control of cardiac gap junction function and expression. *Naunyn. Schmiedebergs Arch. Pharmacol.* **383**, 331–346 (2011).

236. Campbell, A. S., Johnstone, S. R., Baillie, G. S. & Smith, G. β-Adrenergic modulation of myocardial conduction velocity: Connexins vs. sodium current. *J. Mol. Cell. Cardiol.* **77**, 147–154 (2014).

237. Lampe, P. D. & Lau, A. F. The effects of connexin phosphorylation on gap junctional communication. *Int. J. Biochem. Cell Biol.* **36**, 1171–1186 (2004).

238. Molina, C. E. *et al.* Differences in Left Versus Right Ventricular Electrophysiological Properties in Cardiac Dysfunction and Arrhythmogenesis. *Arrhythmia Electrophysiol. Rev.* **5**, 14 (2016).

239. Volders, P. G. *et al.* Repolarizing K+ currents ITO1 and IKs are larger in right than left canine ventricular midmyocardium. *Circulation* **99**, 206–210 (1999).

240. Choi, S. W. *et al.* Increased Expression of ATP-sensitive K Channels Improves the Right Ventricular Tolerance to Hypoxia in Rabbit Hearts. *Korean J. Physiol. Pharmacol. Off. J. Korean Physiol. Soc. Korean Soc. Pharmacol.* **15**, 189–194 (2011).

241. Molina, C. E. *et al.* Interventricular Differences in β-Adrenergic Responses in the Canine Heart: Role of Phosphodiesterases. *J. Am. Heart Assoc. Cardiovasc. Cerebrovasc. Dis.* **3**, e000858 (2014).

242. Beyer, S., Kelly, R. G. & Miquerol, L. Inducible Cx40-Cre expression in the cardiac conduction system and arterial endothelial cells. *genesis* **49**, 83–91 (2011).

7 List of Figures

8 List of Tables

9 Appendix

9.1 Publications

Makowka P, Bruegmann T, **Dusend V**, Malan D, Beiert T, Hesse M, et al. Optogenetic stimulation of G_s-signaling in the heart with high spatio-temporal precision. Nature Communications. 2019 Mar 20;10(1):1281. DOI: 10.1038/s41467-019-09322-7.

Izadi I, **Dusend V**, Takrouni A, Nudds N, Gradkowski K, O'Brien P, et al. Wide Area Uniform Illumination Scheme Using LED Matrix for Optogenetic Cardiac Pacing. Photonics. 2021 Nov;8(11):499. DOI: 10.3390/photonics8110499.

Wagdi A., Malan D., Sathyanarayana, U., Beauchamp J.S., Vogt M., Zipf D., Beiert T., Mansuroglu B., **Dusend V**., Meininghaus M., Schneider L., Kalthof B., Wiegert J.S., König G.M., Kostenis E., Patejdl R., Sass, P., Bruegmann T. Selective optogenetic control of G_q signaling using human Neuropsin. Nat Commun. 2022 Apr 1;13(1):1765. DOI: 10.1038/s41467-022-29265-w.

9.2 Oral and poster presentations

Poster presentation at the Cardiovascular Disease Symposium (Düsseldorf, Germany, 15.-06.03.2018): "Optogenetic stimulation of G_s signaling in intact heart to analyze Ca^{2+}-leak induced arrhythmia"

Poster presentation at the Europhysiology 2018 (London, England, 14.-16.09.2018): "Optogenetic stimulation of G_s signaling in intact heart to analyze Ca^{2+}-leak induced arrhythmia"

Poster presentation at the RTG 1873 "Pharmacology of 7TM-receptors and downstream signaling pathways" (Bonn, Germany, 29.-30.08.2019): "Optogenetic stimulation of G_s signaling to analyze Ca^{2+}-leak induced arrhythmia"

Oral Presentation at the Cardiovascular Disease Symposium (CaVaD) 2021 (Düsseldorf, Germany, 01.-02.06.2021): „Optogenetic stimulation of G_s signaling increases ventricular arrhythmia triggering and maintenance"

Poster presentation at the German Physiological Society (DPG) Annual Meeting 2021 (Frankfurt, Germany, 30.09.-02.10.2021): „Optogenetic stimulation of G_s signaling increases ventricular arrhythmia triggering and maintenance"

Poster presentation at the Europhysiology 2022 (Copenhagen, Denmark, 16.-18.09.2022): „Optogenetic stimulation of G_s signalling increases ventricular arrhythmia triggering from the endocardium and modulates arrhythmia maintenance and complexity"

Oral and poster presentation at the Gordon Research Conference and Seminar on Cardiac Arrhythmia Mechanisms (Texas, USA, 25.02.-03.03.2023): "Optogenetic stimulation of G_s signaling increases ventricular arrhythmia triggering from the endocardium and modulates arrhythmia maintenance and complexity"

10 Acknowledgements (Danksagung)

Als erstes möchte ich mich bei meinem Doktorvater Prof. Dr. Philipp Saße bedanken, dass er mir die Möglichkeit gab in seiner Arbeitsgruppe dieses außerordentlich interessante Projekt durchzuführen. Danke für die hervorragende Betreuung und stete Unterstützung während meiner Doktorandenzeit. Weiterhin danke ich Prof. Dr. Bernd Fleischmann für die Möglichkeit, am Institut der Physiologie I an der Uniklinik Bonn meine Doktorarbeit durchzuführen. Außerdem möchte ich Prof. Dr. Evi Kostenis für die Übernahme der Ko-Betreuung und als 2. Gutachterin, Prof. Dr. Dagmar Wachten für die Teilnahme an meinem Promotionskomitee als fachfremdes Mitglied und Prof. Dr. Christa Müller für den Vorsitz des Komitees danken. Dank gilt auch der fachlichen und finanziellen Unterstützung durch die DFG und dem Graduiertenkolleg 1873.

Ich danke allen Mitarbeitern des Instituts der Physiologie I für die tolle Zusammenarbeit und fachliche Unterstützung. Meine Kollegen und Freunde am Institut haben diese Zeit zu einem besonderen, unvergesslichen Erlebnis gemacht. Mein besonderer Dank gilt hier den Mitarbeitern der AG Saße: Philipp Saße, Daniela Malan, Wanchana Jangsangthong, Berivan Mansuroglu und Frank Holst. Danke euch für die vielseitige Unterstützung im Labor und für die schönen gemeinsamen Erlebnisse, ob auf gemeinsamen Konferenzen, bei Grillfeiern, Kochabenden oder beim Bouldern.

Mein ganz besonderer Dank gilt meinen Eltern, die mich stets unterstützt haben und deren Fürsorge und Liebe mir diesen Weg ermöglicht haben. Dieser Dank gilt auch meiner restlichen Familie, insbesondere meiner Schwester Lotti. Danke euch!